Processing and Characterization of Proton Conducting Yttrium Doped Barium Zirconate for Solid Oxide Fuel Cell Applications

Thesis by

Peter Babilo

In Partial Fulfillment of the Requirements

For the Degree of

Doctor of Philosophy

California Institute of Technology

Pasadena, California

2007

(Defended May 16, 2007)

Acknowledgements

The Ph.D. program at Caltech was definitely a unique experience. The cycles of excitement, joyfulness, and confidence followed by times of uncertainty and bewilderment seemed never ending. Having said that, I truly believe it was one of the best decisions I have made, not only for the intellectual maturity, self confidence, and perspectives I have gained throughout my graduate career, but also the friendships I made with fellow coworkers. This thesis is the result of six years of work during which I have been accompanied, supported, and entertained by many people. I would like to express my gratitude to all those made the completion of this thesis possible.

I am deeply indebted to my advisor Professor Sossina Haile for giving me the opportunity to pursue my graduate work under her guidance. Her constant strive for perfection and incredible work ethic was a constant source of motivation and excellence in research. With every conversation the insight and perspectives I acquired were invaluable.

I am also very appreciative of Professor G. Scott Samuelsen and Dr. Jack Brouwer for allowing me to pursue undergraduate research at UCI. It was at the NFCRC that I was first introduced to fuel cell technology and their immense technological potentials.

I would like to express my sincere gratitude to the exceptionally talented post-doctoral and visiting scholars: Dr. Tetsuya Uda, Dr. Zongping Shao, Dr. Yoshi Yamazaki, and Dr. Mary Thundathil. Their guidance and wealth of knowledge aided me throughout my graduate career.

My years at Caltech would not have been the same without the brilliant yet peculiar colleagues. I thank Dr. Calum Chisholm, Dr. Dane Boysen, Dr. Jian Wu, and Ryan Merle for initial guidance and the establishment of our laboratory. Many thanks to Dr. Wei Lia, Dr. Lisa Cowan, Kenji Sasaki, Justin Ho, and Martin Smith-Martinez for sharing equipment, aiding with coursework, and providing valuable insights into research oddities. I enjoyed the many

conversations, not always scientific, we had. It was a great pleasure to work and socialize with all Haile group members. I also want to thank undergraduate student, Yuki Kimura, and visiting student, Agathe Jarry, for their help with experimental work.

Experimental work, design, and fabrication would have been infinitely harder without the expertise of Mike Vondrus in the machine shop and Rick Gerhart in the glass blowing shop. I would also like to thank Dr. Chi Ma for his expertise and assistance with electron microscopy, and Dr. Sonjong Hwang for his support with NMR measurements.

I feel a deep sense of gratitude to my family, especially my parents, Victor and Violet, whose many sacrifices and support (not to mention delicious food) allowed me to reach my educational goals. The dedication to their children and accomplishments provides a persistent inspiration for my journey in life. Thanks to my sisters for keeping me well-grounded throughout my years at Caltech.

I am very grateful for my wife, Jeanna, for her love, patience, and encouragement (when needed) during the Ph.D. program. Her always joyful spirit and nudging (at times) was instrumental in helping me prevail through demanding times.

Finally, I would like to acknowledge the support of the Department of Energy for providing the majority of the funding for this work.

Abstract

To address the wide range of reported conductivities in literature and investigate the viability of yttrium-doped barium zirconate ($BaZr_{1-x}Y_xO_{3-\delta}$) as a membrane in electrochemical devices, the factors governing the protonic transport properties have been explored, with the aim of attaining reproducible proton conductivity in well-densified samples. It was found that a small initial particle size (50–100 nm) and high temperature sintering (1600 °C) in the presence of excess barium were essential. By this procedure, $BaZr_{0.8}Y_{0.2}O_{3-\delta}$ with 93%–99% theoretical density and total (bulk plus grain boundary) conductivity of 7.9×10^{-3} S/cm at 600 °C could be reliably prepared. Samples sintered in the absence of excess barium displayed yttria-like precipitates and a bulk conductivity that was reduced by more than two orders of magnitude.

Hydrogen transport across grain boundaries has been explored and the specific conductivity found to be two orders of magnitude lower than the bulk. Microstructural optimization of the total grain boundary conductivity included both decreasing total grain boundary density as well as improving intrinsic grain boundary properties.

To investigate the influence of defect chemistry on stability, proton solubility, and proton mobility; samples with yttrium dopant concentration of 30 and 40 mol % were prepared in addition to the well characterized 20 Y mol %. Lattice parameters obtained suggests the solubility of yttrium in barium zirconate to be at least 40 mol %. Thermogravimetric analysis of the barium zirconate system under flowing CO_2 showed excellent chemical stability for all dopant concentrations. Hydrogen incorporation experiments showed barium zirconate is fully saturated at temperatures below 50 ºC, approaching theoretical hydrogen concentration for 20, 30, and 40 Y mol %. Thermodynamic hydration parameters were examined, and found to be independent of dopant concentration. Significant hydroxyl-dopant associations were observed, especially at lower temperatures, which trap protons and impedes transport.

To simplify processing procedures, the influence of transitional metal oxides additives (especially zinc oxide) on the densification and electrical properties of doped barium zirconate have been examined. With the use of zinc oxide as a sintering aid, $BaZr_{0.85}Y_{0.15}O_{3-\delta}$ was readily sintered to above 93% of theoretical density at 1300 °C. SEM investigations showed Zn accumulation in the intergranular regions. The conductivity, as measured by A.C. impedance spectroscopy under H_2O saturated nitrogen, was slightly lower than that of unmodified barium zirconate.

Electromotive force measurements of $BaZr_{0.80}Y_{0.20}O_{3-\delta}$ showed the ionic transference number under fuel cell conditions (H_2,H_2O | BYZ | air,H_2O) to be at least 0.92 at 600 °C. Fuel cells based on BYZ20 with an electrolyte thickness of 320 μm and Pt electrodes were prepared and characterized. Peak power output with humidified hydrogen supplied to the anode and humidified oxygen supplied to the cathode was 42.9 mW/cm^2, and the limiting current (current at short circuit) was 155 mA/cm^2.

Contents

List of Figures

List of Tables

Chapter 1: Introduction and Background

1.1 Structure and Defect Chemistry of Doped Barium Zirconate

1.1.1 Perovskite Structure

Yttrium doped barium zirconate is commonly accepted as a single-phase, cubic perovskite, similar to the undoped composition, space group Pm-3m with lattice constant 4.1973Å [1]. Although the name perovskite was originally used to describe the rare mineral $CaTiO_3$, it is commonly used today to describe a more general group of oxides with a similar crystal structure. The perovskite structure has the general formula ABO_3, where the A-cation is a metal with a +2 or +3 charge and the B-cation with a +4 or +3 charge, respectively. The A-site cations are located at the corners of the unit cell with B-site cations in the center, Figure 1.1. The oxygen ions are at the centers of each face of the unit cell.

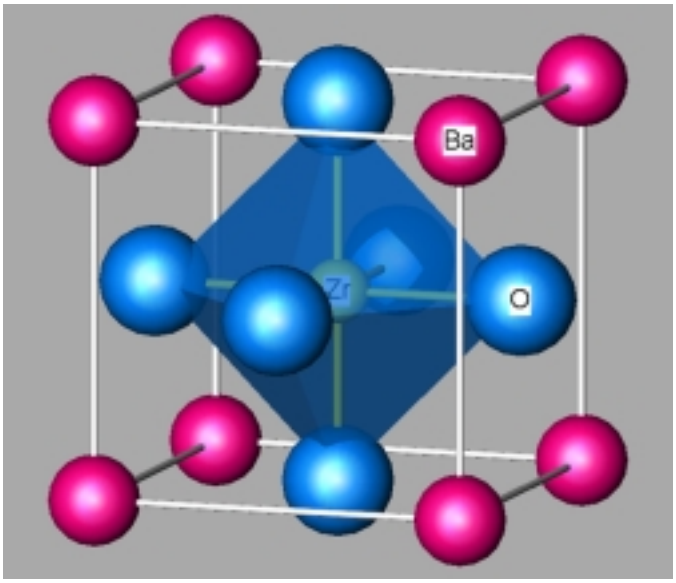

Figure 1.1. Perovskite unit cell of barium zirconate.

Due to the high symmetry of the cubic structure, the calculated x-ray diffraction of the undoped barium zirconate is easily recognized, Figure 1.2.

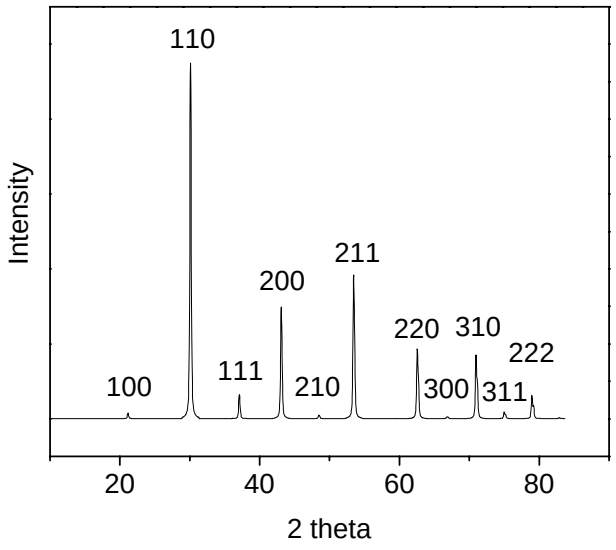

Figure 1.2. Barium zirconate reference pattern, ICSD database 90049.

Although many research groups consider doped barium zirconate a cubic material, Kreuer has reported that at the intermediate Y content and 1700 ºC sintering temperature, barium zirconate adopts a tetragonal structure, reverting to a cubic phase at higher Y doping (25 mol %) [2]. The general crystal structure deviates from a cube when the sum of the A-site and oxygen or B-site and oxygen ionic radii greatly differ from the A-O and B-O bond distances. The deviation can be quantified using the Goldschmidt tolerance factor, Eq. (1.1). The tolerance factor is based on geometrical packing of spheres and it describes the ratio of A-site-oxygen distance and B-site oxygen distance. As the tolerance factor departs from unity, distortions often occur, of which tilting is the most common.

$$t = \frac{r_A + r_O}{\sqrt{2}(r_B + r_O)} \tag{1.1}$$

The perovskite structure is very versatile having many useful technological applications such as ferroelectrics, thermoelectrics, catalysts, fuel cell electrolytes, and superconductors.

Complex perovskite structures also exist that contain two different B-site cations in the unit cell, which can result in a disordered structure due to the dissimilar site occupancy.

1.1.2 Defect Chemistry and Water Incorporation

In the perovskite structure acceptor doping can be performed by the partial substitution of B-site with a +3 cation or the substitution of the A-site with a +1 cation. Specifically, for barium zirconate, the zirconium (B-site) is partially substituted with a trivalent yttrium to create oxygen vacancies. With a significant dopant concentration, extrinsic oxygen vacancy defects are the dominant species. Proton conduction then can occur via the incorporation of protonic defects as the result of the B-site acceptor doping. In Kröger-Vink notation [3], this can be written as

$$Y_2O_3 + 2Zr_{Zr}^{x} + O_O^{x} \rightarrow 2Y_{Zr}' + V_O^{\bullet\bullet} + 2ZrO_2 . \tag{1.2}$$

In dry atmospheres, as shown above, oxygen vacancies provide the charge compensation for the acceptor dopants. In hydrogen or water saturated atmospheres, hydroxyl ion compensate the acceptors and contribute to the protonic conductivity. Proton incorporation is found to be an exothermic reaction [2], Eq. (1.3).

$$H_2O + V_O^{\bullet\bullet} + O_O^{x} \leftrightarrow 2OH_O^{\bullet} \tag{1.3}$$

Protons are not part of the nominal structure, but are present as defects in equilibrium with ambient hydrogen or water vapor. Due to the negative enthalpy and entropy of hydration [2], higher temperatures result in a reversible loss of protons.

For highly oxidizing conditions (wet or dry), holes are created by the dissolution of oxygen, Eq. (1.4). The creation of holes combined with the loss of protons at higher temperatures, leads to a slight electronic conduction in the bulk of the material.

$$\frac{1}{2}O_2 + V_O^{\bullet\bullet} \rightarrow O_O^{x} + 2h^{\bullet} \tag{1.4}$$

1.1.3 Proton Transport

Iwahara [4] first demonstrated the existence of proton conduction in ABO_3 perovskites, and many studies have since shown that cerates and zirconates based perovskites can have substantial levels of proton conductivity [5–7]. Transport of protons between stationary host anions is termed the Grotthuss mechanism as opposed to the transport of hydroxyl ions as a whole. The latter is termed a vehicle mechanism of transport and is commonly encountered in aqueous solution and other liquid-like membranes. In solids, the vehicle mechanism is restricted to materials with open structures to allow for the passage of ions and molecules. An example of the vehicle mechanism includes polymer membranes, in which the vehicular mechanism is used to transport protons in a H_3O^+ ion.

In the Grotthuss mechanism the proton diffuses through a combination of molecular re-orientation around the oxygen and proton hopping from oxygen to adjacent oxygen. Atomistic simulations [8] have shown rapid proton transport to be a barrierless process. The orientation of the O-H group has the proton close to the direction of an adjacent oxide ion. Rotational rates on a timescale of 10^{-12} s for a complete turn and proton jump rates on the order of 10^{-9} s. In addition, the timescale for O-H bending and stretching modes are on the order of 10^{-13} and 10^{-14} s [9]. The proton jump is the rate limiting step in this mechanism. Figure 1.3 shows proton reorientation and displacement.

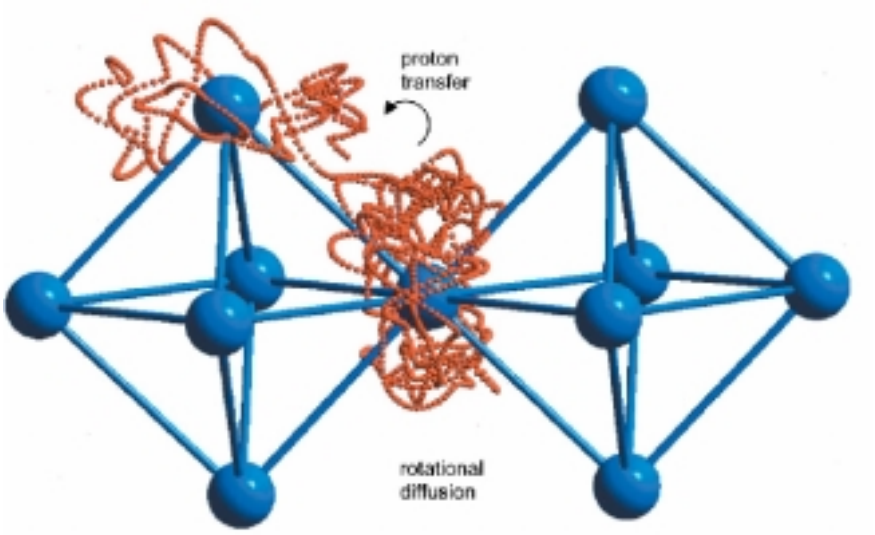

Figure 1.3. Simulation of proton reorientation and displacement [10].

Molecular dynamic simulation of perovskites [9,11] provides further insight in the proton transport mechanism for the perovskite structure. The protons have rotational reorientation around an oxygen ion in the plane perpendicular to the B-O-B axis. Preceding the proton transfer, lattice relaxation is required to achieve equivalent environment around each oxide ion. During the hopping of the proton, the O–H bond to the host ion is retained while simultaneously forming an O–H bond with the neighboring oxide ion. Transfer takes place through a mechanism in which bond formation accompanies bond breaking. The strong interactions of the proton with two oxygens avoid the need to break O-H bonds, with energy ~ 4eV [11]. This concept is shown in Eq. (1.5).

$$OH - O \rightarrow O - H - O \rightarrow O - HO \tag{1.5}$$

In the case of barium zirconate, the Zr-O bond is stiffer compared to that of barium cerates resulting in shorter O-O separation [9]. The energy barrier for proton transfer is lowered by a shortening of the O-O separation.

The conductivity of each ionic species is directly proportional to the density of mobile ions, n, that are carrying a charge, q, with mobility, μ. Generally, the density of mobile ions can

be controlled via the defect chemistry, while mobility is a function of the intrinsic properties of the material (structure and chemistry) and temperature.

$$\sigma = nq\mu \tag{1.6}$$

The mobility is further related to the corresponding diffusivities by the Nernst-Einstein relation:

$$\mu = \frac{qD}{kT}. \tag{1.7}$$

Random walk theory relates the diffusivity of each carrier to its mean jump frequency and jump distance, λ.

$$D = \frac{1}{6}\Gamma\lambda^2 \tag{1.8}$$

Jump frequency can be further written as a thermally activated process

$$\Gamma = zw_0 e^{\frac{-H}{k_B T}}, \tag{1.9}$$

where H is the jump activation enthalpy, z is the number of direction in which the jump can occur, w_0 is a combination of the entropy of activation and lattice vibration frequency, $w_0 = v_0 e^{\frac{\Delta S}{k_B}}$. Combining Eq. (1.6) through (1.9), resulting in the conductivity as a function of temperature, Eq. (1.10).

$$\sigma T = Ae^{\frac{-H}{k_B T}}, \tag{1.10}$$

where

$$A = \frac{znw_0 q^2 \lambda^2}{6k_B}. \tag{1.11}$$

Plotting the conductivity data as shown in Eq. (1.12) allows for the calculation of both the activation enthalpy of the ionic transport as well as the preexponential factor.

$$Log(\sigma T) = -\frac{E}{k_B T} * Log(e) + Log(A) \tag{1.12}$$

1.1.4 Chemical Stability

Although the cerate based compounds were shown to have noteworthy proton conduction at elevated temperature, many suffer from chemical instability under CO_2 and H_2O containing atmospheres, readily forming alkaline earth carbonates [7, 12] according to Eq. (1.13) or alkaline earth hydroxides [13], Eq. (1.14).

$$BaCeO_3 + CO_2 \rightarrow BaCO_3 + CeO_2 \tag{1.13}$$

$$BaCeO_3 + H_2O \rightarrow Ba(OH)_2 + CeO_2 \tag{1.14}$$

This reactivity causes severe degradation of the material and precludes applications in electrochemical devices in severe conditions, such as a fuel cell based on hydrocarbon fuels. In contrast, barium zirconate exhibits excellent stability under CO_2 [14, 15], rendering it highly attractive for applications in aggressive environments.

Figure 1.4 shows the Gibbs energy of formation of barium hydroxide, barium carbonate, and the formation of the perovskite from oxides [13]. $BaCeO_3$ exhibits relatively high formation energy, compared to $BaTiO_3$ and $BaZrO_3$. For the perovskite to be stable, the Gibbs energy of perovskite formation must be lower than both the formation energy of the hydroxide and carbonate. The barium zirconate system is stable against the hydroxide formation at all given water partial pressures and temperatures. Below ~530 ºC in pure CO_2 (1atm), decomposition reaction of barium zirconate is thermodynamically expected, however, slow kinetics allow the system to maintain its stability.

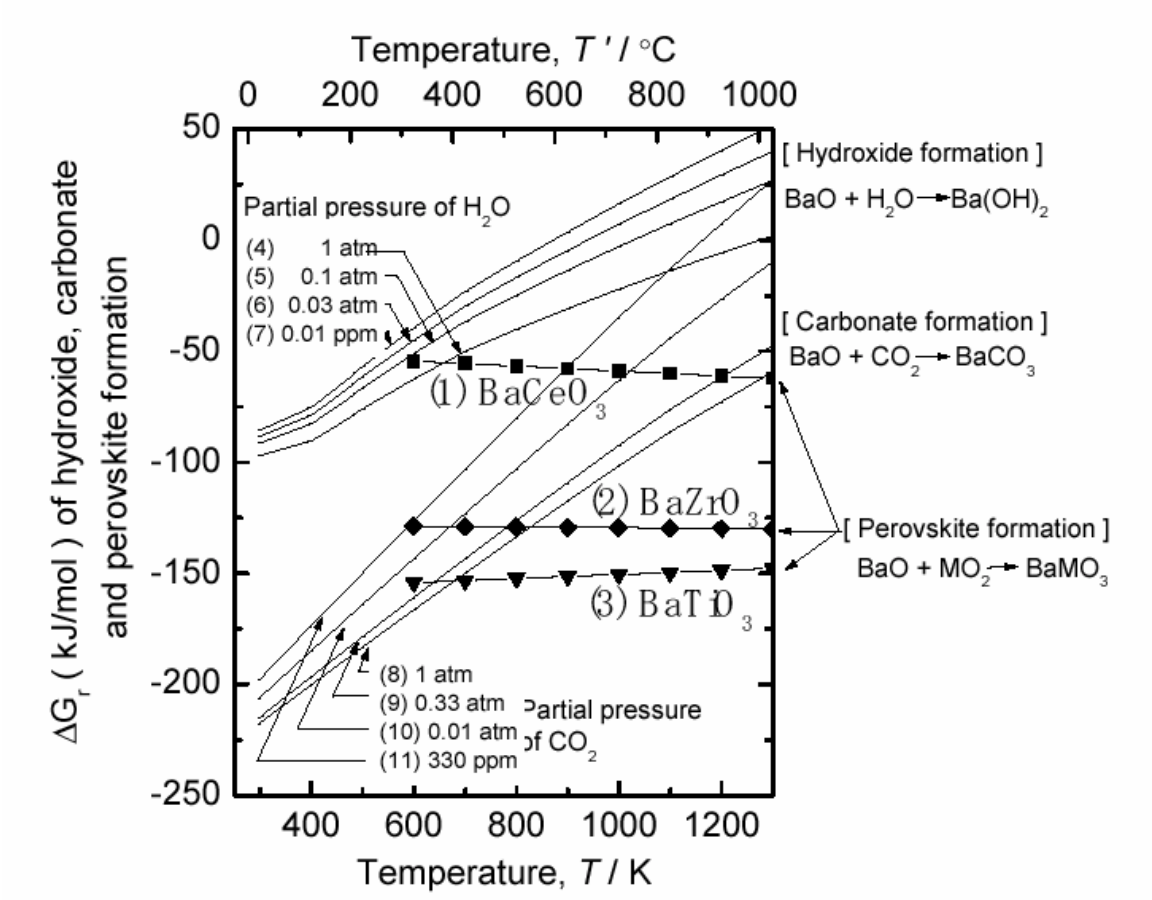

Figure 1.4. Gibbs energy of formation of barium hydroxide, barium carbonate, and perovskite from constituent oxides [13].

1.1.5 Conductivity of Doped Barium Zirconate in Literature

The earliest studies of doped barium zirconate, which appeared in the early 1990s, suggested that this material exhibits poor proton conductivity as compared to doped barium cerate. Although their reported values differ by two orders of magnitude, researchers all agreed that the conductivity of the zirconate is no more than 1.2×10^{-4} S/cm at 600 °C. The understanding of the properties of barium zirconate was revised substantially in 1999. In that year Kreuer [16] reported the conductivity of yttrium doped barium zirconate to be $\sim 5 \times 10^{-5}$ S/cm at just 140 °C and this was quickly confirmed by Schober and Bohn in 2000 [17]. The early mis-

interpretation of the behavior of doped barium zirconate originates from the high refractory nature of this material, which results in samples with small grain sizes and high total grain boundary area. As a consequence, the resistive grain boundaries produce a material with an overall low conductivity, and, in the absence of low temperature A.C. impedance measurements (<200 °C), the individual bulk and grain boundary contributions to conductivity were not resolved in the early literature.

In a follow up paper to his original, Kreuer noted the poor reproducibility of conductivity measurements of barium zirconate [10] and argued that this is connected to the difficulty in fabricating polycrystalline compacts of the material given the extreme processing conditions needed. Thus far, reported conductivity measurements of doped barium zirconate range from 10^{-6} to 10^{-2} S/cm. Causes and solutions for this inconsistency will be further discussed in Chapter 3.

1.2 Electrochemical Applications

Solid electrolytes, such as doped barium zirconate, are used in a variety of electrochemical applications, of which some will be highlighted below. In all applications, the electrolyte performs three critical functions: (1) separation of the two chambers (or reactants), (2) electronic insulator as to force the electrical current to pass through an external circuit, and (3) high conduction of ions to provide the balance for the electronic current in the external circuit.

Applications of proton conducting ceramics can be classified in two fundamental functions: (1) electromotive force based on a chemical potential gradient and (2) electrochemical hydrogen transport driven by an external power source. Using a proton conductor as a solid electrolyte in a chemical potential gradient, the generated voltage can be utilized as an electrical power source (fuel cell) or a signal that depends on the chemical potential of hydrogen in a specified chamber (activity sensor). Second, protonic conductors can function as a medium for preferential hydrogen transport when an external driving force is present. This function can be

utilized as a hydrogen pump, hydrogen extraction from mixed gases, and devices based on similar principles.

1.2.1 Fuel Cells and Sensors

A fuel cell is an energy conversion device that produces electricity and heat by electrochemical combination of gaseous fuel and oxidant (air). Ceramic fuel cells, in specific, combine the fuel and oxidant across an ionic conducting ceramic. Similar to a battery, this solid-state device consists of two electrodes (anode and cathode) which are separated by the solid electrolyte, Figure 1.5. However, a fuel cell, unlike a battery, does not require charging, as long as fuel and oxidant are supplied from an external source, electricity is generated.

Fuel, such as hydrogen, is fed to the anode which is oxidized and releases electrons to an external circuit, while air (oxidant) is fed to the cathode and is reduced, accepting electrons from the external circuit. The electron flow through the external circuit from the anode to the cathode produces the direct current (D.C.) electricity.

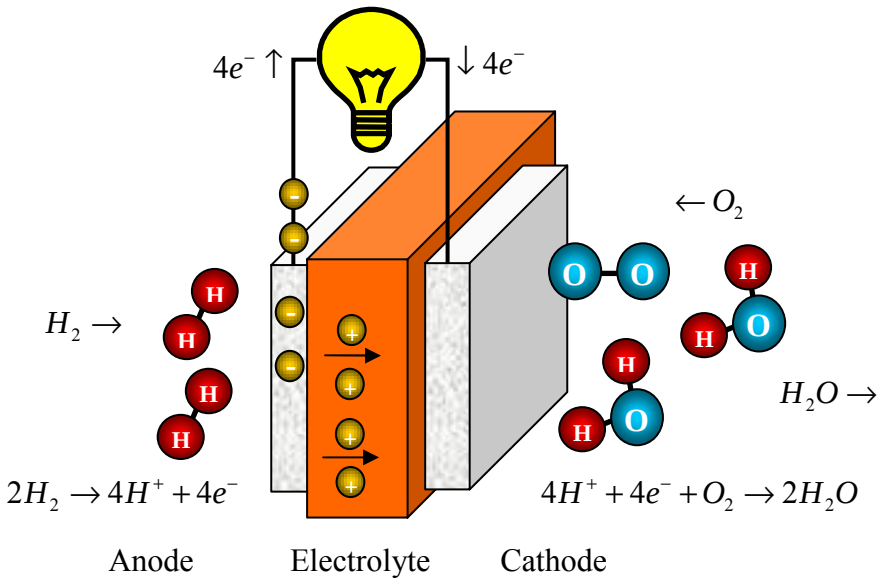

Figure 1.5. Schematic of fuel cell including an anode, a cathode and an electrolyte.

Unlike combustion engines, solid oxide fuel cells convert the chemical energy of reactants directly to electrical energy without the need for combustion, Table 1.1. This allows for higher efficiencies, quieter operation, and greater reliability due to the absence of moving parts.

Table 1.1. Converting chemical energy to electrical energy, comparison of two methods.

Combustion
Chemical energy $\rightarrow$ thermal energy $\rightarrow$ mechanical energy $\rightarrow$ electrical energy
Fuel cell
Chemical energy $\rightarrow$ electrical energy

Sensors function identically to a fuel cell with the objective of providing a small D.C signal. Voltage (the signal) arises due to the difference in the activity (or molar concentration) of hydrogen between two sides of the proton conducting electrolyte. This type of sensor can be used not only for detecting hydrogen gas but also for water vapor and hydrocarbon gases at elevated temperatures where thermodynamic equilibrium is attained with respect to hydrogen.

1.2.2 Preferential Permeation of Hydrogen Ions

In addition to direct energy conversion, high temperature proton conducting materials are also favorable for use in preferential permeation of hydrogen ions including hydrogen extraction, hydrogen pumping, dehumidification/steam pump, selective filtration, electrolysis, and membrane reactor for dehydrogenation of hydrocarbons.

A schematic of the principle of electrochemical pumping of hydrogen is shown in Figure 1.6. As opposed to operations of a fuel cell, these electrochemical devices require external power to transport the hydrogen across the membrane. On passing a direct current through the proton-conducting electrolyte, hydrogen (or water or hydrocarbon) at the anode is oxidized to form

protons in the electrolyte. The protons migrate towards the cathode and are there reduced back to hydrogen (or water if oxygen is present).

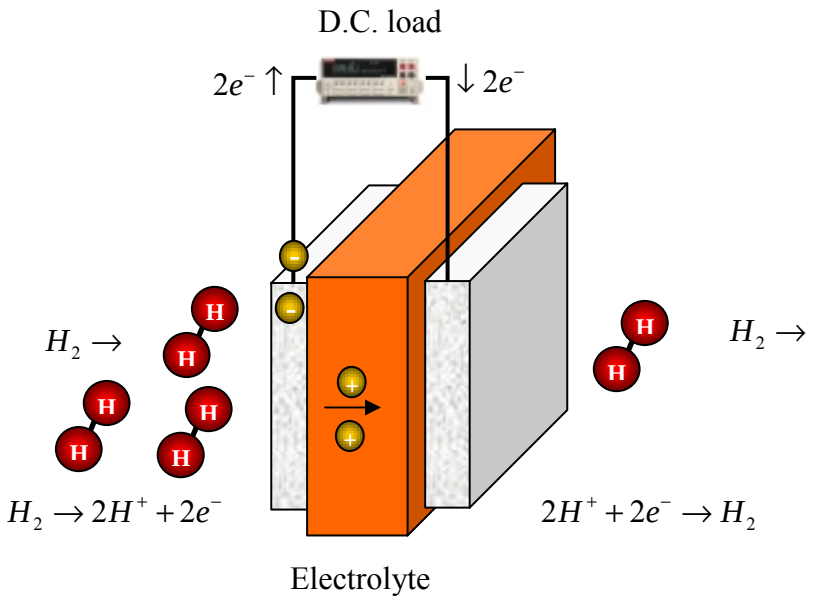

Figure 1.6. Schematic of solid state hydrogen pump or extractor.

1.3 Electrical Characterization

1.3.1 Impedance Spectroscopy

Impedance spectroscopy is a relatively new and powerful analytical tool for characterizing electrical properties of materials and their interfaces with electrodes. In contrast to D.C. measurements, impedance has the capability to distinguish different responses contribution to the total resistance. Ideally, each process (e.g., proton hopping in the grain) has associated with it a unique time constant that can be resolved in the frequency domain. Impedance measurements are commonly conducted in a symmetric cell configuration, denoting two identical electrodes applied to the faces of the sample with uniform gases on both sides. The general approach is to apply a small electrical perturbation voltage, $v(t) = V_0 \sin(wt)$, and to measure the response,

$i(t) = I_0 \sin(wt + \theta)$. In a linear system the phase shift and amplitude of the resulting current are measured at each given frequency over a wide range (10^{-3} to 10^6 Hz). Analogous to the D.C. resistance defined by Ohm's law, the A.C. impedance can be written as the ratio of the A.C. voltage to the A.C. current in the frequency domain.

$$Z(j,w) = \frac{V_0 e^{jwt}}{I_0 e^{j(wt+\theta)}} = Z_0 e^{-j\theta} \tag{1.15}$$

The complex impedance is typically represented in a Nyquist plot, where the imaginary part of the impedance is plotted as a function of the real part. Figure 1.7 provides an example of a Nyquist plot containing three distinctive processes. Each process appears as an arc, and can be modeled with an appropriate equivalent circuit. It is also important to note that the frequency is implicit in the Nyquist plot and is increasing towards the origin on the real axis.

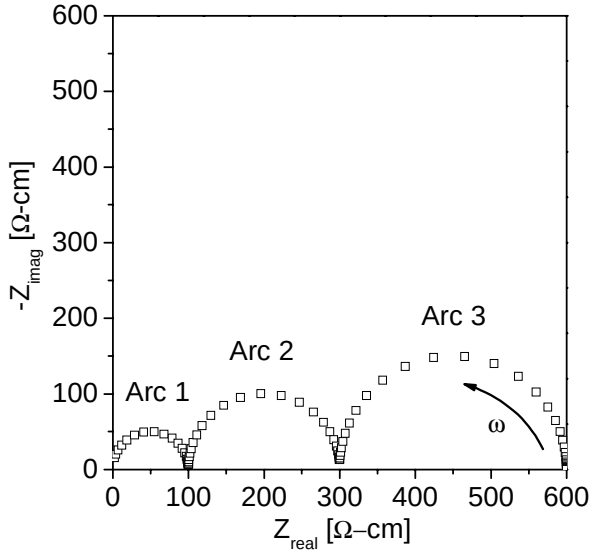

Figure 1.7. Example of Nyquist plot for three unique processes.

In polycrystalline materials, the three processes are typically assigned grain interior (Arc 1), grain boundary (Arc 2), and electrode (Arc 3) responses with decreasing frequency. The

assignments will be further discussed below with the "brick layer model." The angular frequency corresponding to the maximum of each arc is the characteristic frequency, ω_0, or time constant, $1/\omega_0$, of the process. The characteristic frequency is a material constant and independent of sample geometries.

$$\omega_0 = \frac{1}{RC} \tag{1.16}$$

The "brick layer model," Figure 1.8, was adopted to optimize the full extent of information that can be extracted from the measured electrical data [18]. In the model grains are assumed to be cube shaped with flat grain boundary layers between them.

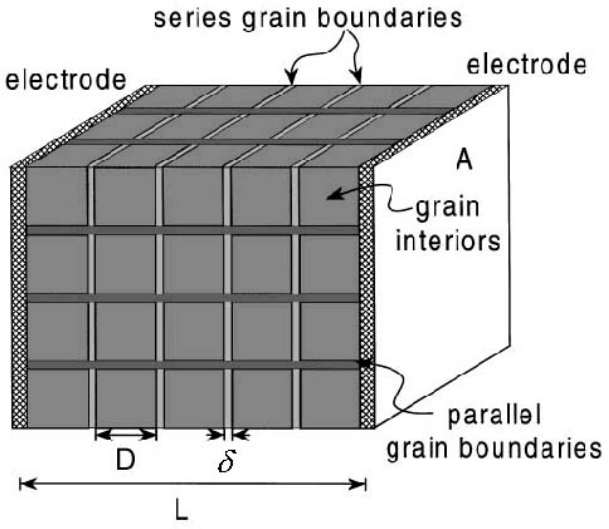

Figure 1.8. "Brick layer" model of a polycrystalline material [18].

In Figure 1.8, L is the sample length, A is the sample cross sectional area, D is the average grain size, and δ is the average grain boundary thickness. The procedure for calculating grain interior and specific grain boundary conductivity from the "brick layer model" is reviewed in detail in ref 18. For the case when $\sigma_{gi} > \sigma_{gb}$ and $\delta << D$, the current will follow the grain interiors only passing through the series grain boundaries as a mean to get from one grain to another. This will result in

two distinguishable arcs, where the high frequency arc is assigned to the grain interior and the low frequency arc is identified as the total grain boundary response.

From the Nyquist plot, the resistance due to the grain interior and total grain boundary can be easily extracted. Given that the characteristic frequencies are sufficiently different from one another, a complete semi-circular arc can be seen and the diameter reveals the resistance for that specific process. With knowledge of sample dimensions (thickness, L and area, A), the resistivity, ρ, and the conductivity, σ, can be calculated, Eq. (1.17).

$$\sigma = \frac{1}{\rho} = \frac{L}{RA} \tag{1.17}$$

The total grain boundary conductivity obtained from this simple calculation is a measure of both the grain boundary geometry (i.e. sample microstructure) and the inherent properties of the grain boundaries. To resolve the specific grain boundary conductivity (independent of microstructure), one requires some microstructural model as well as microstructural information (grain size and grain boundary thickness). The specific grain boundary conductivity, $\sigma_{sp.gb}$, is determined using the approximation:

$$\sigma_{sp.gb} = \frac{L}{A}\left(\frac{C_{bulk}}{C_{gb}}\right)\frac{1}{R_{gb}} \tag{1.18}$$

where C is capacitance and R is the resistance. With this approximation, it is assumed that the dielectric constants are equal in the grain interior and grain boundary. Resulting in the ratio of the capacitances being equal to the ratio of grain boundary thickness, δ, to average grain size, D.

$$\frac{C_{gi}}{C_{gb}} = \frac{\frac{A}{L}\varepsilon_{gi}\varepsilon_0}{\frac{A}{L}\frac{D}{\delta}\varepsilon_{gb}\varepsilon_0} = \frac{\delta}{D} \tag{1.19}$$

The unique processes (arcs) of the polycrystalline materials are modeled as RC circuits in series as shown in Figure 1.9. For each arc in the Nyquist plot, the resistor describes the

resistance of the process to a moving charge, while the capacitance describes the dielectric response of the process.

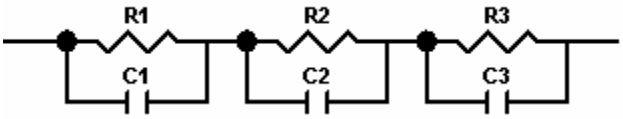

Figure 1.9. Example equivalent circuit to model a three-process system.

When resistors, capacitors, and inductors are combined in an A.C. circuit, the impedances of the individual components can be combined in the same way that the resistances are combined in a D.C. circuit. Time-varying relationships for the circuit elements are Fourier or Laplace transformed into the frequency domain, Table 1.2, to be used to derive impedances.

Table 1.2. Summary of time and frequency dependent relationships of voltage and current.

Circuit Element	**Time dependent relationship**	**Frequency dependent relationship**
Resistor	$\Delta v(t) = R\Delta i(t)$	$Z(j,w) = R$
Capacitor	$\Delta i(t) = C\frac{d(\Delta v(t))}{dt}$	$Z(j,w) = \frac{1}{jwC}$
Inductor	$\Delta v(t) = L\frac{d(\Delta i(t))}{dt}$	$Z(j,w) = jwL$

For non ideal situations (real world materials), material properties are continuously distributed (with a distribution of relaxation times) over a wide range. To account for the distributed microscopic properties, constant phase element (CPE) which exhibit more complicated frequency response provide a more satisfying model. For example, distributed properties include grain boundaries containing surface defects, roughness, charge

inhomogeneities, compositional variance, stoichiometry differences, and/or impurity phases. The impedance of the CPE is defined in Eq. 1.20 with two fitting parameter. The effective capacitance is Y, while the n parameter can have a value between 0 and 1, where 1 denotes an ideal capacitor.

$$Z(jw) = \frac{1}{(jw)^n Y} \tag{1.20}$$

The real capacitance can be calculated from the CPE using Eq. 1.21.

$$C = Y^{\frac{1}{n}} R^{(\frac{1}{n}-1)} \tag{1.21}$$

Nyquist plots ($-Z_{imag}$ vs. Z_{real}) of doped barium zirconate with silver electrodes and water saturated nitrogen atmosphere are shown in Figure 1.10. Only at the lowest temperatures (<150 °C) do the spectra clearly display a high frequency arc (grain interior) that extends to the origin. This grain interior arc is no longer accessible at higher temperatures due to the limitations of the frequency response analyzer. This mid-frequency arc (second arc) is attributed to grain boundary processes. At the very lowest frequencies, arc three is assigned to the electrode. At temperatures greater than about 450 °C, the spectra only reflects the electrode processes and only the displacement of the spectra from the real axis provides any measure of the total electrolyte resistance. In the absence of lower temperature data, misinterpretation of the type of spectra could easily occur. For example, the lower frequency feature of the electrode response could incorrectly be attributed to the grain boundary response, and the electrolyte resistance overestimated.

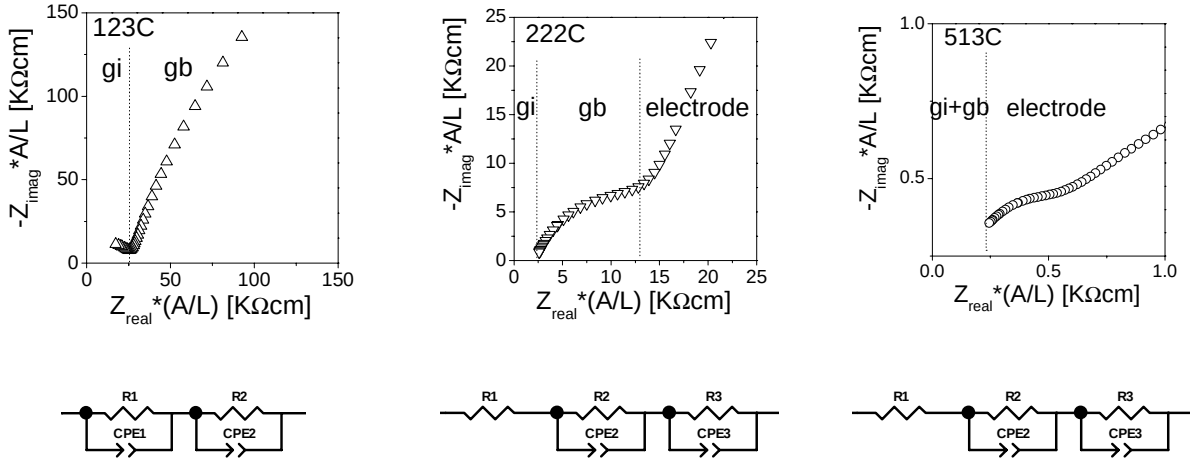

Figure 1.10. Nyquist plot of doped barium zirconate for 123, 222, and 513 ºC with appropriate equivalent circuit for modeling (Ag electrodes in wet nitrogen).

1.3.2 Electromotive Force Measurements (EMF)

Electromotive force measurements are employed to obtain an ionic transport number, the quotient of the current carried by an ionic component and the total current. A voltage can be generated by exposing the two electrode surfaces (on opposite side of an electrolyte in a sealed chamber) to different partial pressures of hydrogen. Specifically, for barium zirconate studies, one surface was exposed to water saturated hydrogen and the other to water saturated compressed air: H_2, H_2O, Pt | sample | Pt, H_2O, Air.

The governing chemical reaction in this case is simply hydrogen and oxygen combining to form water:

$$H_2 + \frac{1}{2}O_2 \rightarrow H_2O\,, \tag{1.22}$$

where the equilibrium constant of the reaction can be written as

$$K_{rxn} = \frac{P_{H_2O}}{P_{H_2} P_{O_2}^{1/2}}\,. \tag{1.23}$$

The theoretical or Nernstian voltage, E_N, expected from a hydrogen partial pressure gradient across the cell is shown in Eq. (1.24) with the convention of a positive EMF value for spontaneous reactions.

$$E_N = \frac{-\Delta G}{nF} = \frac{RT}{2F} \ln\left(\frac{P_{H_2}^{anode}}{P_{H_2}^{cathode}} \right) \tag{1.24}$$

where R is the universal gas constant, T is temperature, F is Faraday's constant and $P_{H_2}^{anode}, P_{H_2}^{cathode}$ are the partial pressures of hydrogen in the anode and cathode chambers. Using the equilibrium constant, Eq. (1.25), and the standard EMF of the cell reaction (T = 273 K, P = 1 bar), Eq. (1.26),

$$E_0 = \frac{|\Delta G_0|}{nF} = \frac{RT \ln K_{rxn}}{nF}. \tag{1.25}$$

The Nernstian voltage, E_N, becomes

$$E_N = E_o + \frac{RT}{2F} \ln\left(\frac{P_{O_2}^{0.5} P_{H_2}}{P_{H_2O}} \right), \tag{1.26}$$

where $P_{H_2}, P_{O_2}, P_{H_2O}$ are the partial pressures of hydrogen, oxygen, and water respectively.

The ionic transport number can be calculated from the ratio of the measured EMF to this Nernstian value, $t_{ion} = E_{meas}/E_N$.

1.4 Motivations and Objectives

In literature, early misinterpretation of data and poorly established processing conditions suggested doped barium zirconate exhibited poor proton conductivity, especially as compared to the easily processed (and more popular) doped barium cerate. Our motivations are as follows:

1. Closely examine the proton transport and determine the causes responsible for the poor reproducibility of electrical data in literature. Develop a methodology to produce high density, doped barium zirconate with reproducible electrical characteristics. Substantiate the highest reported conductivity in literature and correlate stoichiometric changes with proton conductivity.
2. Investigate hydrogen transport across grain boundaries, with the aim of optimization of total conductivity.
3. Study the effects of dopant concentration levels on stability, charge carrier concentration, hydration enthalpies, hydration entropies, and conductivity. Report the existence or lack of proton-dopant associations in proton conducting perovskites.
4. Explore alternative densification procedures with the use of sintering aids. Characterize the effects of the sintering aid on sintering, microstructure, chemical stability, and electrical properties.
5. Demonstrate the viability of doped barium zirconate as a membrane in electrochemical devices by the fabrication and successful operation of a fuel cell. Explore and optimize potential electrode materials for both the anode and cathode.

1.5 References

1. T. Pagnier, I. Charrier-Cougoulic, C. Ritter, G. Lucazeau. A neutron diffraction study of $BaCe_xZr_{1-x}O_3$. *The European Physical Journal Applied Physics* **9**, 1. ICSD database code 90049 (2000).

2. K. D. Kreuer, S. Adams, W. Munch, A. Fuchs, U. Klock, and J. Maier. Proton conducting alkaline earth zirconates and titanates for high drain electrochemical applications. *Solid State Ionics* **145,** 295 (2001).

3. F. A. Kroger and H. J. Vink. Relations between the concentrations of imperfections in crystalline solids, pages 307–435, in *Solid State Physics: Advances in Research and Applications*, vol. 3, edited by F. Seitz and D. Turnbull. Academic Press, New York, (1956).

4. H. Iwahara, T. Esaka, H. Uchida, and N. Maeda. *Solid State Ionics* **3/4,** 359 (1981).

5. H. Iwahara, H. Uchida, K. Ono, and K. Ogaki. Proton Conduction in Sintered Oxides Based on $BaCeO_3$. *J. Electrochem. Soc.* **135**, 529 (1988).

6. R. C. T. Slade and N. Singh. Generation of Charge-Carriers and an H/D Isotope Effect in Proton-Conducting Doped Barium Cerate Ceramics. *J. Mater. Chem.* **1**, 441 (1991).

7. K. D. Kreuer. On the development of proton conducting materials for technological applications. *Solid State Ionics* **97**, 1 (1997).

8. M. Cherry, M.S. Islam, J. D. Gale, and C. R. A Catlow. Computational studies of proton in perovskite structured oxide. *J. Phys. Chem.* **99**, 14614 (1995).

9. W. Munch, G. Seifert, K. D. Kruer, and J. Maier. A quantum molecular dynamics study of the cubic phase of $BaTiO_3$ and $BaZrO_3$. *Solid State Ionics* **97**, 39 (1997).

10. K. D. Kreuer. Proton-Conducting Oxides. *Annu. Rev. Mater. Res.* **33**, 333 (2003).

11. M. Cherry, M.S. Islam, J. D. Gale, and C. R. A Catlow. Computational studies of proton migration in perovskite oxide. *Solid State Ionic* **77**, 207 (1995).

12. K. H. Ryu and S. M. Haile. Chemical stability and proton conductivity of doped $BaCeO_3$–$BaZrO_3$ solid solutions. *Solid State Ionics* **125**, 355 (1999).

13. T. Uda, P. Babilo, and S. M. Haile. Thermodynamic Analysis and conductivity of yttrium doped barium zirconate. 207th ECS Meeting, Quebec City, Canada (2005).

14. H. Iwahara, T. Yajima, T. Hibino, K. Ozaki, and H. Suzuki. Protonic conduction in calcium, strontium and barium zirconates. *Solid State Ionics* **61**, 65 (1993).

15. T. Yajima, H. Suzuki, T. Yogo, and H. Iwahara. Protonic conduction in SrZrO3-based oxides. *Solid State Ionics* **51**, 101 (1992).

16. K. D. Kreuer. Aspects of the Formation and Mobility of Protonic Charge Carriers and the Stability of Perovskite-Type Oxides. *Solid State Ionics* **125,** 285 (1999).

17. H. G. Bohn and T. Schober. Electrical Conductivity of the High-Temperature Proton Conductor $BaZr_{0.9}Y_{0.1}O_{2.95}$. *J. Am. Ceram. Soc.* **83,** 768 (2000).

18. S. M. Haile, D. L. West, and J. Campbell. The role of microstructure and processing on the proton conducting properties of gadolinium-doped barium cerate. *J. Mater. Res.* **13**, No. 6, 1576 (1998).

19. N. Q. Minh and T. Takahashi, in *Science and technology of Ceramic Fuel Cells*. Elsevier Science, Netherlands, (1995).

20. J. R. MacDonald and W. B. Johnson, in *Impedance Spectroscopy*, edited by J. R. MacDonald. Wiley and Sons, New York, (1988).

21. A.J. Bard and L.R. Faulkner, in *Electrochemical Method.* Wiley and Sons, New York, (2001).

Chapter 2: Experimental Methods

2.1 Synthesis and Processing of Powders

2.1.1 Synthesis Methods

Two main routes are common for the synthesis of inorganic oxides: solid state methods and chemical solution method.

Solids state reaction is the easier and more common method for syntheses of traditional multicomponent oxides. The underlying concept is the mixture of carbonates and oxides (as starting materials) elevated to high temperatures to allow for the diffusion of cations in the creation of a new phases. In the specific case of doped barium zirconate, starting materials included barium carbonate ($BaCO_3$), zirconium oxide (ZrO_2), and yttrium oxide (Y_2O_3). Raw materials were mixed in the appropriate molar ratios, Eq. (2.1), and ball milled (up to 24 hrs) using stabilized zirconia media in isopropyl alcohol. Powder was then dried, uniaxially pressed, and calcined to 1300 °C for 10 hrs. Upon cooling the pellet was crushed, ball milled (up to 24 hrs), and again calcined to 1300 °C for 10 hrs. This procedure was repeated three or four times (as needed) to obtain a single phase perovskite structure.

$$BaCO_3 + (0.80)ZrO_2 + (0.10)Y_2O_3 \rightarrow BaY_{0.20}Zr_{0.80}O_{2.9} + CO_2 \uparrow \qquad (2.1)$$

Although this technique is simple and easily accomplished, it has several significant disadvantages. Multiple high temperature sintering steps as well as long hours of milling leads to barium deficiency in the sample by way of BaO evaporation or Zr impurities from the milling media. Solid state reactions often results in inhomogeneous and contaminated products.

Chemical solution methods provide molecular-level of mixing of the elements, reducing diffusion pathways and providing a more homogeneous and stoichiometric crystalline powders. Majority of powders in this work were synthesized in two forms: glycine-nitrate combustion and modified Pechini method.

Glycine-nitrate combustion synthesis process (GNP) [1] is overall a quicker route to obtaining the crystalline powders. In this process the glycine is utilized for (1) complexing with the metal ions and (2) serving as the fuel for the combustion reaction. Due to the glycine's unique character of having both a carboxylic acid group and an amine group, it is able to complex metal ions of varying sizes. The GNP combustion avoids generating second phases and produces desired powders, that are high surface area and compositionally homogeneous, due to its rapid reaction and high temperatures (flame temperatures are recorded 1000–1450 ºC [1]). Doped barium zirconate starting materials included high purity $Ba(NO_3)_2$, $Y(NO_3)_3 \cdot 6H_2O$, and $ZrO(NO_3)_2 \cdot xH_2O$, where x was determined by thermogravimetric analysis. To prepare the crystalline powders, the appropriate molar ratios of nitrates and glycine (NH_2CH_2COOH) were mixed in a minimum volume of deionized water to obtain a transparent solution. A glycine to nitrate ration of 1:2 (and in some cases 1:3) was used. The aqueous solution was dehydrated on a hot plate at a temperature of 150 °C generating a viscous liquid. Upon complete evaporation of the water, the viscous liquid autoignited to produce the desired powders. After autoignition, powders were usually calcined at 1200 °C for 5 hrs to yield well-crystallized BYZ powders. The glycine-nitrate combustion synthesis tends not to be appropriate for the synthesis of oxides with metals that have multiple oxidation states. These metals combust violently during the autoignition, leading to stoichiometric changes in the powder.

Modified Pechini process is an effective method to synthesis multioxidation state metal oxides, and was used for potential electrode materials such as $BaCo_xPr_{1-x}O_3$. In this method, metal ions are complexed in an aqueous solution with an α-hydroxycarboxylic acid such as citric acid. Upon heating the chelate (complexing agent with metal ions), it undergoes polyesterification producing a gel-like resin. The resin is further decomposed by heating to remove organics. Specific instructions include the dissolving the appropriate starting material nitrates in water. In the event of nitrates not readily dissolving, few milliliters of nitric acid can be added along with

heat. To the dissolved solution was added an ethylenediaminetetraacetic acid (EDTA) solution and citric acid. EDTA solution, citric acid, and total metal ion ratio of 1:2:1 was used. The EDTA solution consisted of EDTA and ammonium hydroxide with a 1:2.5 molar ratio. Evaporation of water and polymerization occurred upon mild heating in an oven overnight, and the resulting char was calcined at 900-1100 °C (depending on the material) for 5-10 hrs.

2.1.2 Preparation of High-density Pellet

Synthesized barium zirconate fine powders were attritor milled at 500 rpm for 5 hrs to produce uniform particles (<100 nm). Subsequently, using an agate mortar, powers were mixed with a binder solution consisting of 200 mL of water, 2 g of polyvinyl alcohol (PVA), 1 ml of glycerin, and 10 mL of ethanol. The ratio of binder solution to powder oxide was approximately 1:7 by mass. The granulated power was then passed through a 100 mesh sieve to remove agglomerates larger than ~150 μm. Green pellets were obtained by uniaxial pressing under a pressure of 400 MPa for 1 min. On firing, the binder was removed by holding the pellets at 600 °C (ramp of 1 °C/ min) under ambient air for a period of 30 min. In the final sintering step, samples were surrounded by a powder mixture of barium zirconate and small amount of $BaCO_3$ (about 10% by mass) as shown in Figure 2.1. Sintering was carried out under flowing oxygen at 1600 °C (ramp of 5 °C/min to 1000 °C, followed by a ramp of 1 °C/min) for a period of 4 to 24 hrs.

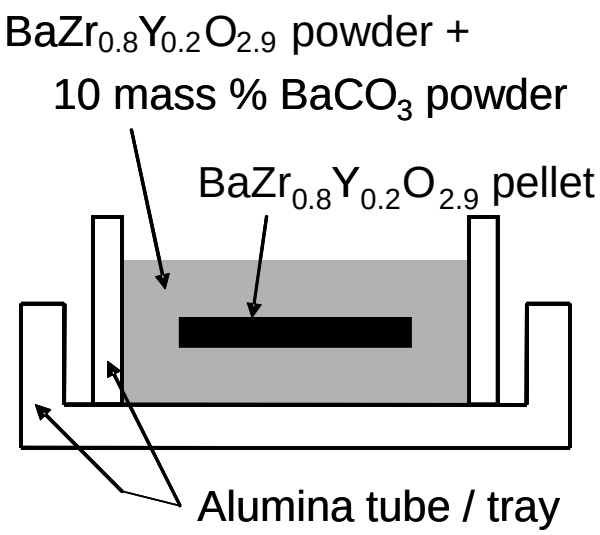

Figure 2.1. Schematic diagram of the sintering configuration: BYZ20 green pellet covered with a powder mixture of BYZ20 and $BaCO_3$ (about 10 mass%).

2.2 Characterization Techniques

2.2.1 Common Materials Characterization Techniques

A variety of traditional materials characterization techniques were utilized to exam doped barium zirconate and other perovskites of interest. Below is a brief summary of techniques used and appropriate descriptions.

Densification measurements were performed in three ways: direct measurements of sample dimensions and weight, by the Archimedes method using deionized water as the immersion medium, and linear shrinkage after sintering. Total linear shrinkage [$(l - l_O)/l_O$, where l_O is the initial length and l is the final length] resulting from sintering was established from direct measurements of sample dimensions before and after sintering. Dilatometry experiments, permitting *in situ* measurements of linear shrinkage as a function of temperature, were performed with a Dilatronic dilatometer (Theta Industries, NY) as well as a Linseis L75V1550 dilatometer (Linseis, NJ). Data were collected at a heating rate of 3 °C /min under variety of atmospheres (nitrogen, air, and oxygen).

The x-ray diffraction (XRD) analyses of calcined powder samples were performed at room temperature using a Phillips diffractometer (X'Pert Pro) with Cu Kα radiation. Intensities were obtained in the 2θ range between 20 and 80 ° with a step size of 0.02 ° and a measuring time of 3 sec at each step. In addition to phase analysis, x-ray patterns were also utilized to determine cell parameters by Rietveld refinement as implemented in the X'Pert Plus software.

The microstructure and chemical composition of sintered samples were investigated by means of scanning electron microscopy (LEO 1550VP Field Emission SEM) in conjunction with EDS (Energy Dispersive x-ray Spectroscopy, Oxford INCA Energy 300). Exposed top surface of the sample was polished in preparation for chemical analysis. The Oxford INCA EDS software employs the PAP (Pouchou and Pichoir) model for quantitative analysis [2] in which fundamental factors are used to correct for the effects of atomic number, absorption, and fluorescence to the measured intensity of the elements. Accordingly, standards are not necessary.

Quantitative elemental microanalyses were conducted with a JEOL 8200 electron microprobe operated at 15 kV and 25 nA in a 10 μm beam mode. Quantitative measurements of the average chemical composition were obtained for a variety of samples. Unless other wise stated, zircon, yttrium phosphate, and barium titanate were used as standards for the analysis. Characteristic x-ray emission intensities were converted to chemical weight percents using the program CITZAF [3].

In order to assess chemical stability and water incorporation, thermogravimetric analysis (TGA) of selected samples was conducted using a Netzsch STA 449 C Jupiter. The TGA allows for the precise measurement of weight loss (or gain) as a function of temperature. Chemical stability test were performed under flowing CO_2 (P_{CO2}=0.20). For this purpose, samples were lightly sintered to a density of 60%–65% of theoretical. In addition, high surface area powder samples were also tested to forgo sluggish kinetics of pellet samples. To measure and quantify the water incorporated into the perovskite structure, powder sample were heated and dried at 1000 °C in dry nitrogen. Sample were then exposed to wet nitrogen (P_{H2O}=0.023) and cooled in 100 °C

increments to room temperature with 2 hrs stabilization time at each temperature. Weight gain due to water incorporation into the structure, as described in Chapter 1, was measured.

2.2.2 Impedance Spectroscopy Station and Reactor

The conductivity of sintered BYZ pellets was measured by impedance spectroscopy over the frequency range 10^2 to 10^6 Hz using a HP 4284A LCR meter with an applied A.C. voltage amplitude of 50 mV. Earlier studies were conducted with an applied voltage of 500 mV; however this higher perturbation amplitude did not influence the results for the barium zirconate system. Silver electrodes were applied onto the surfaces of polished samples by brush painting colloidal silver paint (#16032, Ted Pella, CA). Water was incorporated into the samples by exposure to water-saturated nitrogen (p_{H2O} = 0.031 atm) at 300 °C for 8 hrs. Data were collected under H_2O-saturated nitrogen (p_{H2O} = 0.031 atm) over the temperature range of 75 to 600 °C in 25 °C intervals with an equilibration time of 30 min before each measurement. The resulting impedance spectra were analyzed in terms of an equivalent circuit model using the software package Zview (Scribner Associates, NC). The above procedure was followed to gather all data presented unless otherwise noted in the text.

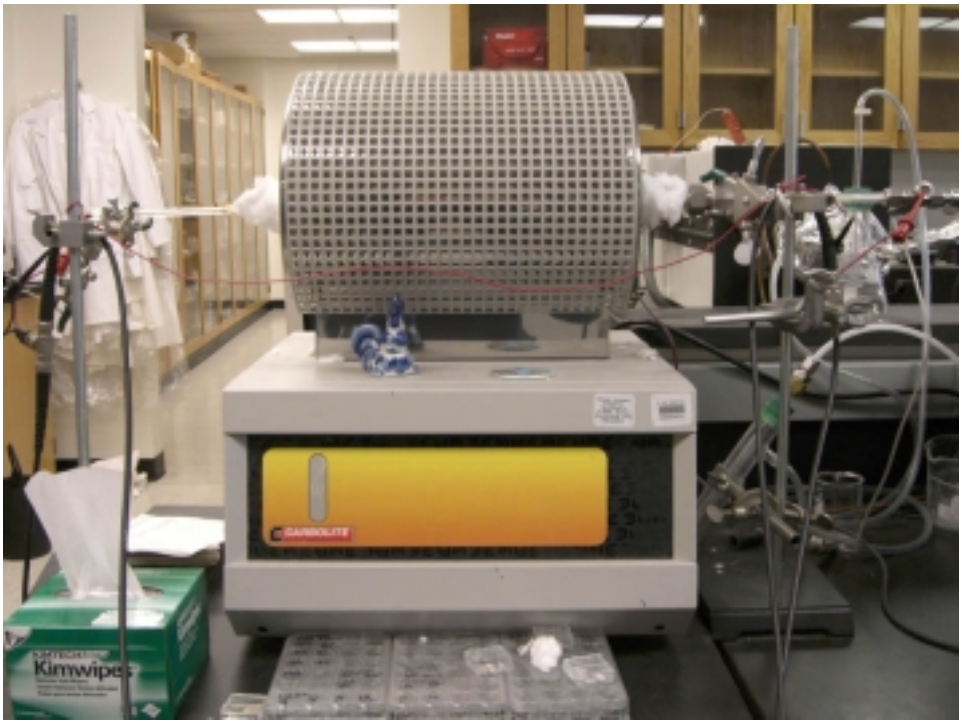

Figure 2.2. Impedance furnace and reactor.

The impedance spectroscopy station, Figure 2.2, consisted of a Carbolite furnace (MTF 9/38/250) controlled with a Eurotherm 2416 controller, HP LCR meter (# 4284A), and custom built reactor, shown in Figure 2.3. All control and output signals were controlled and collected via NI Labview programs.

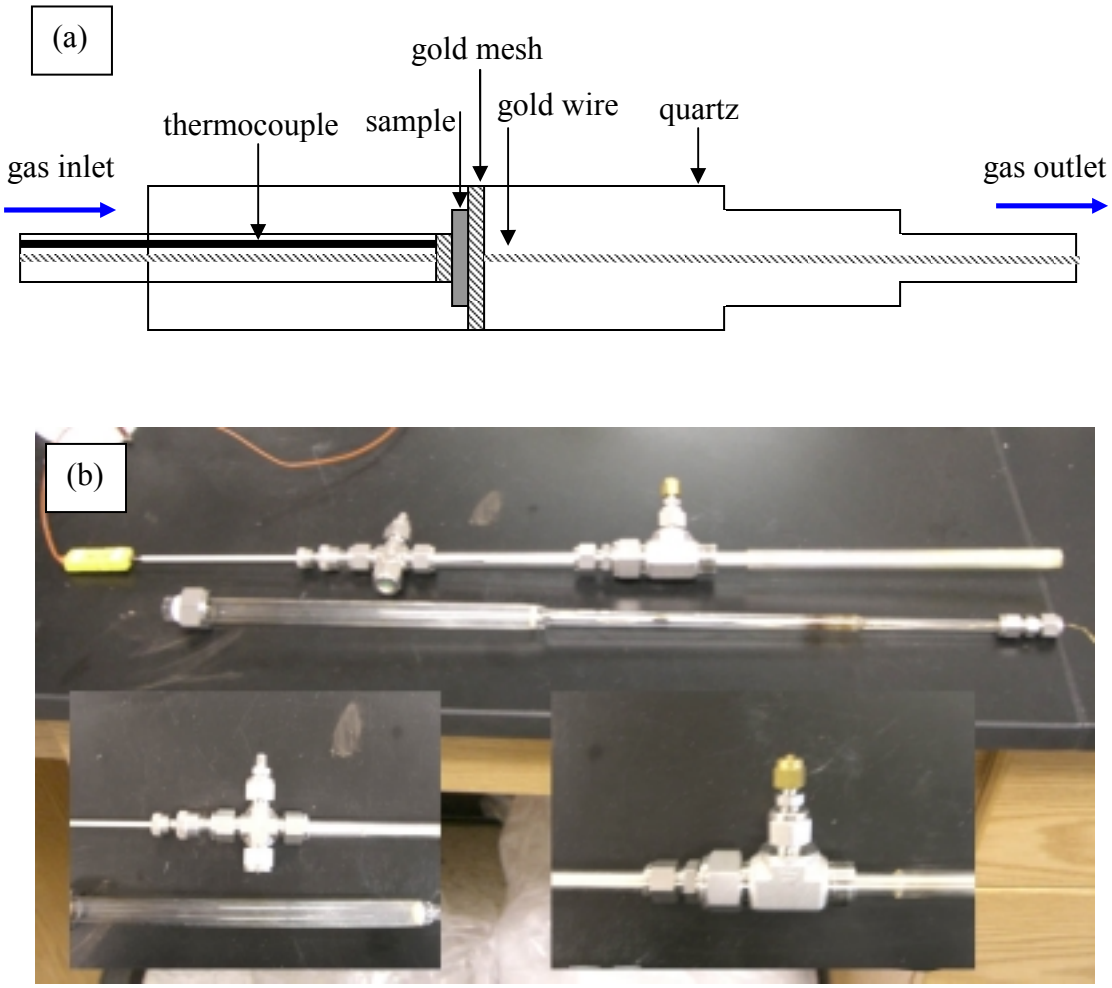

Figure 2.3. Impedance reactor design as a (a) schematic diagram and (b) photograph.

Electrode studies were conducted using either a Solartron 1260 Impedance analyzer or Autolab PGSTAT100 analyzer (Eco Chemie). Data were collected over the frequency range 10^{-3} to 10^{6} Hz in a variety of oxygen partial pressures. Metal electrodes (Pt: Heraues CL11-5349, Pt: Engelhard 6082, Ag: Ted Pella 16032, Pd: ElectroScience 9647) were brush painted over polished pellets. Electrode measurements were completed using the fuel cell reactor, which will be detailed in following section.

2.2.3 Fuel Cell Station and Reactor

The ionic transport number was obtained from electromotive force (EMF) measurements. For these measurement, porous Pt electrodes (# CL11-5349, Heraeus, PA) were pasted onto the surfaces of thick BYZ20 pellet and fired at 1100 ºC (5 hrs under ambient air). Pt current leads were attached to the sample. The sample was affixed to the end of a alumina tube with a gas-tight ceramic paste seal (Aremco Ceramabond 552). By exposing one electrode surface to water saturated hydrogen and the other to water saturated compressed air (P_{H2O} = 0.031 atm) a voltage was generated. The ionic transport number was estimated from the ratio of the measured potential to the calculated Nernstian value, $\langle t_{ion} \rangle = E_{meas}/E_N$ (as described in Chapter 1). This measurement does not distinguish between oxygen ion and proton conduction, but rather gives a total ionic transference number.

Fuel cell polarization tests and electrode studies were conducted using a custom build fuel cell test station, Figure 2.4, by former postdoctoral fellow Tetsuya Uda. This test station includes Carbolite furnace (HST 12/--/600); Keithley 2420 source meter; mass flow controllers (MKS PR 4000) for both anode and cathode chambers; humidification oven to control water partial pressure; Agilent data logger (34970A) to collect temperature, pressure, humidity, and flow rate; custom reactor, shown in Figure 2.5; and all controls were operated using NI Labview programs.

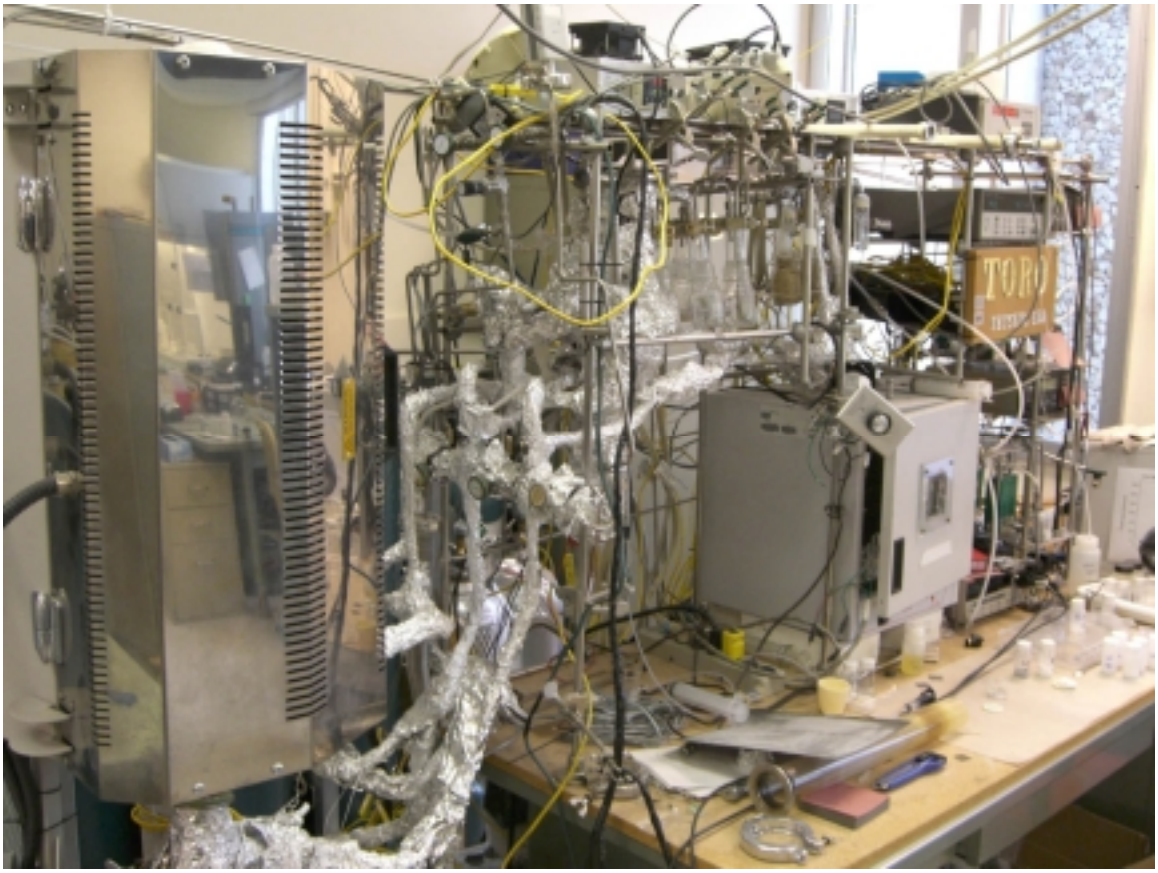

Figure 2.4. Fuel cell testing station.

The fuel cell test reactor, shown in Figure 2.5, does not have anode and cathode chambers entirely sealed from one another; the configuration is designed for rapid examination of fuel cells and electrocatalysts at the expense of slight voltage drops due to gas phase transport between fuel and oxidant chambers. The electrolyte pellet was mechanically supported by an alumina ring, Figure 2.6, to which it was attached using alumina cement. This assembly was then sandwiched between two wider inconel rings, each of which was equipped with a gas inlet at its center and a gas outlet near its edge. A photograph of the assembled fixture, including compression plates used to improve separation of the anode and cathode gases, is also shown in Figure 2.5. Silver paste was painted on the surfaces of the thin pellet and the Inconel rings in order to obtain good electrical contacts. Inconel tubes for supplying and exhausting gas also served as current and

potential leads. A four-probe method was adopted in order to eliminate effects due to voltage drops at the inconel tubes.

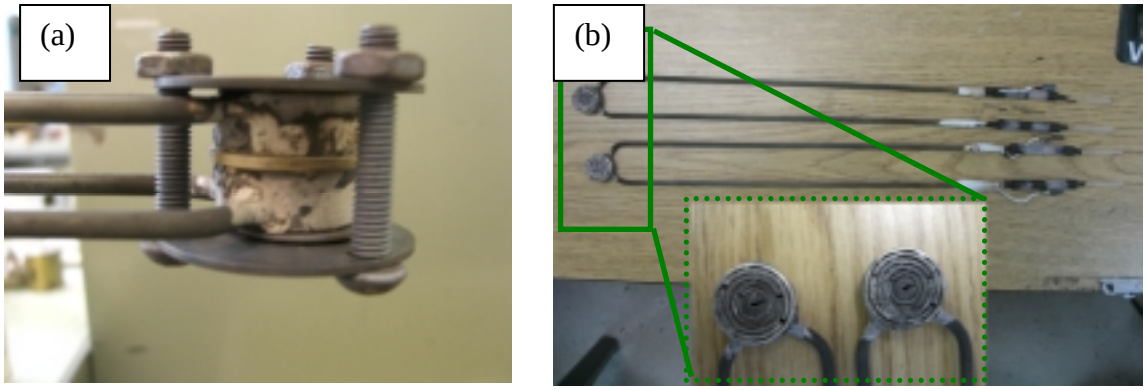

Figure 2.5. Photograph of the (a) assembled fixture, including compression plates and (b) Inconel rings and tubing for gas inlet/outlet and electrical leads.

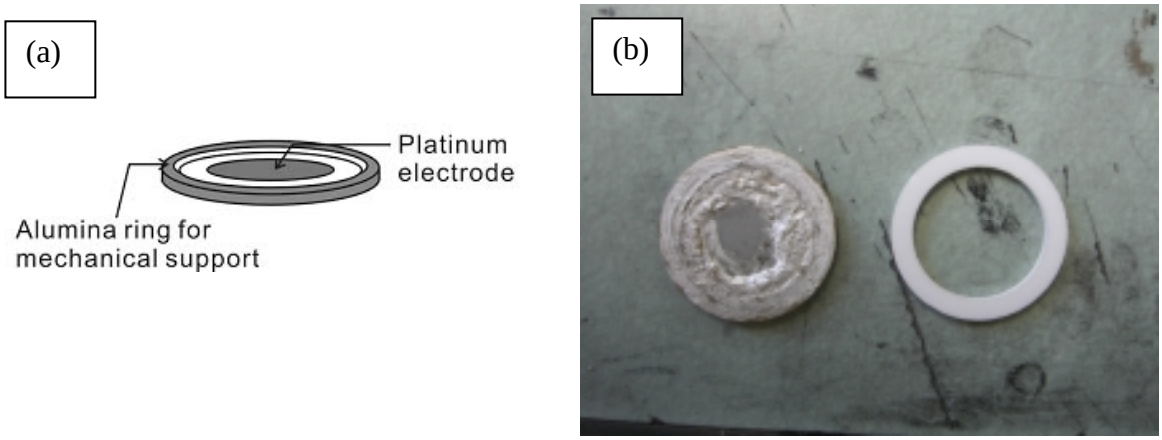

Figure 2.6. Membrane electrode assembly as (a) a schematic diagram and (b) photograph.

The test fixture was placed in a tube furnace and an oxygen partial pressure gradient generated across the fuel cell by supplying humidified hydrogen to the anode and humidified oxygen or humidified air to the cathode. The gas flow rates were 100 standard mL/min, and the water partial pressure was maintained at 0.031 atm by passing the gases through water held at 25 °C. The total pressure of each chamber was kept at ambient levels (~1 atm).

2.3 Cell Fabrication

In preparation of electrode deposition, samples were masked, Figure 2.7. Metal electrodes were deposited by paint brushing. Platinum ink, silver ink, and palladium ink (details as above) were used as both anode and cathode electrocatalysts. Curing temperatures and heating rates are summarized in Table 2.1. The curing process was carried out under stagnant air.

Table 2.1. Summary of metal electrodes curing temperature.

Ink	Manufacturer	Optimal curing temperature [ºC]	Optimal heating rate [ºC/min]
Pt	Heraues CL11-5349	1100	2
Pt	Engelhard 6082	900	2
Ag	Ted Pella 16032	25	--
Pd-Ag	ElectroScience 9647	850	2

In the case of inorganic non-metal electrodes (Ni-BYZ cermet for anode or perovskite cathodes), colloidal solutions were prepared. Electrode powders and isopropanol solvent with concentration of 0.005 g/mL was utilized. Solution was deposited with a pressure of 15 psi, 2-3 inches from the surface, and perpendicular to the support. For optimal results, hot plate temperature was set to 95 °C, slightly above the boiling temperature of isopropanol. This allowed for the electrode particles to deposit wet and instantaneously dry as the solvent evaporated.

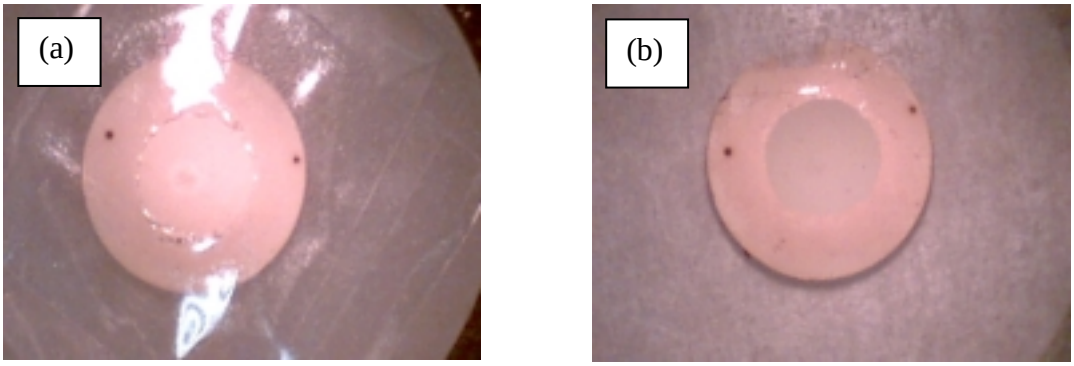

Figure 2.7. (a) masking of barium zirconate pellet, and (b) NiO cermet electrode on BYZ.

2.4 References

1. L. A. Chick, L. R. Pederson, G. D. Maupin, J. L. Bates, L. E. Thomas, and G. J. Exarhos. Glycine-nitrate combustion synthesis of oxide ceramic powders. *Materials Letters* **10**, 6 (1990).

2. J. L. Pouchou and F. Pichoir, in *Quantitative analysis of homogeneous or stratified microvolumes applying the model "PAP" in Electro Probe Quantitation*, edited by K. Heinrich and D. Newbut. Plenum Press, pp. 31-75 (1991).

3. J. T. Armstrong. *Microbeam Anal.* **4,** 177 (1995).

Chapter 3: Processing of Yttrium-doped Barium Zirconate for High Proton Conductivity

3.1. Introduction

The conductivity of doped barium zirconate as reported from twelve independent groups, Table 3.1, [1–12] varies widely, from a low of ~1 x 10^{-6} to a high of 1 x 10^{-2} S/cm at 600 ºC. All data were collected using Pt electrodes with the exception of Mintharam [2] in which Ag electrodes were utilized. Iguchi [12] did not report the electrode material. The wide range of reported data introduces a major challenge for its implementation in any real device and raising fundamental questions regarding the proton transport mechanism.

The earliest studies of doped barium zirconate, which appeared in the early 1990s, suggested that this material exhibits poor proton conductivity as compared to doped barium cerate. Although their reported values differ by two orders of magnitude, Iwahara [1], Manthiram [2] and Slade [3] all agreed that the conductivity of the zirconate is no more than 1.2 x 10^{-4} S/cm at 600 ºC. The understanding of the properties of barium zirconate was revised substantially in 1999. In that year Kreuer [13] reported the conductivity of yttrium doped barium zirconate to be ~5 x 10^{-5} S/cm at just 140 °C and this was quickly confirmed by Bohn and Schober in 2000 [4]. In a later paper, Kreuer noted the poor reproducibility of conductivity measurements of barium zirconate [8] and argued that this is connected to the difficulty in fabricating polycrystalline compacts of the material.

In the present chapter, we explore the sample preparation steps that are responsible for this poor reproducibility and report a methodology for consistently obtaining high density, high conductivity barium zirconate with transport properties comparable to the best values reported in literature.

Table 3.1. Conductivity of doped $BaZrO_3$ as reported in the literature (conductivity of barium cerate also provided for comparison).

Composition	Sintering Conditions	Conductivity (Bulk or Total)*	Conductivity Measurement Conditions	Reference
$BaZr_{0.95}In_{0.05}O_{3-x}$	1500-1650 °C x 10hr in air	1.2x 10^{-4} S/cm (Total) at 600 °C	H_2 (wet)	1993 Iwahara [1]
$BaZr_{0.9}In_{0.1}O_{3-x}$	1350 °C x 40hr	5.0 x 10^{-5} S/cm(Bulk) at 600 °C	Wet N_2	1993 Manthiram[2]
$BaZr_{0.9}Y_{0.1}O_{3-x}$	1400 °C x 10hr in air	1.3 x 10^{-6} S/cm(Bulk) at 605 °C	Wet N_2, (room temperature water)	1995 Slade [3]
$BaZr_{0.9}Y_{0.1}O_{3-x}$	1715 °C x 30 hr in air	3.0 x 10^{-3} S/cm (Bulk) at 600 °C	Wet air	2000 Bohn [4]
$BaZr_{0.9}Y_{0.1}O_{3-x}$	1800 °C x 5hr in air	1.1 x 10^{-3} S/cm (Total) at 600 °C	Wet H_2, (p H_2O = 0.017 atm)	2000 Katahira [5]
$BaZr_{0.93}Y_{0.07}O_{3-x}$	1700 °C x 1hr	5x 10^{-4} S/cm (Total) at 600 °C	Wet air (room temperature water)	2001 Gorelov [6]
$BaZr_{0.95}Y_{0.05}O_{3-x}$	1350-1400 °C x 20-40hr in air	1.8 x 10^{-6} S/cm(Bulk) at 605 °C	Wet N_2, (p H_2O = 0.031 atm)	2002 Laidoudi [7]
$BaZr_{0.85}Y_{0.15}O_{3-x}$	1700 °C x 20hr	1.6 x 10^{-3} S/cm (Total) at 600 °C	Wet N_2 (p H_2O = 0.023 atm)	2003 Kreuer [8]
$Ba_{1.1}Zr_{0.9}Y_{0.1}O_{3-x}$ (10 % excess BaO before sintering)	1500°C x 24hr	9 x 10^{-4} S/cm (Total) at 500 °C	Wet air	2004 Snijkers [9]
$BaZr_{0.93}Y_{0.07}O_{3-x}$	1650 °C x 10hr in air	3.8 x 10^{-3} S/cm (Total) at 600 °C	Wet N2 (p H_2O = 0.025 atm)	2005 Wang [10]
		4.2 x 10^{-3} S/cm (Total) at 600 °C	Wet air (p H_2O = 0.025 atm)	
$BaZr_{0.9}Y_{0.1}O_{3-x}$	1400 °C	2.8 x 10^{-4} S/cm (Bulk) at 600 °C	Wet Ar-5%H_2, (p H_2O = 0.03 atm)	2005 Savaniu [11]
$BaZr_{0.95}Y_{0.05}O_{3-x}$	1800 °C	1.0 x 10^{-2} S/cm at 600 °C	Wet Ar + O_2, (p H_2O = 0.023 atm)	2006 Iguchi [12]
$BaCe_{0.9}Y_{0.1}O_{3-x}$	1700 °C x 10hr in air	1.1 x 10^{-2} (Total) at 600 °C	Wet H_2, (p H_2O = 0.017 atm)	2000 Katahira [5]

*Bulk conductivity refers to conduction through the grain interior portions of the sample only, whereas total refers to conduction through both the grain interiors and the grain boundaries.

3.2 Processing methodology

The specific composition selected in this study was $BaZr_{0.8}Y_{0.2}O_{3-\delta}$ (BYZ20). In order to obtain reproducible sintering behavior and electrical properties, a wide range of processing conditions were examined. Ultimately, it was found that both solid state and chemical synthesis were suitable so long as the crystallite size of the loose powder was reduced to the 50–100 nm range prior to densification. Samples prepared from powders obtained by a glycine-nitrate combustion synthesis process as described in Section 2.1. Powders were calcined at 1250 °C for 5 hrs to yield well-crystallized BYZ20, which were subsequently attritor milled at 500 rpm for 5 hrs to produce uniform particles with approximate size of 20–100 nm, as determined by scanning electron microscopy, Figure 3.1.

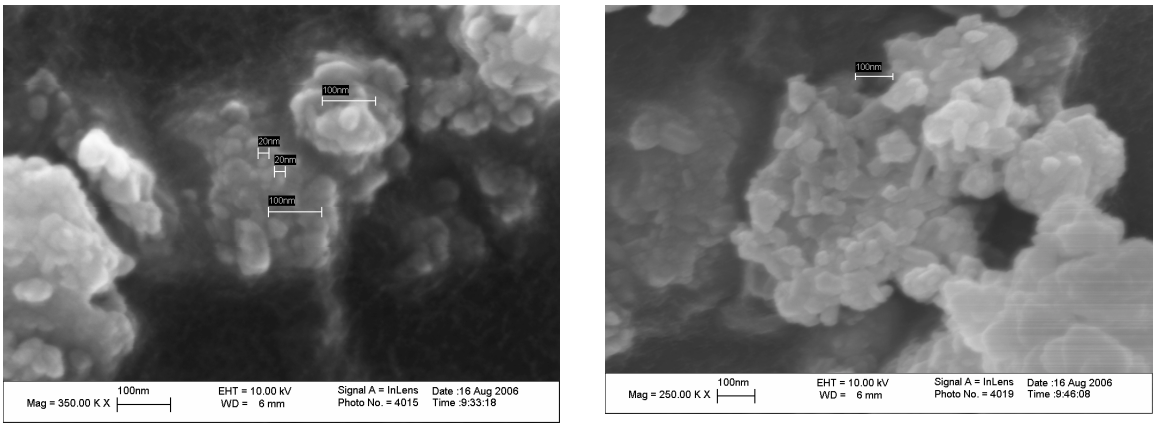

Figure 3.1. SEM micrograph of loose powders of processed barium zirconate.

Pellets were fabricated as detailed in Section 2.3. During sintering pellets were covered with excess barium zirconate to kinetically suppress Ba evaporation. To probe the effect of sintering procedure on conductivity, samples not enclosed in excess barium were also prepared. The two types of samples are hereafter referred to as “covered” and “uncovered” respectively.

3.3 Densification, Phase Formation, and Stoichiometry

The relative density, as determined by the Archimedes method, of (covered) sintered pellets of BYZ prepared by the careful procedures outlined above rose from 93% to 99 % (with respect to the density of undoped barium zirconate, 6.21 g/cm^3) with increasing sintering time Figure 3.2.

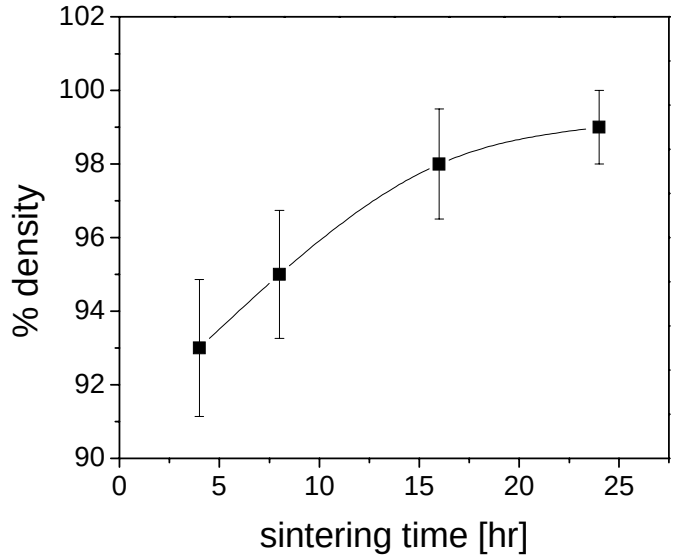

Figure 3.2. Density of $BaZr_{0.8}Y_{0.2}O_3$ as a function of sintering time, sintered at 1600°C under flowing O_2.

An SEM micrograph, Figure 3.3, of a fracture surface in the 24 hrs covered sample confirms the high density. The average grain size is approximately 0.46 μm, with a wide distribution of grain sizes (0.2–1μm). This small grain size is consistent with the observation that BYZ is highly refractory with low rates of grain growth under typical sintering conditions [14]. The step of covering the samples had little effect on density, but tended to yield materials with slightly larger grain sizes.

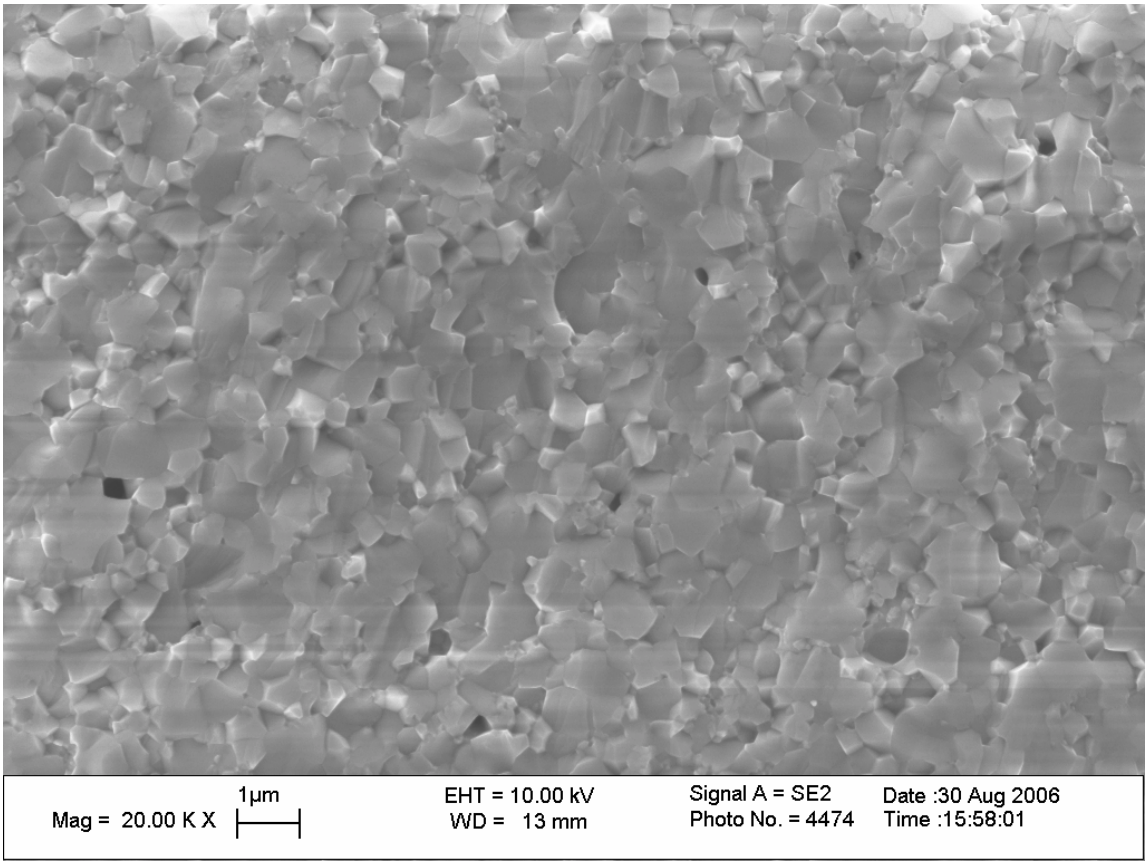

Figure 3.3. SEM micrograph of fracture surface of BYZ20 sintered for 24 hrs at 1600 °C.

A comparison of the x-ray diffraction patterns of covered and uncovered BYZ20 pellets is presented in Figure 3.4 (collected patterns from densified pellets were corrected for displacement errors). The data reveal quite clearly that even after just a few hours of exposure to 1600 °C, the uncovered pellets show a decrease in perovskite cell constant and display the presence of an impurity phase with a high intensity peak at 29.2 ° 2θ. This phase, also observed by Magrez and Schober in their study of the high temperature structural characteristics of $Ba_{0.99}Zr_{0.8}Y_{0.2}O_{3-\delta}$ [15], corresponds to a 'yttria-like' material [16] with space group Ia3- and lattice constant approximately 10.59 Å. It is to be emphasized that these precipitates occur throughout the bulk of the pellets; the highly disintegrated surface layer (50–100 µm) was removed by polishing prior to the collection of the diffraction data. It may be that such precipitates pin grain boundaries and are

responsible for the slightly smaller grain sizes in the uncovered sample.

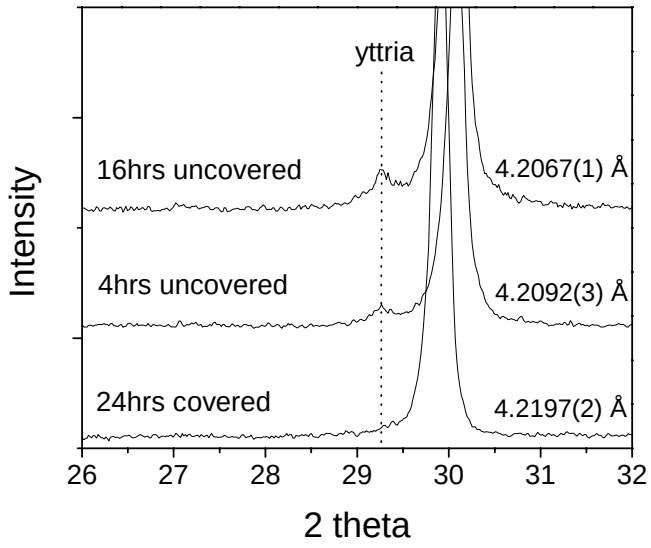

Figure 3.4. X-ray diffraction pattern of BYZ20 pellets sintered at 1600 °C under the conditions indicated. Number associated with each diffraction pattern is the perovskite unit cell parameter (see text for details).

The decrease in cell constant on prolonged exposure to high temperatures can be attributed to the precipitation of yttria from the perovskite structure due to barium loss. As the yttrium leaves the B-site, lattice constants decrease due to the smaller 6-fold coordinated zirconium ion. In contrast to the uncovered samples, even after 24 hrs of exposure to this same temperature BYZ20 covered with excess powder of the same composition is free of yttria precipitates.

The chemical analysis using the JEOL 8200 electron microprobe, Table 3.2, directly shows the uncovered samples to be barium deficient relative to those that were covered during sintering. In this analysis, BYZ20 covered (sintered for 24 hrs) was used as the standard against which the uncovered samples were compared.

Table 3.2. Summary of chemical analysis of sintered BYZ20 with access Ba (covered) and without access Ba (uncovered). Data normalized and reported as moles of cation per formula unit.

Sample	Ba, mole/f.u	Y, mole/f.u	Zr, mole/f.u	Ba/(Zr+Y)
S1	1.023944	0.175893	0.806109	
S2	1.001058	0.183145	0.812113	
S3	1.002477	0.192313	0.804527	
S4	1.012282	0.182078	0.807301	
S5	0.985867	0.208789	0.800475	
24hrs covered, average	**1.005±0.01**	**0.188±0.01**	**0.806±0.004**	**1.010**
S6	0.975289	0.195194	0.815961	
S7	0.981355	0.189261	0.817377	
S8	0.987645	0.187537	0.815525	
S9	0.964130	0.191762	0.824114	
S10	0.983761	0.187945	0.817161	
4hrs uncovered, average	**0.978±0.008**	**0.190±0.003**	**0.818±0.003**	**0.970**
S11	0.974144	0.195688	0.816163	
S12	0.96377	0.184314	0.829879	
S13	0.959533	0.198868	0.821083	
S14	0.96602	0.191051	0.823702	
S15	0.965264	0.186103	0.827791	
16hrs uncovered, average	**0.966±0.005**	**0.191±0.006**	**0.824±0.005**	**0.952**

The molar ratio Ba/(Zr+Y) falls from 0.97 for the uncovered sample sintered for four hours to 0.95 for the sample sintered for 16 hrs, in agreement with the observation of an increasing intensity for the yttria diffraction peak with increasing sintering time for uncovered samples. We

note that even the covered samples showed measurable barium deficiency (which can be explicitly seen in Table 3.3), however, we focus here on the relative chemical differences between the covered and uncovered samples rather than their absolute chemistries.

Although Ba evaporation during sintering can be successfully suppressed with excess powder, as described above, Ba deficiencies can also arise from zirconium contamination during long periods of high energy milling with stabilized zirconia media. Chemical analysis of milled and sintered sample vs. an only sintered (no milling) sample shows a molar ratio Ba/(Zr+Y) difference of 0.02, Table 3.3. In this analysis, zircon, yttrium phosphate, and barium titanate were used as standards. The data presented is not normalized as above, Table 3.2, and shows the actual moles of cation per formula unit (f.u).

Table 3.3. Summary of chemical analysis of sintered BYZ20 with attritor milling and without milling. Data reported as moles of cation per formula unit.

Sample	Ba, mole/f.u	Y, mole/f.u	Zr, mole/f.u	Ba/(Zr+Y)
S1	0.948905	0.217961	0.812076	
S2	0.985596	0.160692	0.836684	
S3	0.986428	0.163901	0.83386	
S4	0.979712	0.163441	0.837563	
S5	0.96829	0.174204	0.835202	
Attritor milled, average	**0.974±0.014**	**0.176±0.022**	**0.83±0.01**	**0.967**
S6	0.990679	0.209188	0.797769	
S7	0.985198	0.213079	0.797591	
S8	0.999333	0.210577	0.792401	
S9	1.000733	0.205865	0.795235	
S10	0.986549	0.208502	0.800349	
No milling, average	**0.993±0.006**	**0.209±0.002**	**0.797±0.003**	**0.987**

In addition to the observation of increasing intensity for the yttria diffraction peak, as well as decreasing lattice constant for BYZ as a consequence of Ba loss, surface imaging of barium deficient samples also show yttrium rich regions. Figure 3.5 is the surface image of a 34 mol % Ba deficient sample as determined by the electron microprobe. Results of the EDS chemical analysis are shown in the image, and clearly seen are darker regions with excess yttrium, while lighter regions have a molar ratio of Ba/Zr close to unity. It is noteworthy that Ba deficient sample prefer to lose Y from the B-site rather than Zr, Eq. (3.1).

$$Ba(Y_{0.20}Zr_{0.80})O_{3-\delta} \rightarrow Ba_{1-x}(Y_{0.20-x}Zr_{0.80})O_{3-\delta} + \frac{x}{2}Y_2O_3 + x\,BaO\uparrow \qquad (3.1)$$

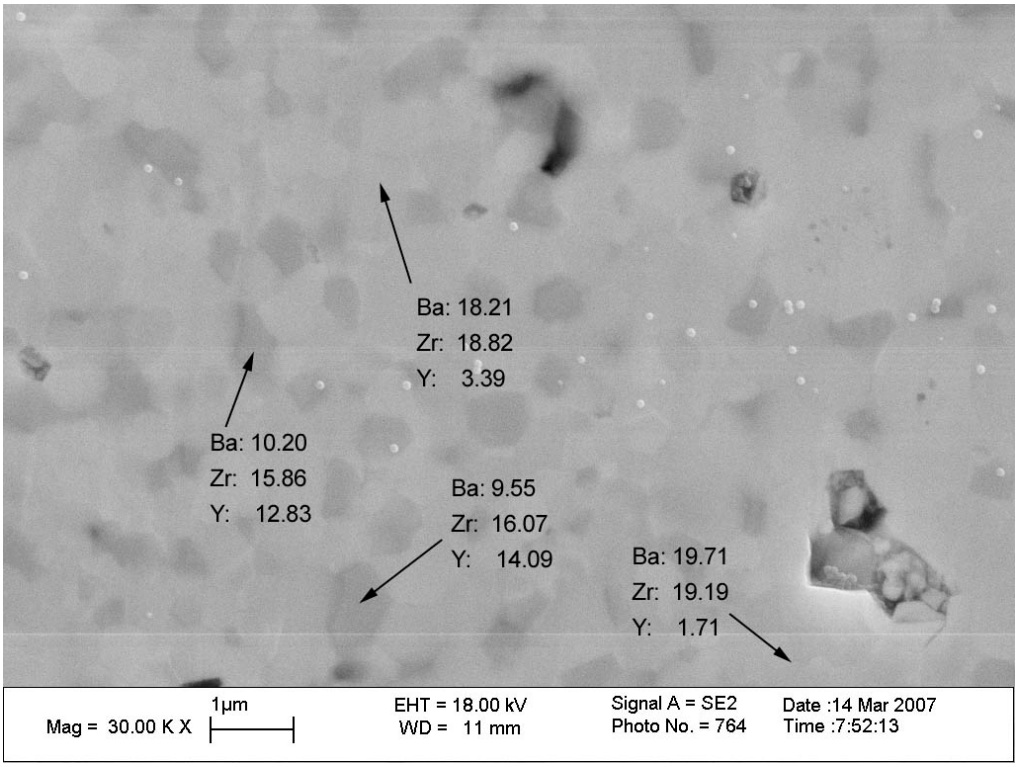

Figure 3.5. SEM surface image of 34 mol% Ba deficient sample with yttrium rich darker regions.

Overall, the results provide clear evidence that under typical sintering conditions, $BaZr_{1-x}Y_xO_{3-\delta}$ samples decompose to form yttria and volatile barium oxide. The absence of yttria

precipitates from covered samples indicates that the volatilization of barium oxide can be kinetically suppressed. A related synthesis procedure has been proposed by Snijkers et al. [9], who showed that direct addition of excess barium carbonate within the bulk of pressed pellets has a similar effect of suppressing yttria precipitation during the sintering of uncovered samples.

3.4 Conductivity of BYZ by impedance spectroscopy

Representative A.C. impedance spectra of BYZ20 (with sample dimensions of 0.65 to 0.73 mm in thickness and 0.69 to 0.71 cm^2 in area) obtained under wet N_2 (0.03 atm H_2O) are shown in the Nyquist representation (-Zimag vs. Zreal) in Figure 3.6. Only at the lowest temperatures (<150 °C) do the spectra display clear evidence a high frequency arc (Arc 1) that extends to the origin. This arc, which yields a relative dielectric constant of 46, is attributed to the bulk behavior of BYZ20. As the temperature is increased, because the characteristic frequency, ω_o, of the bulk processes increases exponentially ($\omega_o = 1/RC$, where R is resistance and C is capacitance), the bulk arc becomes no longer accessible and even at just 125 °C the spectra are dominated by a lower frequency process (a very typical result). This midfrequency arc (Arc 2) is attributed to grain boundary processes. The 'equivalent' relative dielectric constant (that is, one in which the grain boundary dimensions are not accounted for) implied by this arc is on the order of 6500. This value is consistent with grain boundary properties, as discussed further below. At the very lowest frequencies, evidence for an even slower process appears in the 125 °C spectrum (Arc 3), which is attributed to the electrode.

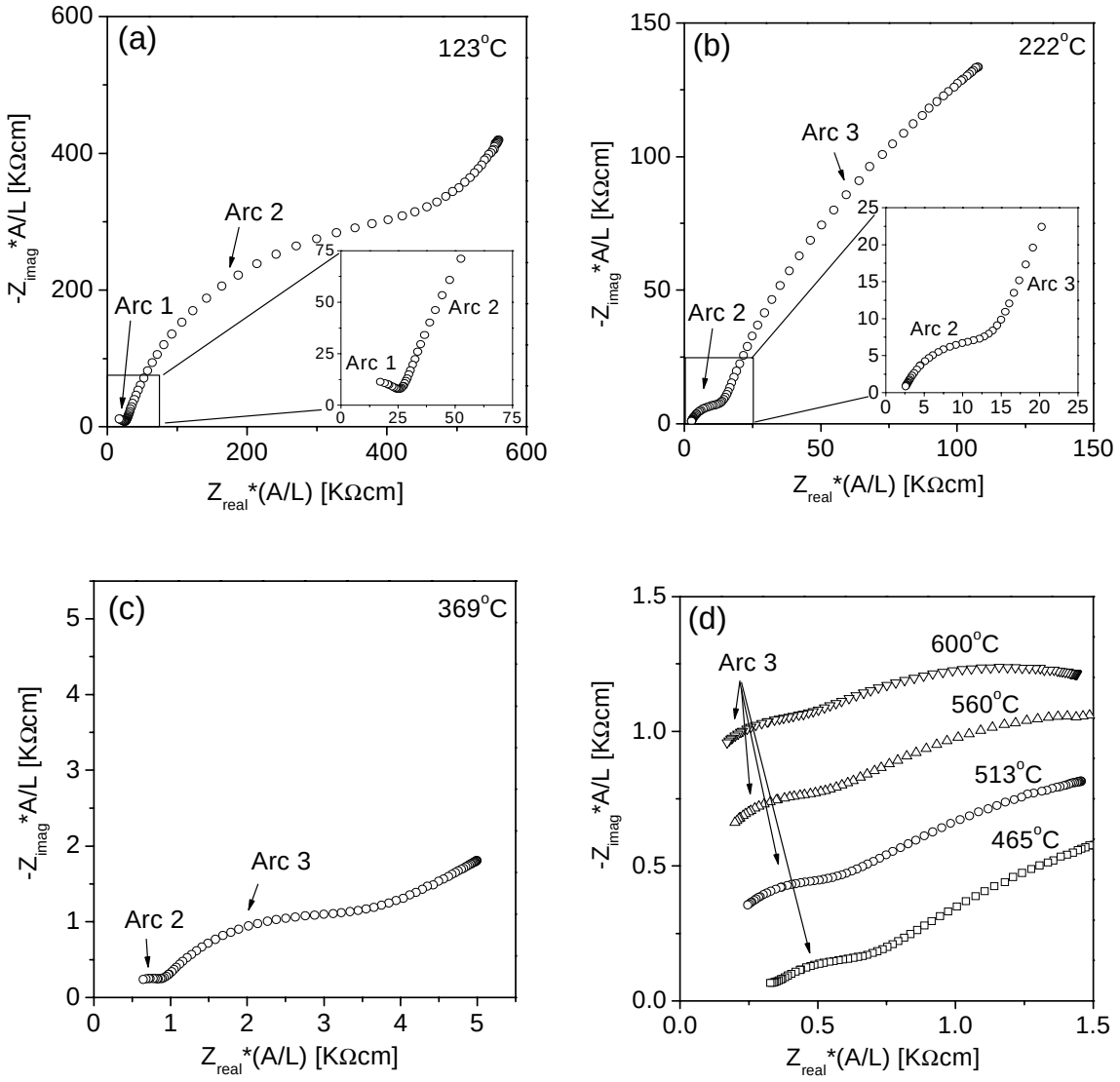

Figure 3.6. Nyquist impedance spectra obtained from BYZ20 with Ag electrodes under humidified nitrogen (pH_2O = 0.03 atm) at the noted temperature (a) 123 °C, (b) 222 °C, (c) 269 °C, and (d) 465–600 °C. In (d) data are offset along the imaginary axis in increments of 0.3 KΩcm for clarity.

As the temperature is further increased, the electrode processes begin to dominate the overall response. By 370 °C, it is almost impossible to distinguish between bulk and grain boundary contributions to the electrolyte resistance, and furthermore the electrode processes display evidence of a complex electrochemical reaction pathway, characterized by two or

possibly more characteristic time scales. At temperatures greater than about 450 °C, no direct information can be obtained regarding the electrolyte properties. The spectra reflect entirely the electrode processes and only the displacement of the spectra from the real axis provides any measure of the electrolyte resistance. In the absence of lower temperature data, misinterpretation of the type of spectra shown in Figure 3.6 d could easily occur. For example, the lower frequency feature of the electrode response could incorrectly be attributed to the grain boundary response, and the electrolyte resistance overestimated by a factor of up to three at high temperatures.

Selected results of the examination of Pt as an alternative electrode material are shown in Figure 3.7. Here, comparison is made between impedance spectra collected using Ag, those collected using Pt (fritless Pt paste, Heraeous, fired at 1100 °C) and those collected using fritless Pt and an additional Ag layer. Although the spectra were comparable at lower temperatures (data not shown), they are not at the high temperatures at which the electrode processes dominate the impedance response. The Pt based electrodes give rise to additional electrode resistance effects which, again, can be easily misinterpreted as originating from the electrolyte. The undesirable electrode properties of Pt may also play a role in the large discrepancies in the reported conductivity values for barium zirconate, Table 3.1.

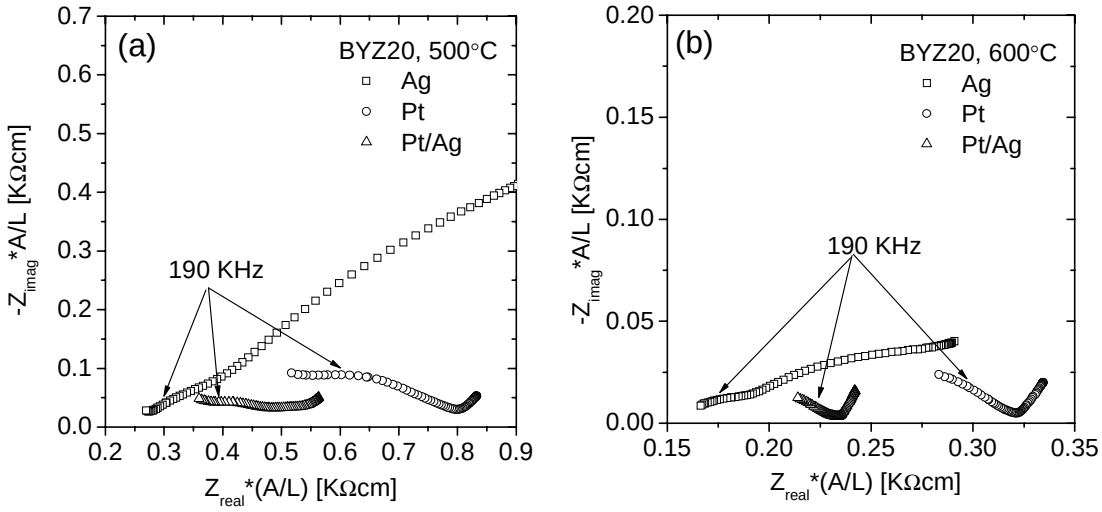

Figure 3.7. Nyquist impedance spectra obtained from BYZ20 under humidified nitrogen (pH_2O = 0.03 atm) using the electrodes the electrodes indicated at (a) 500 °C and (b) 600 °C.

From the complete fitting of the impedance data (Figure 3.6), it was possible (depending on the temperature of the measurement) to obtain the resistance, constant phase element parameters, and capacitance, given by $C = Y^{\frac{1}{n}} R^{(\frac{1}{n}-1)}$, where R, Y and n are as described in Chapter 1, for both the bulk and grain boundary regions of the material. If one assumes that the true dielectric constant of the grain boundaries and the bulk (grain interior) are comparable, then the ratio of the apparent capacitances, Cgb/Cgi, is simply equal to the ratio of the grain diameter, D, to the grain boundary thickness, δ (Chapter 1). The temperature averaged value of this ratio was found to be ~ 140, and if one takes the grain boundary thickness to be on the order of 2.5 nm (as has been observed in Gd-doped barium cerate [20]), the implied grain size is on the order of 0.35 μm. This value agrees well with the observed 0.46 μm average grain size in the SEM image and confirms the assignment of the mid-frequency arc in the impedance spectra to grain boundary processes.

The respective conductivities were deduced from the resistance terms obtained from the

impedance data by accounting for the sample geometry according to Eq. (3.2):

$$\sigma = \frac{1}{R} * \frac{L}{A}, \tag{3.2}$$

where L is the sample thickness and A is its cross-sectional area. As introduced in Chapter 1, the specific grain boundary conductivity (independent of microstructure), $\sigma_{sp.gb}$, was determined, again, under the assumption that the true dielectric constants of the bulk and grain boundary regions are equal, using:

$$\sigma_{sp.gb} = \frac{L}{A}\left(\frac{C_{gi}}{C_{gb}}\right)\frac{1}{R_{gb}}, \tag{3.3}$$

with the temperature-averaged (single) value of the ratio C_{gi}/C_{gb}.

The conductivity of BYZ20 derived from the impedance measurements is shown in Figure 3.8. Here, the bulk conductivity, the specific grain boundary conductivity, and the total conductivity (the only quantity which could be measured at high temperatures as evidenced by the form of the impedance spectra in Figure 3.6 d) are all presented. In the figure 'c' indicates the sample was covered with excess barium during the sintering step and 'u' that it was not covered. The bulk conductivity obtained for $BaZr_{0.8}Y_{0.2}O_{3-\delta}$ in this study is comparable to that reported by Bohn and Schober for $BaZr_{0.9}Y_{0.1}O_{3-\delta}$ [4], as is the value of the activation energy, supporting our assignment of the high frequency arc (arc 1) in Figure 3.6 a to bulk processes. Specifically, Bohn and Schober reported an activation energy for bulk conduction under wet argon of E(Bulk) = 0.44 ± 0.01 eV, as compared to the present values of 0.45 ± 0.01. The present results also confirm that the bulk conductivity of BYZ20 is, in fact, higher, at temperatures lower than 350 °C, than that of typical doped barium cerates, with a correspondingly lower activation energy for proton migration.

As revealed by comparison of Figure 3.8 a and 3.8 b, the specific grain boundary conductivity of BYZ20 is much lower than that of the bulk. Simultaneously, the activation energy

for proton transport across grain boundaries, 0.71 ± 0.02 eV, is higher. The grain boundary behavior of BYZ20 is again similar to that reported by Bohn and Schober for BYZ10, who observed an activation energy of ~0.7 eV for proton conduction through the grain boundary regions of their material. This similarity again supports the identification of the mid-frequency arc with grain boundary transport. High grain boundary resistance to ion transport is typical of ionic conductors [21], and has also been reported for the related material barium cerate [20]. Given that the bulk conductivity of barium zirconate is higher than that of barium cerate, it is somewhat surprising that specific grain boundary resistivity of the zirconate is higher than that of the cerate. Particularly significant for barium zirconate is that the highly refractory properties lead to very small grains and consequently a much higher grain boundary density. As a result, the total conductivity of barium zirconate, that which is the relevant quantity for applications, is much lower than what would be expected simply on the basis of the bulk transport properties, Figure 3.8 c, especially at temperatures of 500 °C and lower.

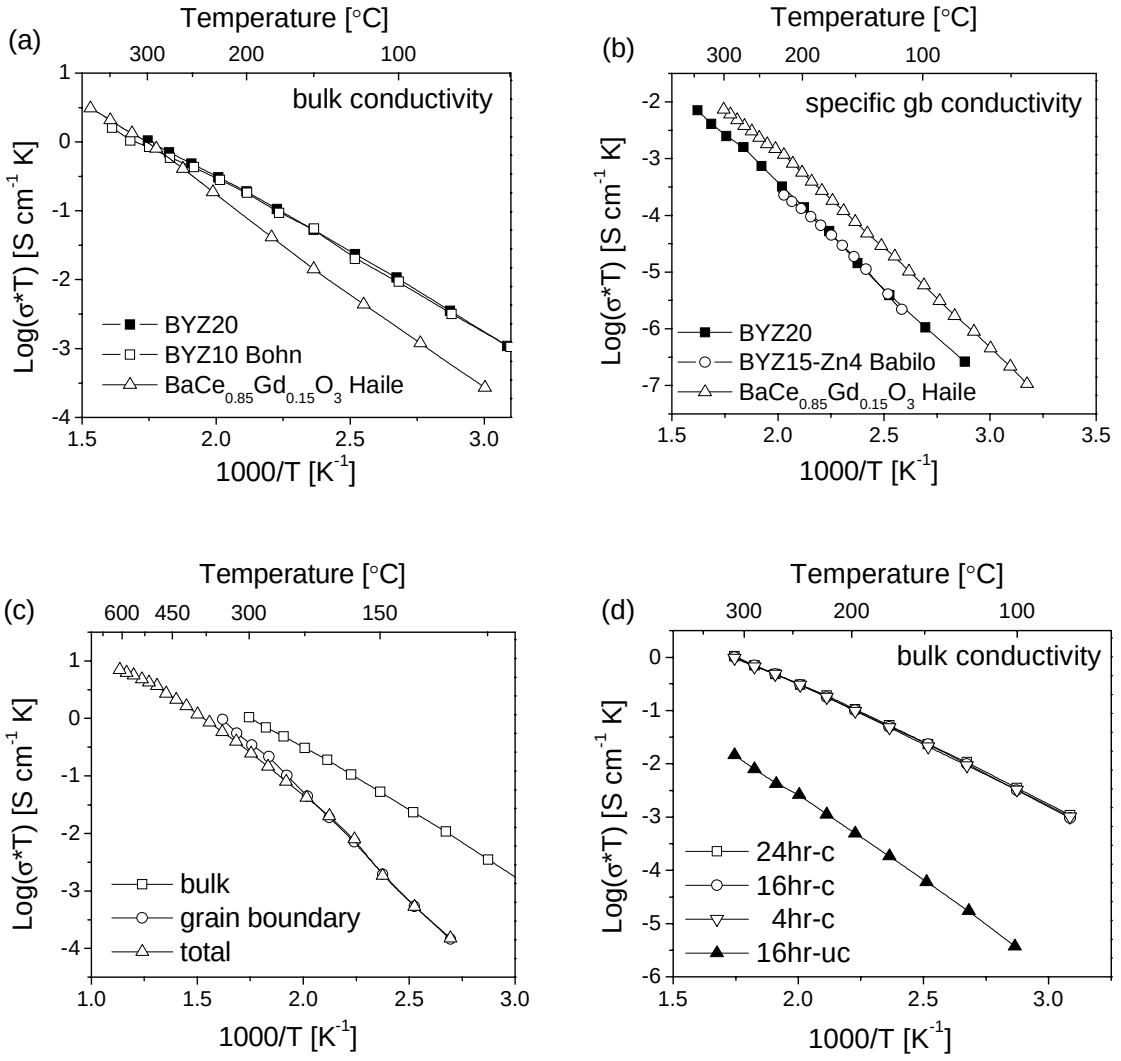

Figure 3.8. Conductivity of BYZ20 under humidified nitrogen (pH2O = 0.03 atm), Ag electrodes: (a) bulk (grain interior) conductivity compared to that of $BaZr_{0.9}Y_{0.1}O_3$ (BYZ10) [4] and $BaCe_{0.85}Gd_{0.15}O_3$ [20]; (b) specific grain boundary conductivity (normalized for grain size differences) as compared to that of $BaZr_{0.85}Y_{0.15}O_3$-$(ZnO)_{0.04}$ (BYZ14-Zn4) [14] and $BaCe_{0.85}Gd_{0.15}O_3$ [20]; (c) comparison between grain interior, grain boundary, and total conductivity of BYZ20; and (d) bulk (grain interior) conductivity of BYZ20 sintered for the time periods indicated.

The comparison of the properties of BYZ20 that was covered during sintering with that of BYZ20 that was not covered, Figure 3.8 d, shows quite dramatically the impact of slight losses

of barium from the sample during high temperature processing. The conductivity of the uncovered pellet has a grain interior conductivity at 100 °C that is almost three orders of magnitude lower than that of the covered pellets. In contrast, three different pellets sintered for differing time periods (4, 16 and 24 hrs) exhibit highly reproducible bulk conductivity, despite even slight differences in density (Figure 3.2). A discussion of the grain boundary properties of these samples is presented elsewhere [22].

The detrimental impact of barium deficiency on the conductivity of doped barium cerate has been well documented [17, 18] and explained in terms of the occupation of the trivalent dopant on the A rather than B site. These effects, which occur in single-phase materials, are responsible for variations in bulk conductivity by a factor of two to three [17]. Here it is apparent that the extent of barium oxide sublimation is far more substantial, inducing yttria precipitation within the bulk of the material and causing a reduction in conductivity that is two orders of magnitude greater than that observed in the cerate. Furthermore, even in barium cerate samples in which barium deficiency is comparable to that observed here for barium zirconate (i.e., similarly induces phase precipitation in the bulk) the decrease in conductivity remains only about a factor of three [17, 20], indicating that not only is barium zirconate more susceptible to barium loss because of the required high-temperature processing, the impact is also more significant. Reasons for such a dramatic influence of barium loss on conductivity may be (1) the precipitation of yttria from the perovskite structure, producing the non-conductive $BaZrO_3$ and (2) the accumulation of the yttria impurities in the grain boundary regions. It is clear that processing differences must contribute substantially to the significant discrepancy in the reported properties of barium zirconate, Table 3.1. In the present study it was generally observed that the precise placement of uncovered samples relative to one another strongly affected the conductivity, and, while the results presented in Figure 3.8 d for an uncovered sample are representative, by definition, properties under ill-defined conditions are indeterminate.

At high temperatures, because of the higher activation energy of grain boundary

conductivity over conductivity through the bulk, the total conductivity of BYZ20, that which is relevant for applications, becomes dominated by the bulk transport properties. Thus, despite the high resistivity of the grain boundaries, the total conductivity at 600 °C was found to be 7.9×10^{-3} S/cm. Such a value compares favorably to the conductivity of YSZ at this same temperature, 3.2×10^{-3} S/cm [23]. Furthermore, referring to Table 3.1, it is comparable to the highest reported value for doped barium zirconate and reflects the high conductivity that results when due care is directed towards minimizing barium deficiency in the final material.

3.5 Conclusions

The findings of this study are summarized as follows

1. High density, high conductivity yttrium doped barium zirconate can be reproducibly obtained under the processing conditions described. Specifically, the particle size of the starting powder must be less than 100 nm, the green body must be prepared using a binder so as to achieve high green density, and the sintering must be carried out under excess barium so as to avoid barium loss. Sintering under oxygen also appears important, but this point requires further investigation.

2. The total conductivity of $BaZr_{0.8}Y_{0.2}O_{3-\delta}$ at 600 °C under humidified nitrogen with pH_2O = 0.031 atm is 7.9×10^{-3} S/cm, where, total refers to resistance contributions of both the bulk (grain interior) and grain boundary regions of the material.

3. In the absence of excess barium, the high temperature sintering conditions required to achieve good densification of barium zirconate induce measurable changes in stoichiometry and dramatic reductions in proton conductivity. Specifically, barium deficiency was shown to lower the conductivity by two orders of magnitude and it is believed that stoichiometry differences induced by severe processing conditions are the major contributor to the wide variation in literature data for the conductivity of yttrium doped barium zirconate.

3.6 References

1. H. Iwahara, T. Yajima, T. Hibino, K. Ozaki, and H. Suzuki. Protonic conduction in calcium, strontium and barium zirconates. *Solid State Ionics* **61**, 65 (1993).

2. A. Manthiram, J. F. Kuo, and J. B. Goodenough. Characterization of oxygen-deficient perovskites as oxide-ion electrolytes. *Solid State Ionics* **62**, 225 (1993).

3. R. C. T. Slade, S. D. Flint, and N. Singh. Investigation of protonic conduction in Yb- and Y-doped barium zirconates. *Solid State Ionics* **82**, 135 (1995).

4. H.G. Bohn and T. Schober. Electrical conductivity of the high-temperature proton conductor $BaZr_{0.9}Y_{0.1}O_{2.95}$. *J. Am. Ceram. Soc.* **83**, 768 (2000).

5. K. Katahira, Y. Kohchi, T. Shimura, and H. Iwahara. Protonic conduction in Zr-substituted $BaCeO_3$. *Solid State Ionics* **138**, 91 (2000).

6. V. P. Gorelov, V. B. Balakireva, Y. N. Kleshchev, and V. P. Brusentsov. Preparation and electrical conductivity of $BaZr_{1-x}R_xO_3$ (R = Sc, Y, Ho, Dy, Gd, In). *Inorganic Materials* **37**, 535 (2001).

7. M. Laidoudi, I. Abu Talib, and R. Omar. Investigation of the bulk conductivity of $BaZr_{0.95}M_{0.05}O_3$ (M=Al, Er, Ho, Tm, Yb and Y) under wet N_2. *J. Phys. D: Appl. Phys.* **35**, 397 (2002).

8. K. D. Kreuer. Proton-conducting oxides. *Annu. Rev. Mater. Res.* **33**, 333 (2003).

9. F. M. M. Snijkers, A. Buekenhoudt, J. Cooymans, and J. J. Luyten. Proton conductivity and phase composition in $BaZr_{0.9}Y_{0.1}O_{3-delta}$. *Scripta Mater.* **50**, 655 (2004).

10. W. S. Wang and A. V. Virkar. Ionic and electron-hole conduction in $BaZr_{0.93}Y_{0.07}O_3$ by 4-Probe D.C. measurements. *J. Power Sources* **142**, 1 (2005).

11. C. D. Savaniu , J. Canales-Vazquez, and J. T. S. Irvine. Investigation of proton conducting $BaZr_{0.9}Y_{0.1}O_{2.95}$: $BaCe_{0.9}Y_{0.1}O2.95$ core-shell structures. *J. Mater. Chem.* **15**, 598 (2005).

12. F. Iguchi, T. Yamada, N. Sata, T. Tsurui, and H. Yugami. The influence of grain structures on the electrical conductivity of a $BaZr_{0.95}Y_{0.05}O_3$ proton conductor. *Solid State Ionics* (press 2006).

13. K. D. Kreuer. Aspects of the formation and mobility of protonic charge carriers and the stability of perovskite-type oxides. *Solid State Ionics* **125**, 285 (1999).

14. P. Babilo and S. M. Haile. Enhanced sintering of yttrium-doped barium zirconate by addition of ZnO. *J. Am. Ceram. Soc.* **88**, 2362 (2005).

15. A. Magrez and T. Schober. Preparation, sintering, and water incorporation of proton conducting $Ba_{0.99}Zr_{0.8}Y_{0.2}O_3$: Comparison between three different synthesis techniques. *Solid State Ionics* **175**, 585 (2004).

16. G. Baldinozzi, J. F. Berar, and G. Calvarin. Rietveld refinement of two-phase Zr-doped Y_2O_3. *Mater. Sci. Forum* **278-2**, 680 (1998).

17. D. Shima and S. M. Haile. The influence of cation non-stoichiometry on the properties of undoped and Gadolinia-doped barium cerate," *Solid State Ionics* **97**, 443 (1997).

18. J. Wu, L. P. Li, W. T. P. Espinosa, and S. M. Haile. Defect chemistry and transport properties of $Ba_xCe_{0.85}M_{0.15}O_3$. *J. Mater. Res.* **19**, 2366 (2004).

19. J. Wu, S. M. Webb, S. Brennan, and S. M. Haile. Dopant site selectivity in $BaCe_{0.85}M_{0.15}O_3$ by extended x-ray absorption fine structure. *J. Appl. Phys.* **97**, 054101 (2005).

20. S. M. Haile, D. L. West, and J. Campbell. The role of microstructure and processing on the proton conducting properties of Gadolinium-doped barium cerate. *J. Mater. Res.* **13**, 1576 (1998).

21. X. Guo and R. Waser. Space charge concept for acceptor-doped zirconia and ceria and experimental evidences. *Solid State Ionics* **173**, 63 (2004).

22. P. Babilo. Processing and Characterization of Proton Conducting Yttrium Doped Barium Zirconate for Solid Oxide Fuel Cell Applications. P. Babilo Thesis Chapter 4 (2007).

23. B. C. H. Steele. Oxygen ion conductors and their technological applications. *Mater. Sci. Eng.* **13**, 79 (1992).

Chapter 4: Microstructure and conductivity of the $BaZr_{1-x}Y_xO_{3-\delta}$ system, where x = 0.2, 0.3, 0.4

4.1 Introduction

The inability to obtain high quality data due to processing and nonstoichiometry challenges for the barium zirconate system has not allowed for the material to be fully optimized in terms of microstructure, composition, or defect structure. Chapter 3 established the methodology to produce such high conductivity samples and that approach will be utilized to further characterize BYZ material properties.

Recent researchers have attempted to optimize the grain structure by elongated sintering periods. Iguchi et al. reported average grain size of 1.61 μm after 200 hrs of sintering at 1800 ºC [1]. Although larger grains were obtained, considerably decreasing the grain boundary density, conductivities of the samples were 2–3 orders of magnitude lower than samples prepared with shorter sintering times. Even though the authors state that chemical compositions were not affected by sintering conditions, in such extreme processing conditions, the loss of Ba from the perovskite structure is inevitable.

An alternative approach to improving the performance of doped barium zirconate system is to significantly increase the proton concentration by the introduction of additional dopant. This methodology has raised conflicting opinions on its effectiveness. Neutron diffraction studies by Hempelmann [2] revealed the introduction of dopant ions caused negatively charged defects that act as proton traps. Scherban and Nowick [3] illustrate, by analysis of preexponential terms in the conductivity of Yb doped $SrCeO_3$, that only a fraction of all protons dissolved are mobile carriers. In addition, Davies and Islam [4] completed a series of calculations to derive binding energies of defect clusters. Their simulations indicated proton-dopant associations may occur. In stark contrast, Kreuer [5] suggests that the observed increase in activation energy for the protonic

defect with increased dopant concentration may be related to the general increase in oxygen basicity and the barrier for proton transfer rather than proton-dopant association.

In this chapter we examine the electrical properties of samples prepared with varying grain sizes to clarify the role of grain boundary contributions to the total conductivity. Further, we explore dopant concentration influence on stability, proton concentration, and mobility.

4.2 Influence of Grain Size on the Electrical Conductivity

4.2.1 Microstructural Evaluation

Synthesized BYZ (glycine-nitrate process) powders were used to prepare densified pellets for conductivity measurements. Prior to sintering, powers were attritor milled at 500 rpm for 5 hrs and combined with a binder solution. Green pellets were obtained by uniaxial pressing and sintering with excess BYZ powders, to avoid Ba loss. Sintering was carried out under flowing oxygen at 1600 °C for a period of 4 to 24 hrs. A more detailed explanation of the preparation procedure is described in Chapter 2.

Grain size analysis of sintered samples surfaces and bulk was conducted using the ASTM E112 standard [6] on electron microscopy images. Analysis of the unpolished surface, Figure 4.1, can be misleading in determining sample grain size. It was often observed that the surface grain size is considerably larger than that of the bulk, Table 4.1. Slight Ba evaporation during the sintering process may be responsible for the increase in grain boundary mobility resulting in surface grain growth.

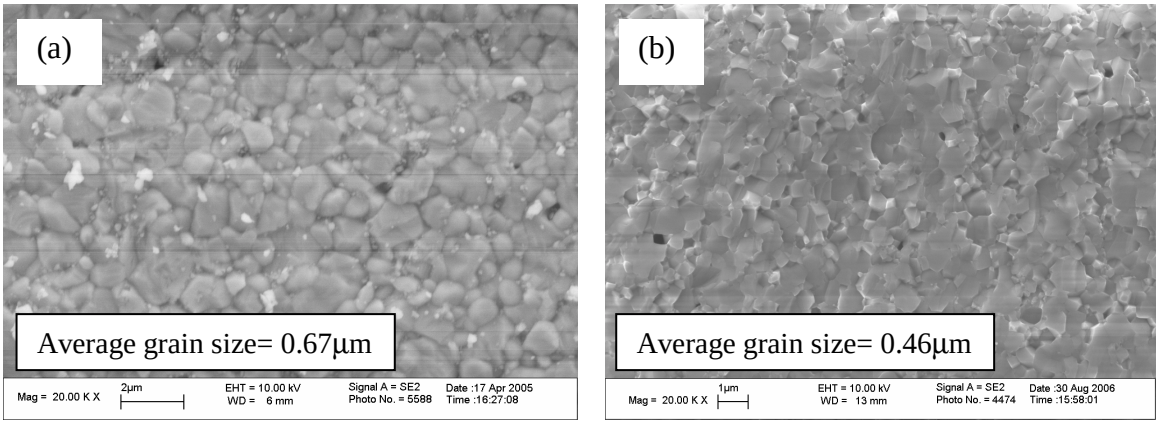

Figure 4.1. SEM image of BYZ20 sintered 1600 ºC for 24hrs (a) unpolished surface and (b) fracture surface.

Table 4.1. Comparison of surface and bulk average grain size for varying sintering conditions.

Sintering Time [hrs]	Surface grain size [μm]	Bulk grain size [μm]
4	0.49	0.34
16	0.66	0.43
24	0.67	0.46

4.2.2 Electrical Characterization

Impedance nyquist plots for the BYZ system at 75 ºC are shown in Figure 4.2. With increasing sintering time (larger grains) is it clear that there exists less overlap between the grain interior (first arc) and grain boundary (second arc) arcs. Least square fitting of impedance plots with the resistance-CPE (R-CPE) elements in series, shown in Figure 4.3, allows the determination of the resistance and constant phase element (CPE) associated with both the grain interior (bulk) and grain boundary responses. Further the capacitance can be obtained by $C = Y^{\frac{1}{n}} R^{(\frac{1}{n}-1)}$, where R is the resistance, Y and n are fitting parameters of the CPE as introduced in Chapter 1. Fitting with the (R)(CPE)-(R)(CPE) equivalent circuit was possible in the

temperature range of 50–150 ºC. For temperatures greater than 150 ºC the high frequency arc (grain interior) can no longer be fitted with confidence.

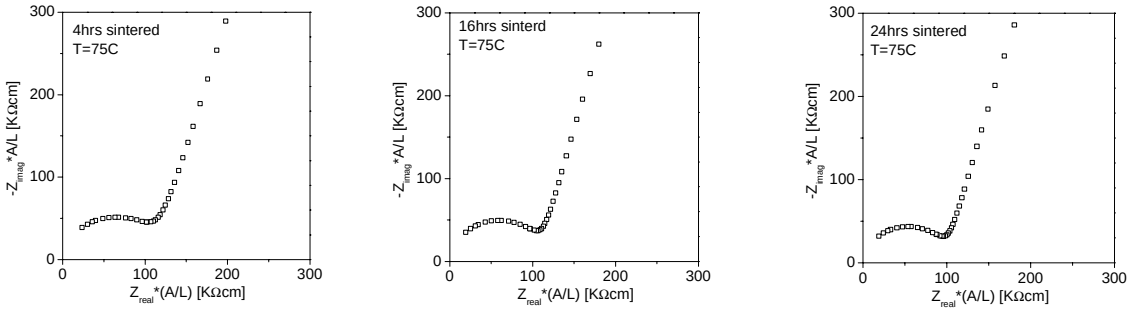

Figure 4.2. Nyquist plots for samples sintered at 4, 16, and 24 hrs at 1600 ºC. Measurements made with Ag electrodes in water saturated nitrogen.

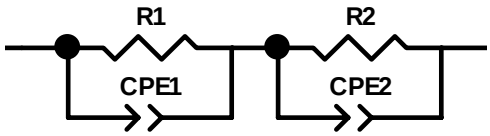

Figure 4.3. Equivalent circuit used up to 150 ºC to determine grain interior and grain boundary resistance and capacitance.

With a fixed characteristic frequency (only dependent on material properties), $w_0=1/(RC)$, for the grain boundary response, an increase in the total resistance results in a decrease of the capacitance. As the capacitance value of the grain boundary approaches that of the grain interior response (10^{-12} F), greater overlap of the two arcs is expected. The overlapping capacitance values results in a convolution of the impedance arcs producing higher fitting errors.

The true dielectric constants for the bulk and the effective dielectric constant for the grain boundary, in turn, can be calculated from the capacitance according to Eq. (4.1) and are shown in Figure 4.4 (grain interior) and Figure 4.5 (grain boundary).

$$\varepsilon = \frac{C}{\varepsilon_0}\frac{L}{A} \tag{4.1}$$

The figure reveals doped barium zirconate has a bulk dielectric constant in the range of 42–49. The dielectric constant, as visually observed in the case of 4, 16, and 24 hrs sintering times, is independent of temperature. The higher error bars in the 4 hrs sintered sample are a result of the higher grain boundary density. As discussed above, the higher resistive grain boundaries (smaller grain) cause slight overlapping of the impedance arcs resulting in fitting errors.

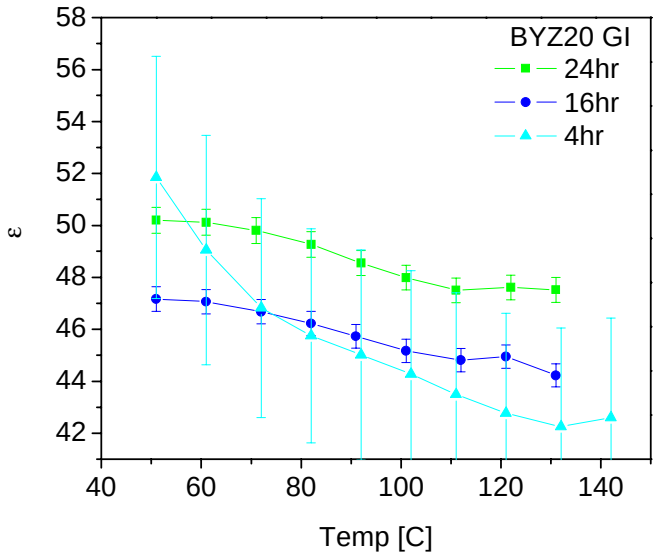

Figure 4.4. Dielectric constant of the BYZ20 bulk (Ag electrodes in wet nitrogen, P_{H20}=0.03 atm).

At first glance the dielectric constant of the grain boundary seems to be 2 orders of magnitude larger than the grain interior. Values shown are only the effective constants, not having accounted for the geometric properties of the grains. The grain boundary capacitances are weakly dependent on temperature, but significantly dependent on grain size. This observation was also noted for Fe doped $SrTiO_3$ [7].

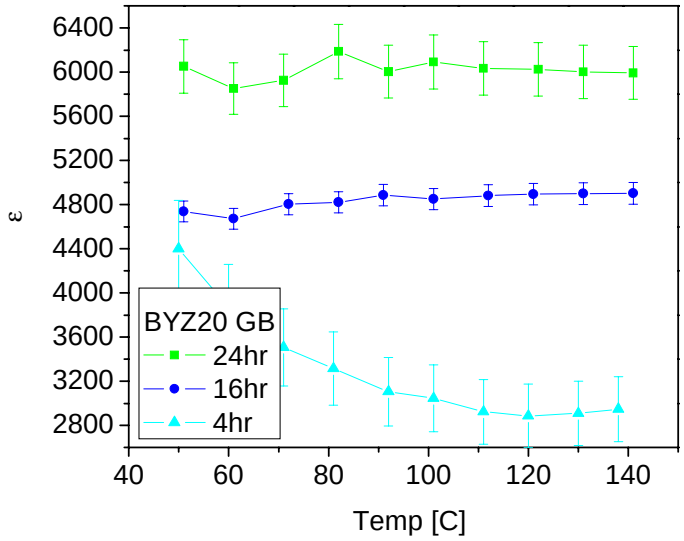

Figure 4.5. Effective dielectric constant of the grain boundary in BYZ20 (Ag electrodes in wet nitrogen, P_{H20}=0.03 atm).

In the narrow temperature range that both the grain interior and grain boundary arcs can be obtained and reliably measured (50–150 ºC), a ratio of the capacitances is calculated. With the assumption that the dielectric constant of the grain interior and grain boundary are comparable, $(\varepsilon_{gi} \approx \varepsilon_{gb})$, the ratio of the apparent capacitances, C_{gi}/C_{gb}, is simply equal to the ratio of the grain boundary thickness, δ, to the grain diameter, D, providing insight into the microstructure characteristics, Eq. (4.2).

$$\frac{C_{gi}}{C_{gb}} = \frac{\frac{A}{L}\varepsilon_{gi}\varepsilon_0}{\frac{A}{L}\frac{D}{\delta}\varepsilon_{gb}\varepsilon_0} = \frac{\delta}{D} \tag{4.2}$$

In Eq. (4.2), δ signifies grain boundary thickness, while D is the average grain size. Grain boundary thickness is slightly higher than the 2.7 nm reported for gadolinium doped barium

circuit by Haile et al [8]. A trend of decreasing thickness with increasing sintering time is also observed, Table 4.2.

Table 4.2. Calculated grain boundary thickness based on fitted capacitance and grain size from microscopy.

Sintering Time [hrs]	Capacitance ratio	Grain size [μm]	Grain boundary thickness [nm]
4	0.0130	0.34	4.4
16	0.0092	0.43	4.0
24	0.0080	0.46	3.7

Grain interior (bulk) conductivity data is remarkably reproducible, Figure 4.6, given differences in processing conditions. As discussed previously in Chapter 3, the bulk conductivity obtained for $BaZr_{0.8}Y_{0.2}O_{3-\delta}$ is comparable to that reported by Bohn and Schober for $BaZr_{0.9}Y_{0.1}O_{3-\delta}$ [9] and is higher than that of typical doped barium cerates, especially at lower temperatures.

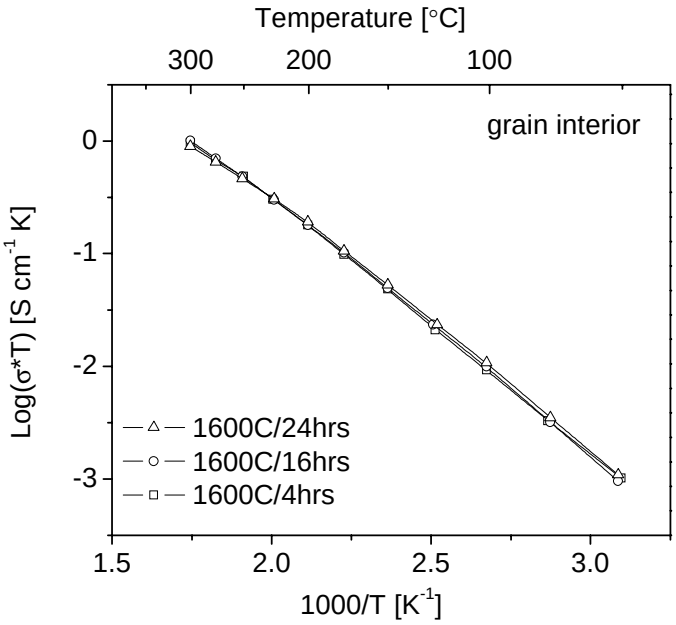

Figure 4.6. Grain interior conductivities of BYZ20 sintered for 4, 16, and 24 hrs (saturated nitrogen, P_{H20}=0.03 atm, Ag electrodes).

As revealed by comparison of samples in Figure 4.7, the grain boundary conductivity is influenced by the grain size as predicted. Sample sintered for 4 hrs, with average grain size of 0.34 μm, shows 2–3 times lower conductivity in the total grain boundary, Figure 4.7 a, than samples sintered for 24 hrs, with average grain size of 0.46 μm. However, when conductivities are corrected for grain geometry, Figure 4.7 b, the specific grain boundary conductivities are similar. A slight increasing trend is evident with increasing grain size, which correlates to the decrease in grain thickness and decrease in the space charge of the grain boundary, as discussed below. Activation enthalpies and preexponential factors fitted with the Arrhenius form, Eq. (4.3), are summarized in Table 4.3.

$$\sigma T = Ae^{-\frac{E}{k_B T}} \tag{4.3}$$

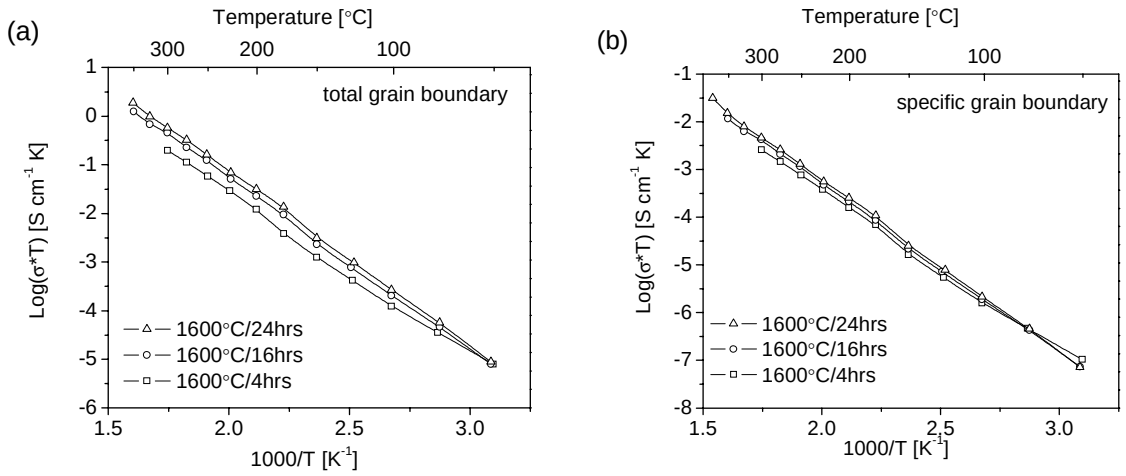

Figure 4.7. BYZ20 (a) total grain boundary conductivities and (b) specific grain boundary conductivities (saturated nitrogen, P_{H20}=0.03 atm, Ag electrodes).

The influence of grain size on the grain boundary conductivity is more dramatically observed in the impedance spectrums. The nyquist plots obtained for a single temperature (100 ºC) are shown in Figure 4.8. At this temperature the full grain interior arc is no longer visible due to the frequency limitation of the equipment. However, the grain boundary arc can clearly be seen and is dramatically decreasing in resistance with grain growth (increased sintering time).

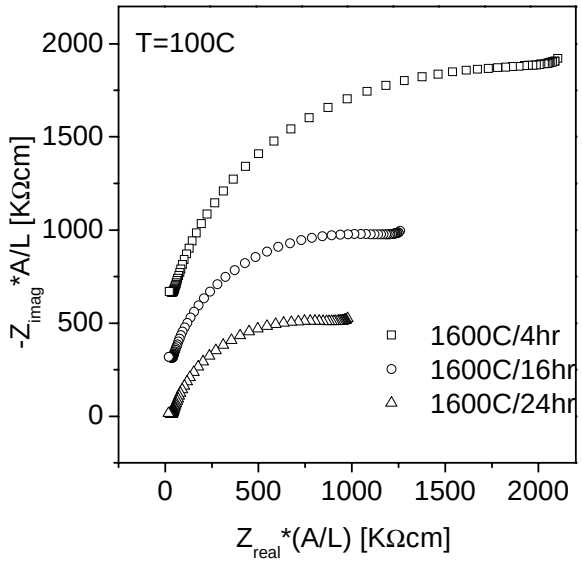

Figure 4.8. Nyquist plot of samples sintered at 4, 16, and 24 hrs at 100 ºC in saturated nitrogen (Ag electrodes).

Table 4.3. Summary of activation enthalpies and preexponential factors of the Arrhenius form.

Sintering time	**Grain interior**		**Grain boundary**		**Specific Grain boundary**	
	Ea [eV]	Log A	Ea [eV]	Log A	Ea [eV]	Log A
4 hrs	0.44	3.94	0.66	5.11	0.66	3.25
16 hrs	0.45	3.98	0.70	5.79	0.70	3.76
24 hrs	0.44	3.84	0.71	6.04	0.71	3.98

Total conductivity being the summation of both the grain interior and grain boundary conductivities, can therefore be increased by the optimization of the grain boundaries. One strategy, as we have shown to be successful, is the decrease in grain boundary density results in higher total grain boundary conductivity, Figure 4.9.

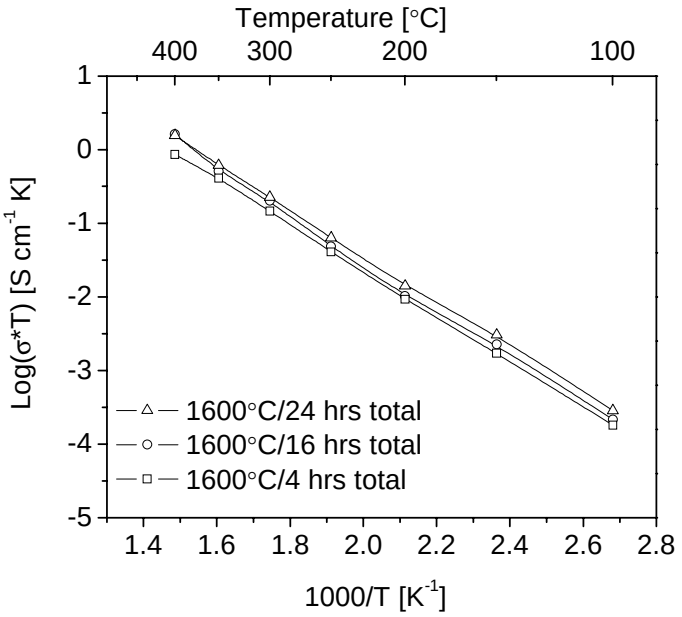

Figure 4.9. BYZ20 total (grain interior + grain boundary) conductivities (saturated nitrogen, P_{H20}=0.03 atm, Ag electrodes).

Comparing Figures 4.6 and 4.7 b it is clearly evident that the specific grain boundary conductivity is several orders of magnitude lower than that of the bulk. The blocking effects to proton transport across the grain boundary can be due to many reasons including crystalline impurities, amorphous phases, or intrinsic property of the boundary. Intrinsic grain boundary blocking was put forth by Guo and Maier [10] as a consequence of space charge regions. This concept originated after the realization that for high purity samples, where impurities were not observed with electron transmission microscope (TEM), the specific grain boundary conductivity was still found to be orders of magnitude lower than the bulk. A distribution of positively charged donor states (in our case, $Y_{gb}^{\bullet\bullet\bullet}$) within the grain boundary is electrically compensated by this space charge region. Each grain boundary consists of two adjacent space charge regions, Figure 4.10, showing an enrichment of negatively charged species (electrons and acceptors) and a

depletion of mobile positive charge carriers (oxygen vacancy and holes). The oxygen vacancy depletion was proposed as one of the causes for the grain boundary blocking effects.

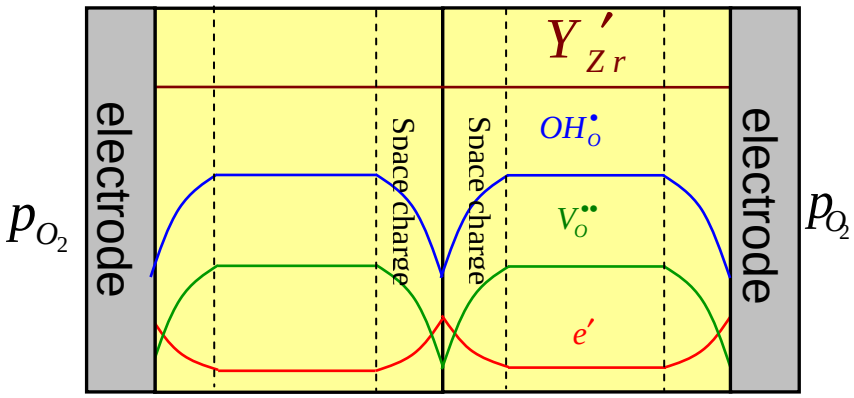

Figure 4.10. Schematic one grain boundary and adjacent space charge regions.

For one charge carrier with a charge of +1 (proton), the grain boundary space charge potential, ϕ, can be expressed as [11],

$$\frac{\sigma_{gi}}{\sigma_{sp.gb}} = \frac{e^{(e\phi/k_BT)}}{2e\phi/k_BT}, \tag{4.4}$$

where σ_{gi} is the grain interior conductivity, $\sigma_{sp.gb}$ is specific grain boundary conductivity and e, k_B, and T have their usual meanings. Calculated space charge potentials decrease with increasing sintering time, Figure 4.8. Decreasing potentials implies decreasing space charge layer thickness, which correlates well with the observation that grain boundary thickness is also decreasing, calculated independently from capacitance ratios (as described above). Although a more detailed instigation is required of the grain boundary, including high resolution microscopy, it is believed that high temperature in combination with long periods of sintering promotes the diffusion of B-site cations from cation-rich (Y^{+3} or Zr^{+4}) grain boundary core into the grain interior. Resulting in a less positive core (smaller potential), and overall smaller space charge layer. This suggests that

the grain boundary can not only be optimized by decreasing the overall density (increasing grain size), but can be intrinsically improved with longer sintering times, at least up to 24 hrs.

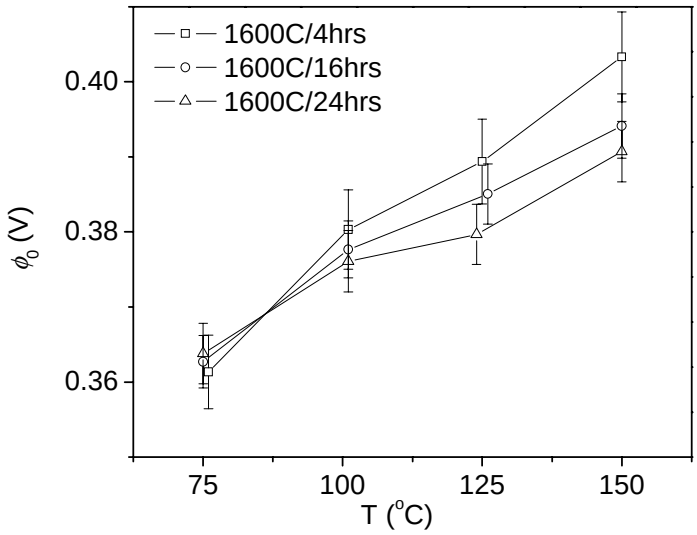

Figure 4.11. Calculated space charge potential of the grain boundary in BYZ20.

4.3 Dopant Concentration

4.3.1 Chemical Stability in Carbon Dioxide–containing Atmosphere

The chemical stability of higher Y doped barium zirconate powder was investigated under a CO_2 atmosphere balanced with argon. Powder samples were heated to 1400 ºC under a CO_2 (P_{CO2}=0.20) atmosphere, and subsequently cooled. Researchers have suggested that the formation of defects in the perovskite structure is not compatible with high stability of the oxide with CO_2 [12]. Dopant concentrations up to 25 Y mol % have been investigated previously [13] and this work expands the dopant concentration to 40 Y mol %. Higher doped samples, at least to 40 Y mol %, are stable in aggressive environments, Figure 4.12. In comparison, a barium cerate sample clearly forms barium carbonate in an identical environment inducing weight gain.

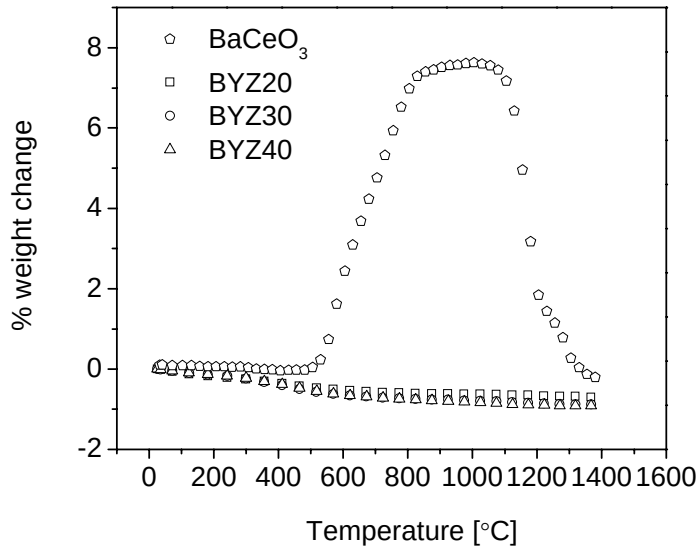

Figure 4.12. Weight gain as a function of temperature in P_{CO2}=0.20 balanced with argon.

4.3.2 Lattice Constants

Powder x-ray diffraction confirmed all samples were single phase perovskites after calcination at 1200 ºC for 5 hrs. Lattice parameters were found to increase linearly with dopant concentration suggesting the solubility limit of Y had not been reached. Increase in the lattice constant is due to the slightly larger ionic radius of the six-fold coordinated Y^{+3} (0.90 Å) ion compared to that of Zr^{+4} (0.72 Å) ion [14]. Lattice parameters reported in literature by Schober [15], Omate [16], Iguchi [1], and Keuer [13] are also plotted for comparison. The refined $BaZrO_3$ lattice parameter (4.193(1) Å) compares well with 4.1973 Å reported in the ICSD database 90049 [17].

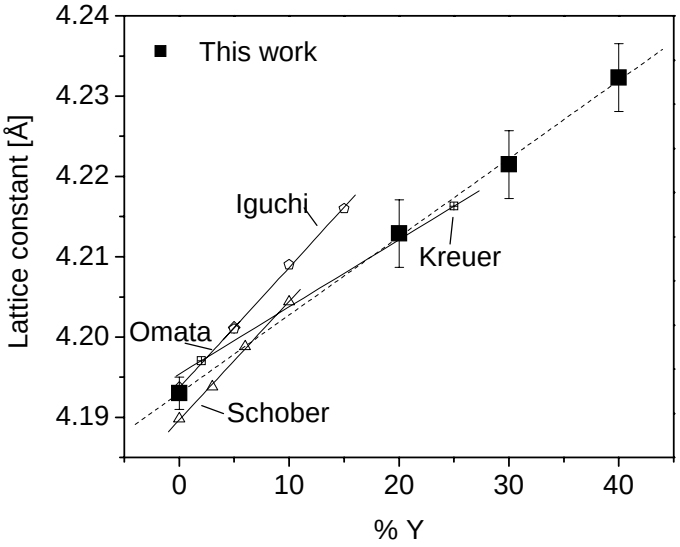

Figure 4.13. Lattice constant of cubic Y doped barium zirconate system.

4.3.3 Water Incorporation into the Structure

Recent reexamination of water vapor solubilites in the perovskite structure has shown solubilites close to those expected from acceptor doping and much higher than earlier reports [15]. Schober and Bohn observed a maximum proton content of 0.083, almost approaching the limit of 0.1 for a 10% Y doped barium zirconate system. Kreuer showed $BaCe_{0.9}Y_{0.1}O_{2.95}$ can reach 80% of the theoretical hydration level below 600 ºC [18]. As discussed in Chapter 1, in a humidified atmosphere, protonic defects can be incorporated into the perovskite structure to compensate for the oxygen vacancies according to Eq. (4.5).

$$H_2O + V_O^{\bullet\bullet} + O_O^x \leftrightarrow 2OH_O^{\bullet} \tag{4.5}$$

Thermogravametric analysis of sample weight gain while exposed to a water saturated (P_{H2O}=0.023) nitrogen atmosphere studies were conducted, Figure 4.14. Powder samples were heated and stabilized at a temperature of 1000 ºC in a dry atmosphere. Samples were then exposed to water saturated nitrogen (P_{H2O}=0.023 atm) and cooled in increments of 100 ºC with 2

hrs stabilization time per step. The final stabilization temperature of the sample was 50 ºC. The sample weight change was converted to mole of hydrogen per mole of BYZ, Figure 4.15. To probe the surface adsorption of water, a $BaZrO_3$ sample was also tested.

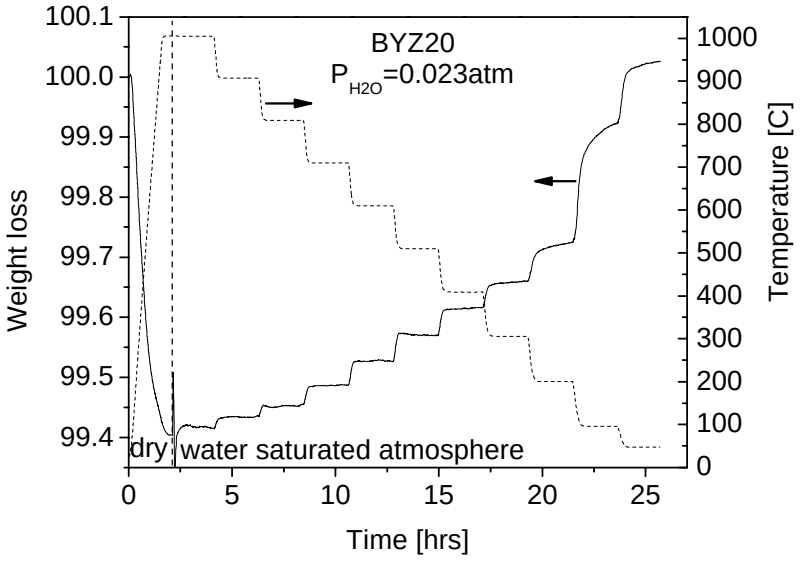

Figure 4.14. BYZ20 powder sample weight loss and temperature as a function of time.

$BaZr_{1-x}Y_xO_{3-\delta}$ where x = 0.2, 0.3, 0.4 all showed fully saturated structures at or below a temperature of 50 ºC with proton concentration exponentially decreasing with temperature. Shapes of the hydration isobars in this study were different from those measured by Kreuer [13]. Kreuer observed hydration to the theoretical limit (up to 20 mol % Y doped barium zirconate) at temperatures of 200 ºC. His hydration isobar for 25 mol % showed a more complex behavior, with the protonic defect concentration leveling at 8 mol % at 200 ºC. It is conceivable that 25 mol % Y sample would have reached its saturation limit if measurements were taken below 200 ºC. The 20 mol % Y sample, Figure 4.15, shows a saturation of ~9 mol% at 200 ºC, and approaches maximum theoretical solubility at 50 ºC. In the temperature range of interest for

electrochemical applications (400–600 ºC), the proton concentration is a small fraction of the solubility limit.

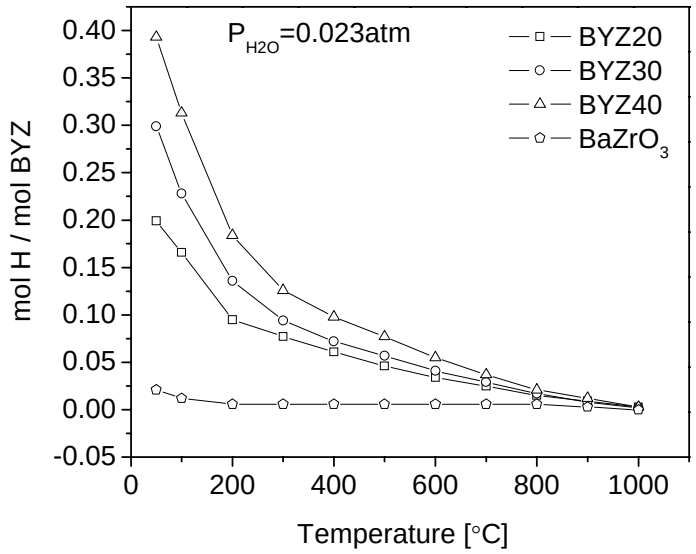

Figure 4.15. Molar percent of hydrogen per mol of BYZ in a water saturated atmosphere.

To independently confirm the proton solubilites, room temperature H NMR was considered. NMR measurements were performed on a Bruker DSX 500MHz spectrometer using magic angle spinning (12 kHz). To obtain quantitative data regarding the proton concentration, a measurement of 0.0196 g of water was used as reference and its area was assigned to 100%. Experimental samples were normalized for their weight, and adjusted with the reference water to obtain proton concentrations. NMR spectra, Figure 4.16, reveal one broad peak at approximately 4.9 ppm. Further, NMR and TGA results are summarized and compared in Table 4.4.

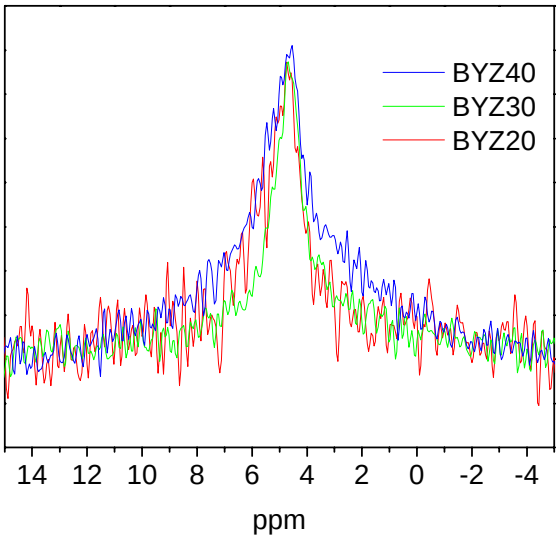

Figure 4.16. H NMR measurements of sample at room temperature.

Both TGA and NMR results agree on the near saturation of the structure at room temperature. TGA weight gain at each step can be analyzed to determine equilibrium constants of protonic defect incorporation into the structure, Eq. (4.5).

Table 4.4. Comparison of water incorporation by TGA and NMR (room temperature).

	TGA, mol H/ mol BYZ	NMR, mol H/ mol BYZ
BYZ20	0.19	0.23
BYZ30	0.29	0.33
BYZ40	0.39	0.47

The equilibrium condition for the water incorporation reaction, Eq. (4.5), is written as

$$K = \frac{[OH_O^{\bullet}]^2}{[V_O^{\bullet\bullet}][O_O^x]P_{H_2O}}. \qquad (4.6)$$

Utilizing oxygen site restriction, Eq. (4.7), where an oxygen site can only contain a vacancy, an oxygen atom, or a hydroxyl, with an electroneutrality condition, Eq. (4.8), combined with the expression for the equilibrium expression, Eq. (4.6), the equilibrium constant can be written as a function of protonic defect concentration, Eq. (4.9).

$$[V_O^{\bullet\bullet}]+[O_O^x]+[OH_O^\bullet]=3, \tag{4.7}$$

$$2[V_O^{\bullet\bullet}]+[OH_O^\bullet]-[Y_{Zr}']=0, \tag{4.8}$$

$$K=\frac{4[OH_O^\bullet]^2}{P_{H_2O}(6-[Y_{Zr}']-[OH_O^\bullet])([Y_{Zr}']-[OH_O^\bullet])}, \tag{4.9}$$

where $[Y_{Zr}']$ is the concentration of the acceptor dopant. Eq. (4.9) is used to calculate K from each temperature increment of the hydration experiment. As seen from Figure 4.17, approximate Arrhenius behavior can be observed in temperature ranges of 100 to 700 ºC. Fitting of this data will allow the determinations of standard hydration enthalpies and entropies, Eq. (4.10).

$$kT\ln K=T\Delta S_{hydra}-\Delta H_{hydra} \tag{4.10}$$

Hydration enthalpies and entropies are reported in Table 4.5 for the entire doped barium zirconate system. The numbers obtained here are significantly smaller than those obtained by Kreuer et al. [13]. Hydration enthalpies of -25 to -27 kJ/mol and hydration entropies of -42 to -43 J/mol/K are compared to Kreuer's reported ~ -79 to -93 kJ/mol and -93 to -103 J/mol/K, respectively. It should be noted that Kreuer isobars had the majority of weight loss in the temperature range of 400 to 800 ºC, and this region was fitted in the Arrhenius form. The thermodynamic data of the hydration reaction in this work is independent of dopant concentration. This observation was also made by Kreuer [13] up to 20 Y mol % dopant. It was suggested that the thermodynamics of hydration are dependent on acceptor dopant concentrations only when the dopant significantly changes the chemical character of the lattice oxygen. In the case of yttrium doped barium cerate [5], increasing yttrium doping concentration increased the lattice oxygen basicity. The increased OH bond strength due to the increased basicity of the oxide causes the increasingly negative

hydration enthalpies. Due to Y being isoelectronic (same valence electronic configuration) as Zr, the basicity of the lattice oxygen is not significantly changed due to doping. Further, hydration enthalpies are expected to be independent of dopant concentration, as observed.

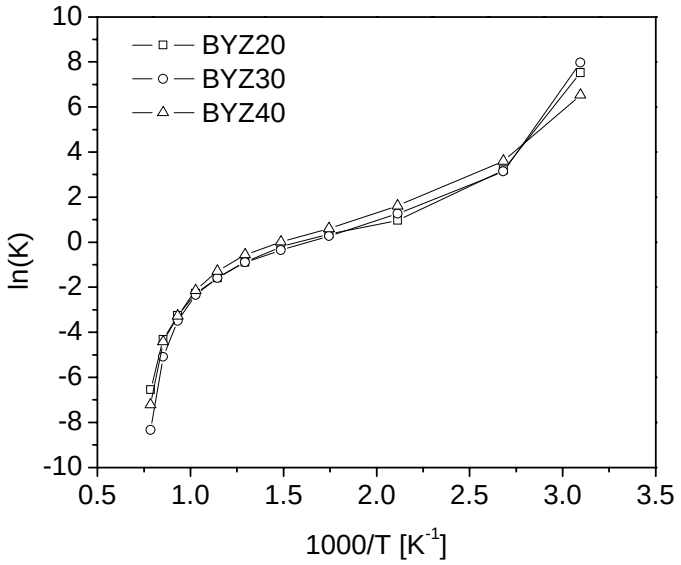

Figure 4.17. Equilibrium constant as a function of temperature.

Table 4.5. Standard enthalpy and entropy by assuming Arrhenius behavior in the 100 to 700 °C temperature range.

	ΔH kJ/mol	**ΔS J/(mol*K)**	**mol H/ mol BYZ**	**Reference**
BYZ20	-25	-42	0.19	This work
BYZ30	-26	-43	0.29	This work
BYZ40	-27	-42	0.39	This work
BYZ2	-80.9	-94.4	0.017	[13]
BYZ5	-79.5	-93.5	0.05	[13]
BYZ10	-79.4	-88.8	0.10	[13]
BYZ15	-83.4	-92.1	0.14	[13]
BYZ20	-93.3	-103.2	0.18	[13]

4.3.4 Conductivity

Grain interior conductivities measured from impedance spectroscopy are shown in Figure 4.18. Keuer et al [19] and Yajima et al [20] suggest there is no indication of significant interaction of the proton with the acceptor dopant. In contrast, defect association, specifically dopant-hydroxyl association can be observed for highly doped barium zirconate system at low temperatures. Water uptake experiments confirmed solubility limits for protons close to the theoretical. Conductivity of the grain interior of the BYZ40 is lower than that of BYZ20, especially at lower temperatures, Figure 4.18. Given the concentration of charge carriers is twice that of BYZ20 at 50 ºC, BYZ40 should have significantly higher conductivity at this temperature.

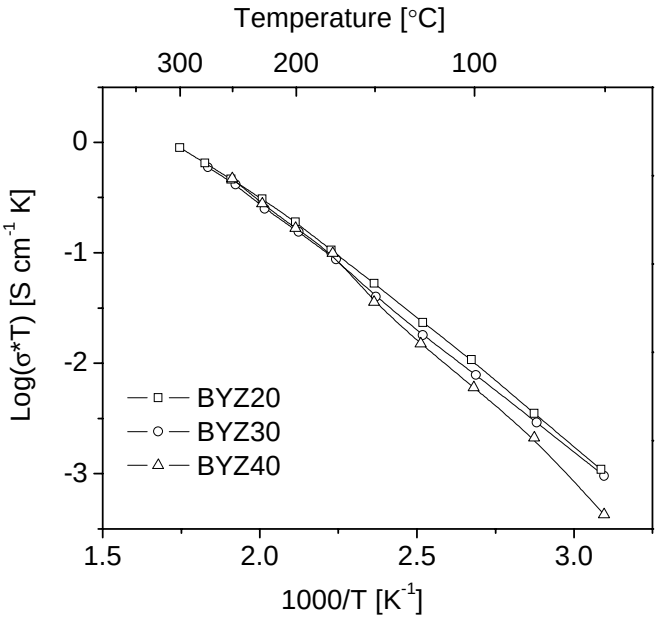

Figure 4.18. Grain interior conductivity of BYZ system with varying dopant concentration (saturated nitrogen, P_{H20}=0.03 atm, Ag electrodes).

Fitting the conductivity data in Arrhenius form allows for the determination of activation enthalpies and preexponential factors, Table 4.6. Experimental activation energies increase with dopant concentration, from 0.44 eV for BYZ20 to 0.49 eV for BYZ40. The activation enthalpy is a summation of both proton migration enthalpy and association enthalpy. As associations become more pronounced with increasing Y dopant, the total enthalpy is expected to increase. It is surprising that the preexpontential factor also increases with increasing dopant concentration. It was anticipated that only a fraction of charge carriers would be mobile due to the associations formed with the Y dopants, decreasing the "free" charge carriers in the perovskite structure. Increase of preexponential factor was also observed by Kreuer [13] from 2 to 20 mol % Y doped barium zirconate samples. At higher temperatures, expansion and softening of the lattice combined with comparable proton concentration of the three samples (BYZ20, BYZ30, and BYZ40) results in similar conductivities.

$$OH_O^{\bullet} + Y'_{Zr} \rightarrow (OH_o^{\bullet} \cdot Y'_{Zr})^x \quad (4.11)$$

In the case of Y doped barium cerate [5], Kreuer suggests the increase in activation enthalpies for the protonic defects with increasing dopant concentration may be related to a general increase in oxygen basicity rather than association cluster formations. As discussed above, doping barium zirconate with yttrium is not expected to significantly change the electron density on the oxygen ions (basicity) coordinated with the Y as opposed to coordinated with Zr; therefore, any change in activation enthalpies due to increased dopant concentrations can be attributed to hydroxyl-dopant associations.

Table 4.6. Summary of activation enthalpies and preexponential factor for the BYZ system with varying dopant concentration.

Y mol %	**20**	**30**	**40**
E_A [eV]	0.44	0.45	0.49
Log A	3.8	3.9	4.4
ε (Temp av.)	48	45	67

4.4 Conclusions

Optimization of the total conductivity of the barium zirconate system can be achieved through the control of its microstructure. Elongated sintering time results in grain growth, decreasing the grain boundary density. This was clearly shown to have beneficial effects on the total conductivity. In addition, an unexpected result was the intrinsic improvements of the grain boundary properties with increased sintering times. Grain boundary thickness as well as the space charge potential systematically decreased with increasing grain size, this was attributed to the redistribution of B-site charged cations from the grain boundary core to the grain interior.

Dopant concentration influence on the stability, unit cell, and proton solubility were examined. As anticipated, the lattice constant increased with increasing dopant concentration. This indicated the solubility up to 40 mol % Y in the barium zirconate system. Further, tests in aggressive environments showed even the highly doped (40 Y mol %) system to be stable. All structures were fully saturated at room temperature, with proton concentration dramatically decreasing with temperature. Hydration enthalpies and entropies were found to be independent of the dopant concentration due to the similarity in valence electron configuration of dopant Y and host Zr. Highly doped barium zirconate system (40 Y mol %) showed lower bulk conductivity than 20 Y mol %, which is attributed to significant hydroxyl-dopant association. The activation enthalpy increased with dopant concentration, suggesting the addition of association enthalpy to the proton migration enthalpy.

4.5 References

1. F. Iguchi, T. Yamada, N. Sata, T. Tsurui, H. Yugami. The Influence of grain structure on the electrical conductivity of a $BaZr_{0.95}Y_{0.05}O_3$ proton conductor. *Solid State Ionics* (in press 2007).

2. R. Hempelmann, M. Soetratmo, O. Hartmann and R. Wäppling. Muon diffusion and trapping in proton conducting oxides. *Solid State Ionics* **107**, 269 (1998).

3. T. Scherban and A. S. Nowick, Bulk protonic conduction in Yb-doped $SrCeO_3$. *Solid State Ionics* **35**, 189 (1989).

4. R. A. Davies, M. S. Islam, J. D. Gale. Dopant and proton incorporation in perovskite-type zirconates. *Solid State Ionics* **126**, 323 (1999).

5. K. D. Kreuer, W. Münch, M. Ise, T. He, A. Fuchs, U. Traub, and J. Maier. Defect Interactions in proton conducting perovskite-type oxide. *Ber. Bunsenges. Phys. Chem* **101**, 1344 (1997).

6. ASTM International E112–96. Standard Test Methods for Determining Average Grain Size. ASTM Committee E04 on Metallography and Subcommittee E04.08 on Grain size (2004).

7. I. Denk, J. Claus, and J. Maier. Electrochemical investigations of SrTiO3 Boundaries. *J. Electrochem. Soc.* **144**, 3529 (1997).

8. S. M. Haile, D. L. West, J. Campbell. The role of microstructure and processing on the proton conducting properties of gadolinium-doped barium cerate. *J. Mater. Res.* **13**, No. 6, 1576 (1998).

9. H. G. Bohn and T. Schober. Electrical conductivity of the high-temperature proton conductor $BaZr_{0.9}Y_{0.1}O_{2.95}$. *J. Am. Ceram. Soc.*, **83**, 768 (2000).

10. X. Guo and J. Maier. Grain Boundary Blocking Effects in Zirconia: A Schottky Barrier Analysis. *J. Electrochem. Soc.* **148** (3), E121 (2001).

11. J. Fleig, S. Rodwald, and J. Maier, *J. Appl. Phys* **87**, 2372 (2000).

12. K. D. Kreuer. Proton Conducting Oxides. *Annu. Rev. Mater. Res.* **33**, 333 (2003).

13. K. D. Kreuer, St. Adams, W. Münch, A. Fuchs, U. Klock, and J. Maier. Proton conducting alkaline earth zirconates and titanates for high drain electrochemical applications. *Solis State Ionics* **145**, 295 (2001).

14. R. D. Shannon. Revised effective ionic radii and systematic studies of interatomic distances in halides and chalcogenides. *Acta Cryst.* **A32**, 751 (1976).

15. T. Schober and H.G. Bohn. Water vapor solubility and electrochemical characterization of the high temperature proton conducting $BaZr_{0.9}Y_{0.1}O_{2.95}$. *Solid State Ionic* **127**, 351 (2000).

16 T. Omata, M. Takagi and S. Otsuka-Yao-Matsuo. O–H stretching vibrations of proton conducting alkaline-earth zirconates. *Solid State Ionics* **168**, 99 (2004).

17. T. Pagnier, I. Charrier-Cougoulic, C. Ritter, G. Lucazeau. A neutron diffraction study of $BaCe_xZr_{1-x}O_3$. *The European Physical Journal Applied Physics* **9**, 1. ICSD database code 90049 (2000).

18. K. D. Kreuer. Aspects of the formation and mobility of proton charge carriers and the stability of perovskite-type oxides. *Solid State Ionics* **125**, 285 (1999).

19. K. D. Kreuer, Th. Dippel, Y.M. Baikov, and J. Maier. Water solubility, proton and oxygen diffusion in acceptor doped $BaCeO_3$: A single crystal analysis. *Solid State Ionic* **86-88**, 613 (1996).

20. T. Yajima and H. Iwahara. Studies on behavior and mobility of protons in doped perovskite-type oxides: (I) in situ measurement of hydrogen concentration in $SrCe_{0.95}Yb_{0.05}O_{3-a}$ at high temperature. *Solid State Ionic* **50**, 281 (1992).

Chapter 5: Enhanced Sintering of Yttrium doped Barium Zirconate by addition of ZnO

5.1 Introduction

As previously discussed in Chapter 3, the refractory nature of doped barium zirconate leads to significant challenges to its implementation in fuel cells and other electrochemical devices. Processing high density (>93%), high conductivity doped barium zirconate is difficult and requires high sintering temperature (1600 °C), long sintering times (24 hrs), and nanometer-sized particles (Chapter 3). Not only are these conditions costly to implement, they are incompatible with most potential electrode materials and thereby preclude the fabrication of co-sintered structures. Further, it is the total resistance of the electrolyte, not only that of the bulk (or grain interiors), that dictates electrochemical performance. Thus, strategies for improving total grain boundary conductivity are required. In addition, high temperature processing induces barium oxide evaporation (also observed with barium cerate compounds [1]), decreasing the BYZ grain interior conductivity by 2–3 orders of magnitude (Chapter 3). Last, abnormal grain growth [2] results in inhomogeneous properties, both electrical and mechanical, which are highly undesirable.

In the present chapter we demonstrate that ZnO is an effective sintering aid for $BaZr_{0.85}Y_{0.15}O_{3-\delta}$, (BYZ15) enhancing both densification and uniform grain growth. Yttrium has been selected as the dopant because of the high proton conductivity this species imparts, presumably as a result of its good ionic radius match to Zr [5]. Of potential sintering aids, a previous study of Al_2O_3, MgO, and Y_2O_3 on barium zirconate densification showed a marginal improvement in sintering behavior with yttria. This additive yielded samples of 91%-92% dense at 1600 °C as compared to ~90% density for pristine samples processed under identical conditions [6]. While no detailed mechanism for the slight enhancement in density was presented,

it was speculated that yttria limits grain growth. In this chapter, an initial screening of all transition elements in the series Sc to Zn, as discussed below, showed NiO, CuO and ZnO to be the most effective additives for enhancing barium zirconate densification. Of these, zinc oxide was selected as most suitable and accordingly subjected to further investigation and system optimization.

5.2 Preliminary comparison of transition-metal modifiers

Preliminary modifier screening experiments were carried out by mechanical addition of 4 mol% of the transition metal oxide (Alfa Aesar, 99.9%- 99.99% purity) to the $BaZr_{0.85}Y_{0.15}O_{3-\delta}$ powder synthesized via glycine-nitrate combustion process as described in Chapter 2. Powder was calcined at 1000 °C for 2 hrs to yield well-crystallized BYZ powders, which were subsequently attritor milled at 550 rpm for 2 hrs to produce uniform, submicron particles with approximate surface area of 8 m^2/g. The stoichiometry of the BYZ base material was not adjusted to accommodate the modifier and no assumptions about site incorporation mechanisms are made.

Densities obtained from 4 mol % transition-metal modified BYZ samples, sintered at 1300 °C with a 4 hrs soak time, are shown in Figure 5.1. As evident from the data, Ni, Cu, and Zn are tremendously effective in enhancing densification, raising the final density from about 60% of theoretical for the unmodified material to approximately 86%-88% for modified BYZ. Other additives such as V, Cr and Fe, in contrast, substantially worsened densification behavior. Powder x-ray diffraction of both vanadium and chromium combined with BYZ showed the presence of second phases, which is contributing to the densification worsening.

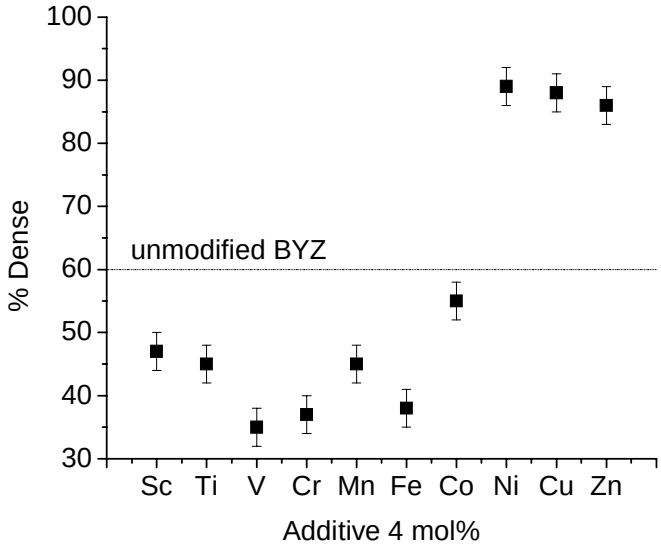

Figure 5.1. Effect of transition metal oxide additives as sintering aids for BYZ.

Diffraction patterns obtained after sintering, from BYZ modified with the favorable elements, are presented in Figure 5.2. In all three cases, a single perovskite phase is indicated. However, upon closer examination under the SEM, Figure 5.3, the Cu modified sample showed the presence of $Ba_2YCu_3O_x$. In addition, both this material and the Ni modified BYZ pellet changed color from white to black upon sintering. In contrast, the Zn modified sample acquired a pale green color. Often, black coloring in an oxide indicates substantial electronic conductivity, and even though the transition metal concentration in these samples is low, suggesting the electronic transference number would not be large, Cu and Ni were abandoned as modifiers in favor of Zn.

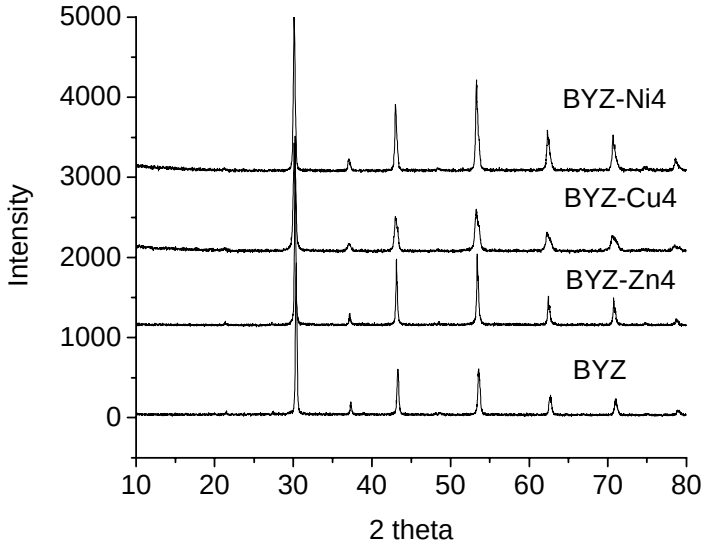

Figure 5.2. X-ray powder diffraction patterns of sintered BYZ, BYZ-Zn4, BYZ-Cu4, and BYZ-Ni4.

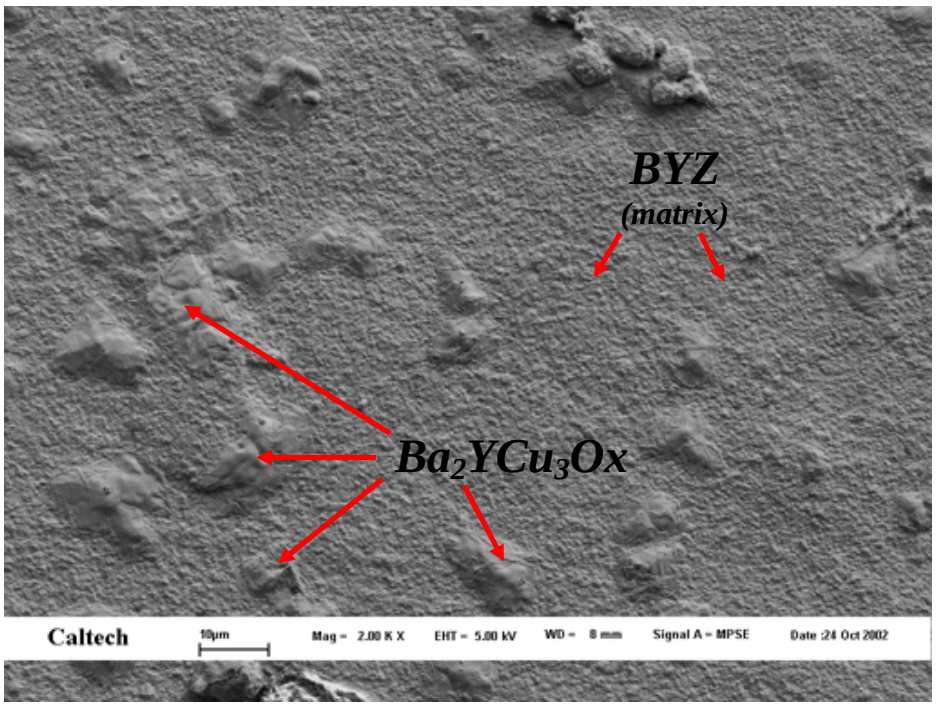

Figure 5.3. Surface of sintered (1300 °C) BYZ-Cu4 sample showing the presence of $Ba_2YCu_3O_x$.

The impact of ZnO content on the sintering behavior of BYZ (samples prepared by mechanical mixing of the two oxides, 1300°C, 4 hrs) is presented in Figure 5.4. Densification, as measured in terms of total linear shrinkage, dramatically increased in the range from 0 to 4 mol % Zn then remained at a constant intermediate value for higher Zn concentrations. Although this behavior was established only for Zn in particular, it is because of this concentration dependence of densification that 4 mol% was selected for the preliminary screening of transition metal elements as modifiers.

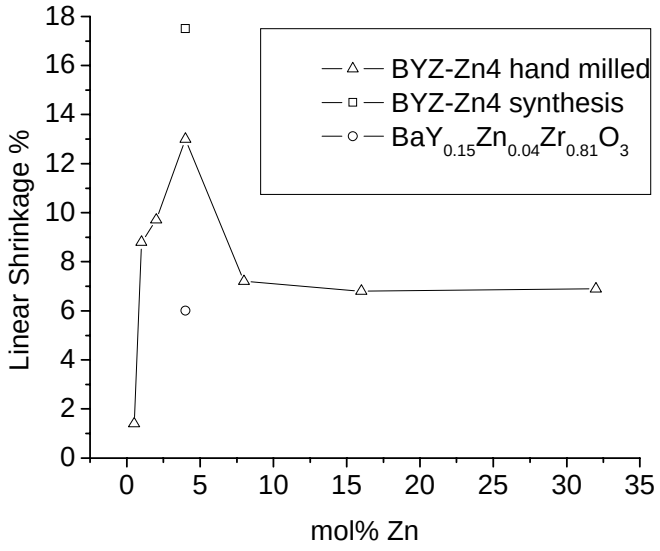

Figure 5.4. Linear shrinkage of Zn modified $Ba(Zr_{0.85}Y_{0.15})O_3$ after sintering at 1300°C in air (4 hrs) as a function of mole percentage of ZnO. △ = mechanical addition; □ = Zn oxide addition to BYZ nitrate solution; ○ = zinc nitrate addition to BYZ nitrate solution.

In the case of ZnO, two additional synthesis routes were explored. The first involved dissolution of zinc nitrate (Alfa Aesar, 99% purity) directly into the BYZ nitrate solution described above, the stoichiometry was adjusted to incorporate the Zn in the B site of the perovskite ($BaY_{0.15}Zn_{0.04}Zr_{0.81}O_{3-\delta}$). In the second method, ZnO (Alfa Aesar 99.99% purity,

surface area of 8.5 m^2/g) was introduced as an oxide powder to the BYZ nitrate solution just prior to complete dehydration. With the latter technique, the stoichiometry of the BYZ base materials was not adjusted to accommodate the ZnO.

The impact of different methods of ZnO addition on the densification of BYZ is also presented in Figure 5.4, in which the linear shrinkage of BYZ-Zn4 prepared by the three different routes are compared. Of the three BYZ-Zn4 samples, densification is greatest for ZnO introduced as a dispersed oxide into the BYZ nitrate solution. The improvement over mechanical mixing of the two oxides is attributed to the greater homogeneity of the ZnO distribution within the ceramic. Further evidence of homogeneity is seen by SEM images of the surfaces of samples prepared by different routes, Figure 5.5. Clearly the addition of ZnO to BYZ via the milling process produces abnormal grain growth with a wide distribution of grain sizes. The poorer densification of the presumably most homogenous sample, that in which zinc nitrate was added to the BYZ nitrate solution, is attributed to the complete dissolution of Zn into the bulk crystalline structure of BYZ without significant preferential segregation to the grain boundaries. In comparison to the unmodified sample, however, even this sample shows enhanced shrinkage over simple BYZ. All subsequent studies were performed with materials prepared via introduction of zinc oxide to the BYZ nitrate solution.

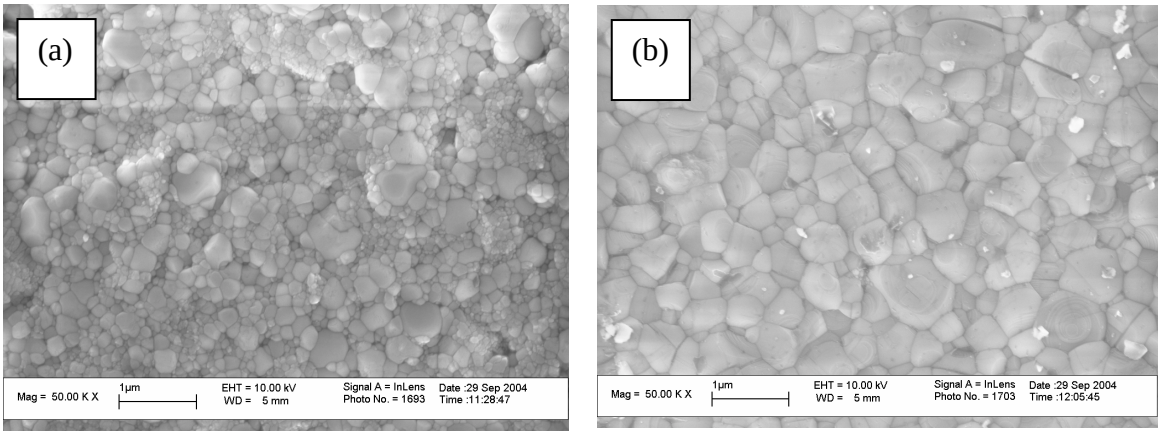

Figure 5.5. Surfaces of BYZ-Zn4 pellet sintered at 1300 ºC for 4 hrs (a) ZnO added to BYZ via milling (b) ZnO added to the BYZ nitrate solution.

5.3 Densification with ZnO

The difference in sintering behavior between unmodified and Zn-modified BYZ is particularly evident from a comparison of the dilatometry curves obtained from the two materials, Figure 5.6.

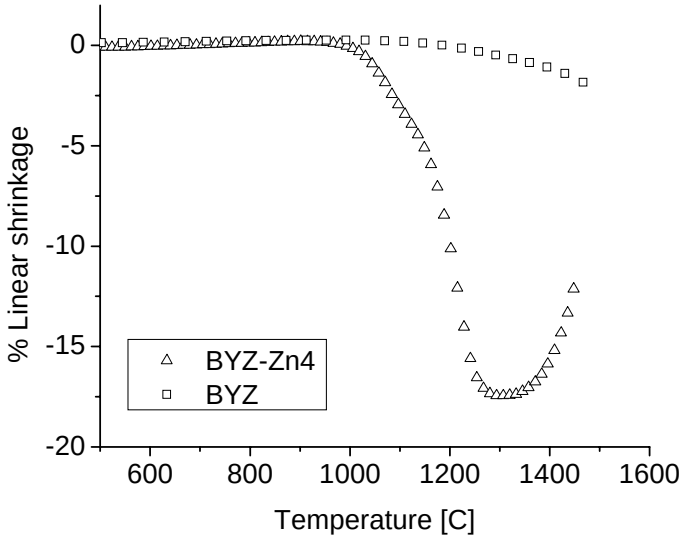

Figure 5.6. Temperature dependence of linear shrinkage in BYZ and BYZ-Zn4.

Dilatometry experiments, permitting *in situ* measurements of linear shrinkage as a function of temperature, were performed with a Dilatronic dilatometer (Theta Industries). Data were collected at a heating rate of 3 °C /min under a stagnant air atmosphere. The onset of sintering in BYZ-Zn4, occurs at approximately 1000 °C, 200 °C before its onset in the BYZ system. Furthermore, between 1000 and 1100 °C BYZ-Zn4 shrinkage is ~4%, whereas it is only ~1% for BYZ over the temperature range of 1200 to 1300 °C. At 1300 °C the total linear shrinkage for BYZ-Zn4 is 17.5% (as compared to only ~1% for BYZ).

Additional comparisons between the behavior of BYZ-Zn4 (optimally synthesized) and unmodified BYZ are presented in Figures 5.7 and 5.8, in which the post sintering densities as a function of temperature and selected micrographs, respectively, are shown.

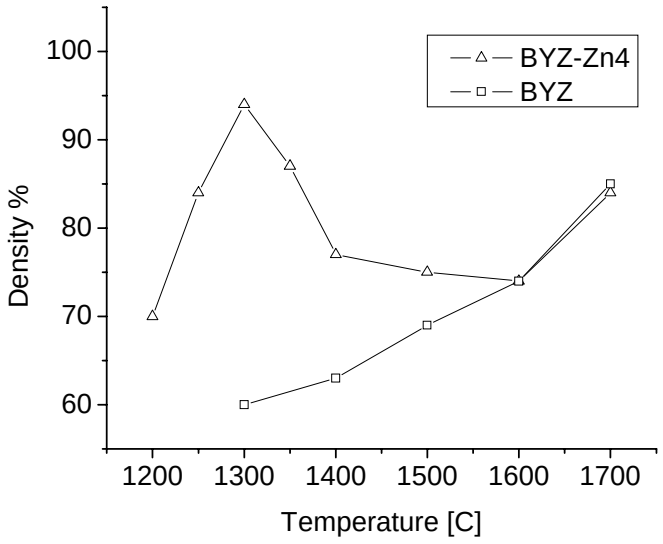

Figure 5.7. Density of BYZ and BYZ-Zn4 as a function of sintering temperature in ambient atmosphere.

As evident from Figure 5.7, the maximum densities that could be achieved from these two materials differ significantly: 95% of theoretical for BYZ-Zn4 (ρ_{theo} = 6.12 g/cm^3), at a

sintering temperature of 1300 °C, compared to only 88% for BYZ, at a sintering temperature 1700 °C. At 1300 °C, the density of unmodified BYZ is only ~60%. The electron micrograph images for the two different samples obtained after sintering at 1300 °C confirm the macroscopic observations. The BYZ system has considerable porosity (~40%) after sintering at this low temperature, Figure 5.8 a, whereas the BYZ-Zn4 system appears dense and has larger mean grain size (0.18 vs. 0.47 μm), Figure 5.8 b & 5.8 d. The images (examined in combination with EDS chemical analysis) furthermore reveal that the BYZ-Zn4 system is free of secondary phases.

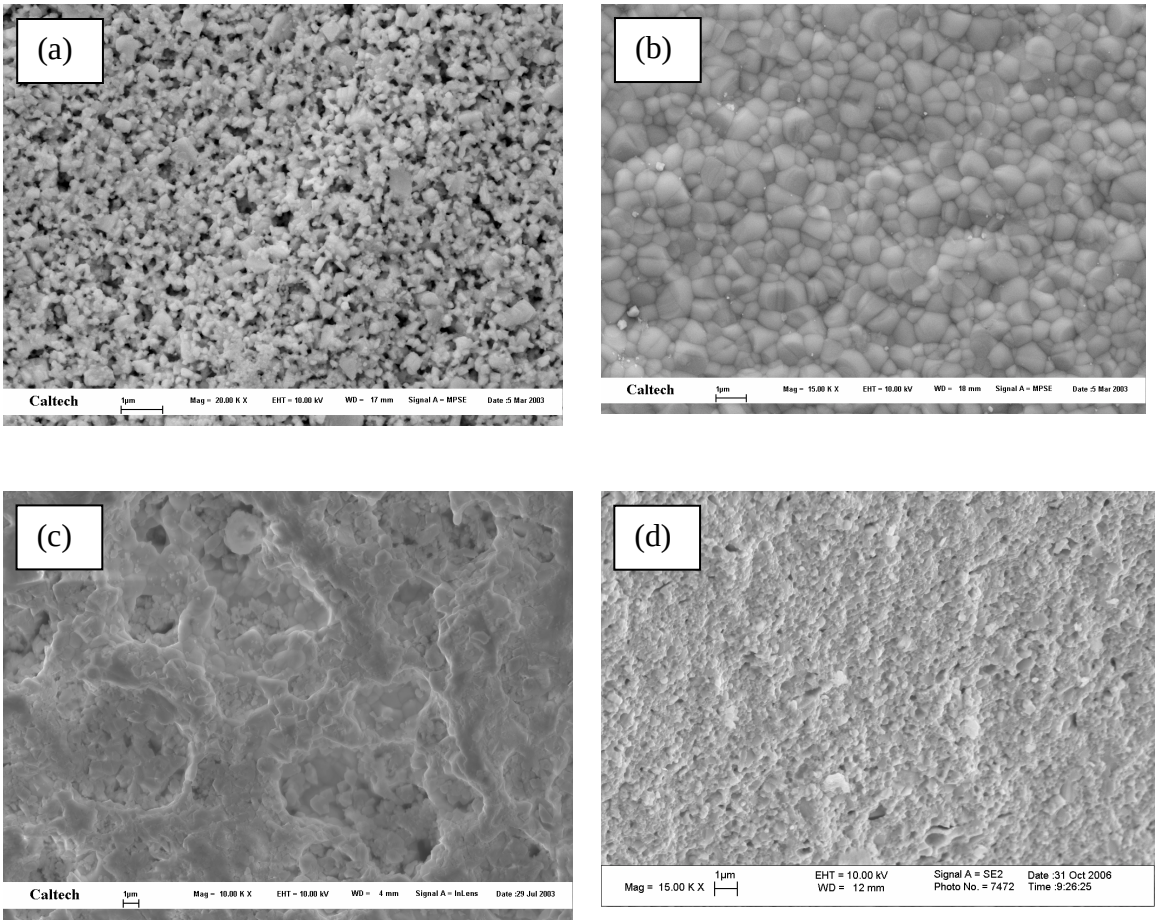

Figure 5.8. SEM micrograph of sintered (a) BYZ at 1300 ºC, (b) BYZ-Zn4 at 1300 ºC, (c) BYZ-Zn4 at 1400 ºC, and (d) fracture surface of BYZ-Zn4 at 1300 ºC.

The temperature dependence of sample density differs dramatically between the Zn modified and unmodified materials, Figure 5.7. For the former a highly obvious maximum in density as a function of sintering temperature exists, occurring at 1300 °C, whereas the latter shows a monotonically increasing density as a function of sintering temperature. The dilatometry data, Figure 5.6, similarly shows a loss in density for BYZ-Zn4 exposed to temperatures above 1300 °C. This decrease in density is accompanied by an unusual change in microstructure, Figure 5.8 c, in which individual grains can no longer be distinguished. The decreasing density of BYZ-Zn4 is thought to result from evaporation of Zn at elevated temperatures according to Eq. (5.1).

$$ZnO(s) \leftrightarrow Zn(g) + \frac{1}{2}O_2(g) \tag{5.1}$$

This conclusion is supported by preliminary observations that ZnO is effective as a sintering additive only in relatively oxidizing atmospheres (air). Under reducing atmospheres, Eq. (5.1) is driven to the right and metallic zinc readily vaporizes. Indeed, under an atmosphere with 10^{-6} bar O_2 partial pressure, the partial pressure of Zn at 1300 °C, based on available thermodynamic data [7], is approximated as 10^{-2} bar, indicating significant zinc loss.

5.4 Chemical Analysis

The diffraction and microscopy studies, Figures 5.2 and 5.8, respectively, indicate that BYZ-Zn4 is free of obvious secondary phases, which may have served to enhance sintering through the formation of a eutectic melt. However, these techniques provide little information about the distribution of Zn within the polycrystalline perovskite. Of particular relevance is whether there is any difference in Zn concentration between bulk and grain boundary regions.

The microstructure and chemical composition of sintered samples were investigated by means of scanning electron microscopy (LEO 1550VP Field Emission SEM) in conjunction with EDS (Energy Dispersive X-ray Spectroscopy, Oxford INCA Energy 300). Exposed top surface of

the sample was polished in preparation for chemical analysis. The Oxford INCA EDS software employs the PAP (Pouchou and Pichoir) model for quantitative analysis [8] in which fundamental factors are used to correct for the effects of atomic number, absorption, and fluorescence to the measured intensity of the elements. Accordingly, standards are not necessary.

The results of chemical analysis as determined by quantitative analysis of the EDS spectra are presented in Table 5.1 (for BYZ-Zn4 sintered at 1300 °C). The mol % are normalized to one unit of barium. The bulk composition appears slightly barium deficient, possibly an artifact of the experimental technique in that EDS rather than more quantitative WDS (wavelength dispersive X-ray spectroscopy) has been employed. More importantly, within the detection limit, there is no Zn within the grain interiors. In contrast, the grain boundaries have a substantial concentration of Zn, almost 5 mol %, and this coincides with a decrease in the Y concentration by about 3 mol % relative to that in the bulk. Furthermore, the grain boundaries exhibit a slightly greater barium deficiency.

Table 5.1. Chemical compositional comparison of the bulk and grain boundary in the BYZ-Zn4 densified system.

	Zn	Y	Zr	Ba	O
Bulk	0.000	0.099	0.914	1.000	2.947
Bulk	0.000	0.126	0.936	1.000	3.025
Bulk	0.003	0.166	0.928	1.000	3.107
Bulk	0.000	0.099	0.915	1.000	2.972
Average bulk	**0.001**	**0.123**	**0.923**	**1.000**	**3.013**
Grain boundary	0.012	0.085	0.915	1.000	2.970
Grain boundary	0.057	0.091	0.930	1.000	3.053
Grain boundary	0.078	0.087	0.936	1.000	3.080
Grain boundary	0.047	0.104	0.951	1.000	3.104
Average grain boundary	**0.049**	**0.092**	**0.933**	**1.000**	**3.052**

In light of the chemical analysis, the enhanced densification observed here is assumed to be a result of the high Zn concentration in the grain boundary regions. Given the slightly larger mean grain size of BYZ-Zn4 than simple BYZ for samples sintered at 1300 °C, Figure 5.8, it is apparent that Zn slightly increases grain boundary mobility. In contrast, Caballero et al. [9] observed that introduction of very small concentrations of ZnO to $BaTiO_3$ dramatically inhibited grain growth but, nevertheless, marginally improved densification. Grain boundary mobility in oxides is limited by the diffusivity of the slowest moving species [10] and in the case of perovskites these are the cations. In the grain boundary regions of BYZ-Zn4, the Zn appears to be

incorporated on the B site of the perovskite, which could be expected to increase the vacancy concentrations on both the Ba and oxygen sites:

$$ZnO \rightarrow Zn''_{Zr} + O_O + V''_{Ba} + 2V_O^{\bullet\bullet}. \quad (5.2)$$

The increase in barium vacancy concentration, may, in turn, be responsible for the increase in grain boundary mobility, grain growth, and densification. Such a mechanism may also, in part, explain the marginal impact of Zn on BYZ sintering when added to yield an overall composition of $Ba(Zr_{1-x}Y_yZn_z)O_{3-\delta}$, as was the case for the samples in which zinc nitrate was directly introduced into the BYZ nitrate solution.

5.5 Chemical Stability

In order to assess chemical stability, thermal gravimetric analysis (TGA) of selected samples was carried out under flowing CO_2 (P_{CO2}=0.20) using a Netzsch STA 449 C Jupiter. For this purpose, samples were lightly sintered to a density of 60%–65% of theoretical. Barium cerate ($BaCeO_3$), for comparison of chemical stability with BYZ, was synthesized.

A comparison of the thermal gravimetric behavior of BYZ, BYZ-Zn4 and $BaCeO_3$ in the presence of CO_2 is presented in Figure 5.9. Consistent with earlier observations [1], gradual weight gain is apparent for the $BaCeO_3$ above 600 °C signifying the formation of $BaCO_3$ as per Eq. (5.3)

$$BaCeO_3 + CO_2 \rightarrow BaCO_3 + CeO_2 \quad (5.3)$$

In contrast, BYZ and BYZ-Zn4 show no significant weight gain. Thus, the ZnO additive does not impact the excellent stability of barium zirconate in carbon dioxide containing atmospheres.

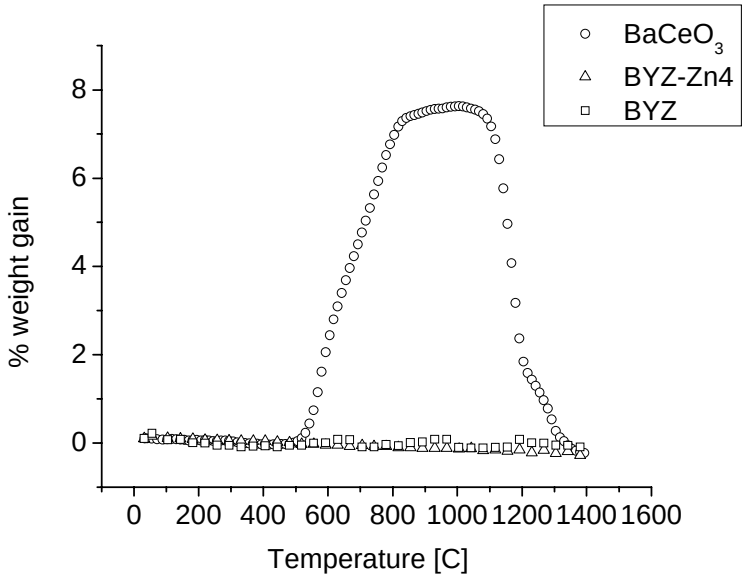

Figure 5.9. Thermogravimetric analysis of BYZ-Zn4 and BYZ as compared to $BaCeO_3$ in a CO_2 atmosphere (P_{CO2}=0.20).

Due to the high vapor pressure of Zn, especially in a reducing atmosphere, it was important to address the stability of Zn in hydrogen atmospheres at appropriate operating temperatures. Although the BYZ-Zn4 sample changes color from a pale green to a yellow upon treatment at 600 ºC in a reducing atmosphere, there is no evidence of increased porosity due to the evaporation of Zn, Figure 5.10. The stability of BYZ-Zn at 600 ºC in hydrogen is critical to the development and testing of electrochemical devices such as fuel cells.

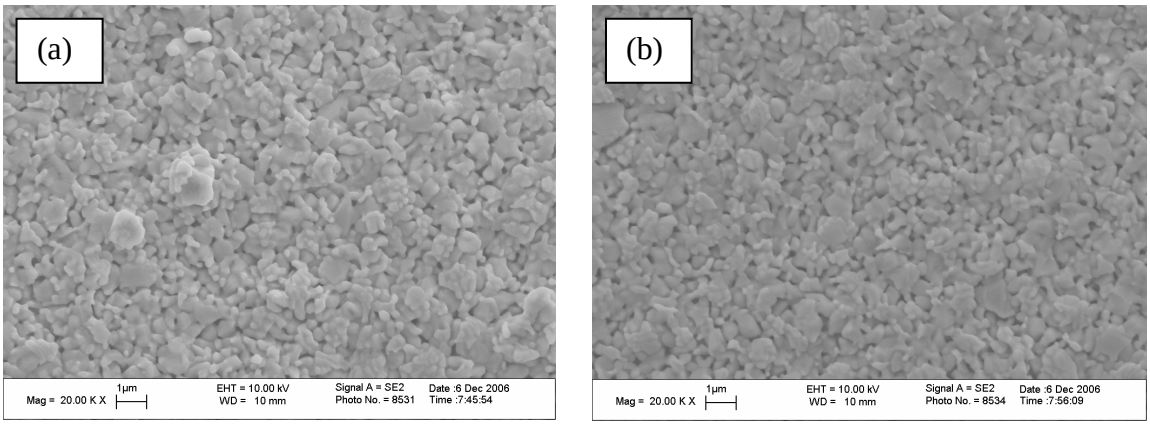

Figure 5.10. SEM fracture surface image of (a) BYZ-Zn4 and (b) BYZ-Zn4 after 24 hrs treatment in pure H_2 at 600 ºC.

5.6 Transport Properties

The conductivity of densified pellets of 4 mol% ZnO modified BYZ (BYZ-Zn4) were measured under water-saturated nitrogen in the temperature range of 50–350 °C. The BYZ-Zn4 sample was that prepared by the zinc oxide + BYZ nitrate route and sintered at 1300 °C for 4 hrs (93% dense). Impedance data were collected over the frequency range of 10^3–10^6 Hz using a HP 4284A precision LCR meter at an applied voltage of 1V. It should be noted that the samples were not electrochemically decomposed due to the voltage bias. Platinum electrodes were sputtered onto the surfaces of polished samples.

Nyquist plots (Z_{real} vs. Z_{imag} as parametric functions of frequency) obtained at selected temperatures for BYZ-Zn4 under water-saturated nitrogen are shown in Figure 5.11. In the temperature range of 120 to 160 °C the impedance spectra consisted of two semicircles. The low frequency arc is attributed to grain boundary processes whereas the high frequency arc is attributed to the bulk response [11–13]. With increasing temperature, these two arcs shift towards higher frequencies and by ~230 °C a third feature, which corresponds to the electrode response, appears at the low frequency end of the spectrum [11, 14, 15]. At a temperature of ~250 °C the

characteristic frequency of the bulk response reaches a value greater than the maximum measurement frequency of the impedance meter and thus the bulk arc is no longer accessible.

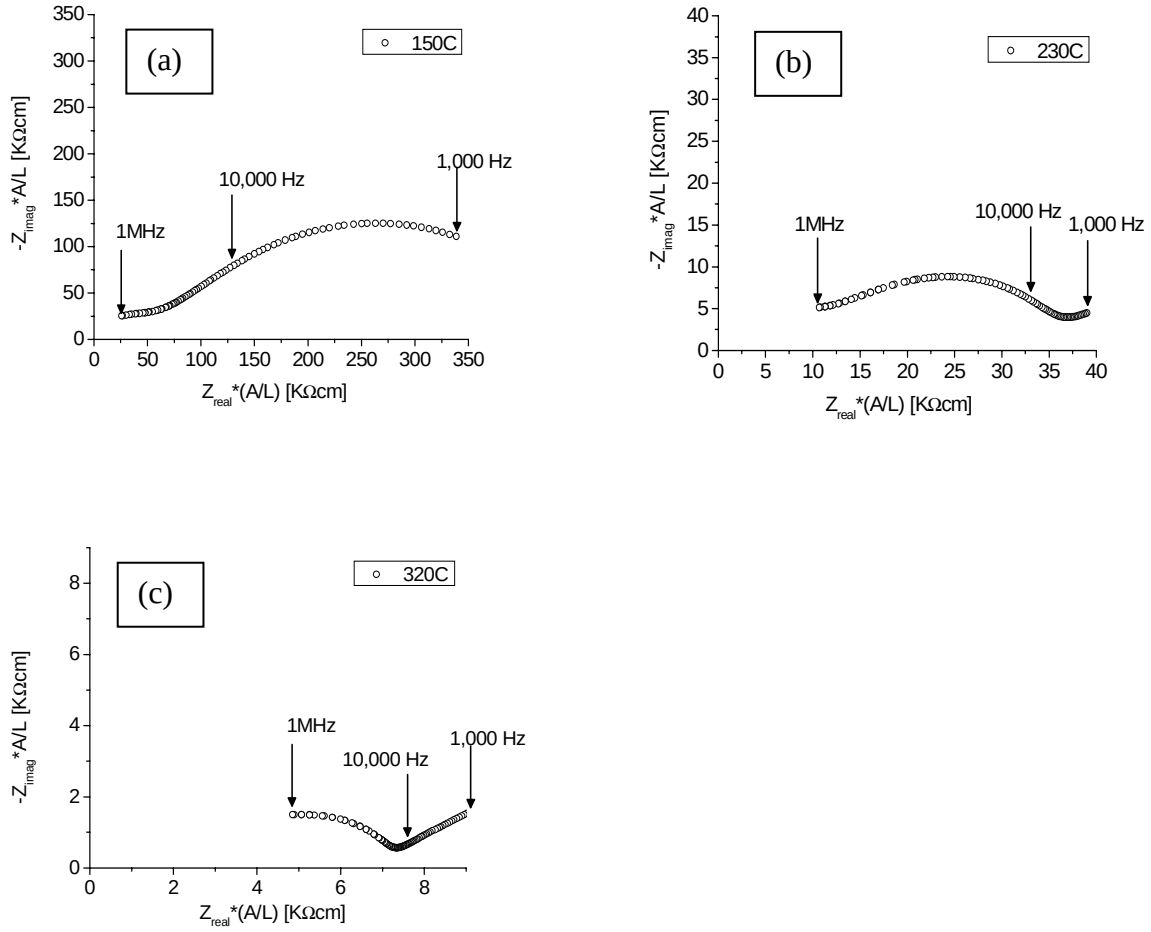

Figure 5.11. Nyquist impedance plots for BYZ-Zn4 obtained at (a) 150 ºC, (b) 230 ºC, and (c) 320 ºC in water-saturated nitrogen atmosphere (sputtered Pt electrodes.)

After least-squares fitting to the impedance data to obtain the resistances associated with the high and intermediate frequency arcs, the conductivities of the bulk and grain boundary regions were deduced by accounting for the sample geometry according to Eq. (5.4):

$$\sigma = \frac{1}{R} * \frac{L}{A} \tag{5.4}$$

where L is the sample thickness and A is its cross-sectional area. As introduced in Chapter 1, the specific grain boundary conductivity (independent of microstructure), $\sigma_{sp.gb}$, was determined using:

$$\sigma_{sp.gb} = \frac{L}{A}\left(\frac{C_{bulk}}{C_{gb}}\right)\frac{1}{R_{gb}} \tag{5.5}$$

A temperature averaged (single) value of the ratio C_{bulk}/C_{gb} [= 0.0182] was employed for these calculations.

The temperature dependences of the bulk (or grain interior), total grain boundary and specific grain boundary conductivities of BYZ-Zn4 are presented in Figure 5.12. The data obtained from BYZ-Zn4 are compared to the bulk and total grain boundary conductivities of $BaZr_{0.90}Y_{0.10}O_3$ (BYZ10) as reported by Bohn and Schober [14], and to the specific grain boundary conductivity of $BaCe_{0.85}Gd_{0.15}O_3$ as reported by Haile et al. [13]. In Table 3.2 are listed the activation energies, E_a, and preexponential terms, A, determined from a fit of the data to the Arrhenius equation

$$\sigma T = A\exp(-E_a / k_b T), \tag{5.6}$$

where T, and k_b are temperature and the Boltzman constant, respectively.

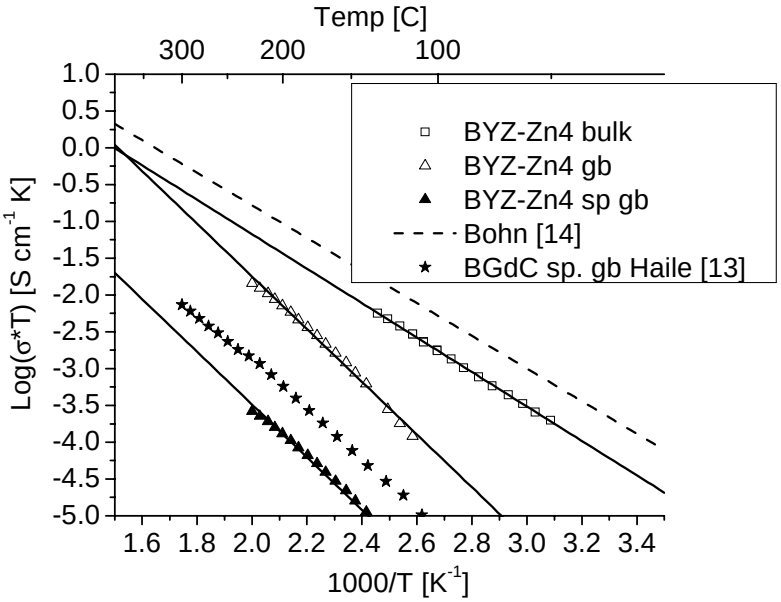

Figure 5.12. The bulk, total grain boundary, and specific grain boundary conductivity of BYZ-Zn4 as a function of temperature plotted in Arrhenius form. Atmosphere is water-saturated nitrogen (Pt electrodes). Data are compared to those of Bohn [14] for the bulk conductivity of unmodified $BaZr_{0.9}Y_{0.1}O_3$ and those of Haile [13] for the specific grain boundary conductivity of $BaCe_{0.85}Gd_{0.15}O_3$.

Table 5.2. Comparison of activation energies and pre-exponential factor of bulk and grain boundary conductivity of BYZ-Zn4 and BYZ.

	BYZ-Zn4	Bohn [14]
E_a, bulk [eV]	0.47(1)	0.44
Log A, bulk [K S/cm]	3.51	
E_a, gb [eV]	0.71(1)	0.7
Log A, sp gb [K S/cm]	3.67	
Log A, tot gb [K S/cm]	5.41	

From the results presented in Figure 5.12, it is immediately apparent that the bulk conductivity of BYZ-Zn4 is lower than that of BYZ10, by a factor of two. Furthermore, differences appear in the activation energy for proton transport, 0.47 vs. 0.44 eV for BYZ-Zn4 and BYZ10, respectively, and the preexponential term, 10^3.51 vs. 10^3.65, respectively. This result is particularly surprising in light of the chemical analysis, which suggests that little if any Zn is incorporated within the bulk structure of BYZ-Zn4. Moreover, the dopant (yttrium) concentration in BYZ-Zn4, 15%, is greater than in BYZ10, 10%, suggesting a higher proton concentration and thus larger preexponential term in the former. That the opposite is observed indicates that even at the lowest levels, Zn has a detrimental impact on bulk conductivity. We speculate that Zn^{2+} ions residing on the tetravalent Zr site, with effective -2 charge, act as deep proton traps, both decreasing the effective concentration of protons able to participate in the charge transport process and raising the activation energy. We note that measurements of high density (unmodified) BYZ20, discussed in Chapter 3, yield bulk conductivity values that are almost identical to those of Bohn and Schober, and thus the differences between BYZ10 and BYZ-Zn4 are not due to experimental artifacts.

A comparison of the grain boundary properties of BYZ10 and BYZ-Zn4 reveals another surprising result. In this case, there is very little difference between the two samples, despite the very high concentration of Zn in the grain boundary regions of BYZ-Zn4. The activation energies are comparable (~0.7 eV) and the preexponential terms for the total grain boundary conductivity, which include effects of both the specific grain boundary properties and the microstructure, is $\sim 10^{5.3}$. It is possible that even in nominally pure BYZ10, impurities accumulate in the grain boundary region and dominate the proton transport process, giving rise to properties that are similar to those of BYZ-Zn4. Both BYZ-Zn4 and BYZ10 are similar to gadolinium doped barium cerate [13], in that the activation energy for grain boundary transport is higher than through the bulk, and furthermore that the specific grain boundary conductivity is several orders of magnitude

lower than that of the bulk. Although the specific grain boundary conductivity of BYZ10 (nor the grain size) was not reported, it is possible to deduce this conclusion from the simple observation of a grain boundary arc [13]. In terms of the cerate, the observation of high grain boundary resistance has been explained in terms of the disruption of the perovskite structure, which is otherwise favorable to rapid proton transport, at disordered grain boundary regions. Perhaps more significantly, Figure 5.12 reveals that of the specific grain boundary conductivity of BYZ-Zn4 is lower than that of barium cerate. Thus, not only does the high concentration of grain boundaries in barium zirconate decrease total conductivity relative to the cerate, so do the inherent properties of those boundaries. Therefore, optimization of transport properties relies heavily on the ability to grow grains to moderate sizes so as to reduce total grain boundary area. Modification of BYZ with ZnO enhances grain growth and addresses precisely this challenge, although further optimization will be necessary in order to obtain total grain boundary conductivity that is greater than that of unmodified BYZ.

The results of the EMF measurements are summarized in Table 5.3. The data reveal the ion transport number of BYZ-Zn4 to be ~0.90 in the temperature range of interest, dropping slightly from 0.90 at 500 °C to 0.86 at 700 °C. By analogy to related materials [17] the balance of the charge transport can be attributed to electron hole charge carriers. With increasing temperature, both the loss of water from the structure and the higher mobility of the holes lead to a slight decrease in ionic transport number. The value shown here is somewhat higher than reported by Schober and Bohn for unmodified BYZ10 [2], who obtained ~0.8 at 700 °C for a similar but not identical EMF cell. The higher EMF values in the present work are more likely due to the more reducing conditions employed at the anode or slightly higher dopant concentration rather than to an inherent improvement in ionic transference number upon introduction of Zn. Overall, it is apparent that the ionic transport number of BYZ-Zn4 is large enough for satisfactory implementation in a fuel cell [18].

Table 5.3. Ionic transport number of BYZ-Zn4 as a function of temperature.

		T [°C]	Measured EMF [mV]	Theoretical EMF [mV]	t_{ion}
BYZ-Zn4					
Cathode	Anode				
Air-3%H_2O	H_2-3%H_2O	700	966	1120	0.86
		650	990	1128	0.88
		600	1017	1136	0.90
		550	1030	1144	0.90
		500	1037	1152	0.90

5.7 Conclusion

A homogeneous distribution of ZnO in the intergranular regions of BYZ ($BaZr_{0.85}Y_{0.15}O_3$) leads to enhanced, yet relatively uniform, grain growth of the host oxide, which, in turn, results in high densities (>93%) at reduced sintering temperatures (1300 °C). Chemical analysis by EDS methods confirmed the accumulation of Zn at the grain boundaries. In the absence of a second phase, sintering is believed to take place by enhanced solid-state diffusion, possibly due to cation vacancy formation in the intergranular regions. Despite the apparent absence of Zn from the grain interiors, the bulk conductivity of zinc oxide modified BYZ is lower than that of unmodified BYZ. At the same time, the total grain boundary conductivity appears largely unaffected by the ZnO modifier, despite the high concentration of Zn at the grain boundaries and presumably larger grain size. The reduction in bulk conductivity may be due to strong proton trapping at ZnZr” sites, which are present in levels below the EDS detection limit. Although the conductivity of ZnO modified BYZ is somewhat lower than the unmodified counterpart, the dramatic reduction in sintering temperature (from ~1600–1700 ºC), which will enable the exploration of a wider variety of potential electrode materials, renders the modified composition an attractive alternative to simple BYZ. Overall, the high total ionic conductivity, the high ionic transport number (>0.90 under fuel cell conditions) and good chemical stability, render BYZ-Zn4 a good candidate as an electrolyte in sensors and fuel cells.

5.8 References

1. K. H. Ryu and S. M. Haile. Chemical stability and proton conductivity of doped $BaCeO_3$–$BaZrO_3$ solid solutions. *Solid State Ionics* **125**, 355 (1999).

2. T. Schober andH. G. Bohn. Water vapor solubility and electrochemical characterization of the high temperature proton conductor $BaZr_{0.9}Y_{0.1}O_{2.95}$. *Solid State Ionics* **127**, 351 (2000).

3. A. Sin, B. El Montaser, and P. Odier.Synthesis and Sintering of Large Batches of Barium Zirconate Nanopowders. *J. Am. Ceram. Soc*, **85** [8], 1923 (2002).

4. G. Tagliere, M. Tersigni, P.L. Villa, and C. Mondelli. Synthesis by the citrate route and characterization of $BaZrO_3$, a high tech ceramic oxide: Preliminary results. *Inter. J. Inorg., Mater.* **1**, 103 (1999).

5. H. Iwahara, T. Yajima, T. Hibino, K. Ozaki, and H. Suzuki. Protonic conduction in calcium, strontium and barium zirconates. *Solid State Ionics* **61**, 65 (1993).

6. A. Azad, S. Subramaniam, and T. W. Dung. On the development of high density barium metazirconate ($BaZrO_3$). *J. of Alloys and Compounds* **334**, 118 (2002).

7. HSC Chemistry program (Version 5.1 Outokumpu Research Oy, Finland).

8. J. L. Pouchou and F. Pichoir, in *Quantitative analysis of homogeneous or stratified microvolumes applying the model "PAP" in Electro Probe Quantitation*, edited by K. Heinrich and D. Newbut. Plenum Press, pp. 31-75, (1991).

9. A. C. Caballero, J. F. Fernandez, C. Moure, P. Duran, and Y. M. Chiang. Grain Growth Control and Dopant Distribution in ZnO-Doped $BaTiO_3$. *J. Am. Ceram. Soc.* **81** [4], 939 (1998).

10. Y. M. Chiang, D. P. Birnie and W. D. Kingery, in *Physical Ceramics: Principles of ceramic science and engineering.* John Wiley and Sons, pp. 376 (1997).

11. R. C. T. Slade, S. D. Flint, and N. Singh. Investigation of Protonic Conduction in Yb- and Y-doped Barium Zirconates. *Solid State Ionics* **82**, 135 (1995).

12. K. D. Kreuer. Aspects of the formation and mobility of protonic charge carriers and the stability of perovskite-type oxides. *Solid State Ionics* **125**, 285 (1999).

13. S. M. Haile, D. L. West, and J. Campbell. The role of microstructure and processing on the proton conducting properties of gadolinium-doped barium cerate. *J. Mater. Res.* **13**, 1576 (1998).

14. H. G. Bohn and T. Schober. Electrical Conductivity of the High-Temperature Proton Conductor $BaZr_{0.9}Y_{0.1}O_{2.95}$. *J. Am. Ceram. Soc.* **83**, 768 (2000).

15. S.M. Haile, G. Staneff, and K.H. Ryu. Non-stoichiometry, grain boundary transport and chemical stability of proton conducting perovskites. *J. Mater. Science* **36**, 1149 (2001).

16. T. Uda, P. Babilo, and S. M. Haile. Thermodynamic Analysis and Conductivity of Yttrium Doped Barium Zirconate. Ninth International Symposium on Solid Oxide Fuel Cells, The Electrochemical Society 207 Meeting, Quebec City, Canada (2005).

17. H. Iwahara, H. Uchida, and K. Morimoto. High-Temperature Solid Electrolyte Fuel-Cells Using Perovskite-Type Oxide Based on $BaCeO_3$. *J. Appl. Electrochem.* **137**, 462 (1990).

18. T. Takahashi, K. Ito, and H. Iwahara. Efficiency of Solid-Electrolyte Fuel Cells. *Elctrochim. Acta* **12**, 21 (1967).

Chapter 6: Yttrium-doped Barium Zirconate as a Fuel Cell Electrolyte

6.1 Introduction

State-of-the-art solid oxide fuel cells (SOFCs) deliver tremendous power densities, as high as ~2 W/cm^2, but they require operation at high temperatures (typically above 800 °C for SOFCs using yttria stabilized zirconia as the electrolyte [1]). A key motivation for pursuing proton conducting perovskites is the possibility of lowering the fuel cell operating temperature to the 500–700 °C regime in order to alleviate many of the materials lifetime and cyclability challenges that result from high temperature operation. In addition, unlike oxygen conducting electrolytes, proton conducting membranes have the benefit of producing the exhaust water on the cathode side, thus avoiding the dilution of the fuel stream.

Doped barium cerate systems have been widely studied in recent years as proton conducting electrolytes for a variety of electrochemical devices including fuel cells [2–9]. A brief summary of recently reported fuel cell results are shown in Table 6.1. Cerate electrolyte thicknesses range from 0.0007 to 1.0 mm coupled with a variety of electrode materials, resulting in a wide array of measured power densities (8–1400 mW/cm^2 at 600 ºC). Among the fuel cell studies, two reports are most impressive. Hibino et al. achieved a power density of 134 mW/cm^2 at 600 ºC [6] using a novel cathode $Ba_{0.5}Pr_{0.5}CoO_3$ perovskite with an electrolyte ($BaCe_{0.75}Y_{0.25}O_3$) thickness of 0.5 mm. Iguchi et al., using yttrium doped barium cerate as an electrolyte (0.0007 mm thick), demonstrated power densities of 570 mW/cm^2 at 430 °C and 780 mW/cm^2 at 510 °C [8] under air / hydrogen conditions. In order to circumvent the detrimental reaction of barium cerate with CO_2, which would otherwise result in the formation of $BaCO_3$ and CeO_2, these authors protected the thin electrolyte by depositing it onto a dense layer of palladium foil, a well-known hydrogen separation material.

As discussed in previous chapters (Ch. 3, 4, 5), barium zirconate is stable in CO_2 containing atmospheres and fuel cells based on this electrolyte would not require elaborate

solutions for ensuring cell longevity. It should be noted that, to date, fuel cell results using a doped barium zirconate electrolyte have not been published in literature, mainly due to difficulty in processing densified high conductivity material (Chapter 3).

The development of high density and high conductivity electrolyte (unmodified BYZ, Chapter 3, and ZnO modified BYZ, Chapter 5) allows for the fabrication of electrode-membrane assemblies for electrochemical devices. In this chapter we explore ionic contribution to the total electrical transport, as well as compatibility and performance of potential electrode materials. Finally, we demonstrate the viability of doped barium zirconate as an electrolyte

Table 6.1. Summary of proton conducting electrolyte fuel cell results in literature.

electrolyte	**Cathode / Anode**	**OCV**	**Max power**	**Reference**
0.5 mm $BaCe_{0.8}Gd_{0.2}O_{2.9}$	Pt:Air / Pt:H_2 at 800 ºC	1070 mV	203 mW/cm^2	1996, N. Taniguchi [2]
1.0 mm $BaCe_{0.85}Eu_{0.15}O_{2.93}$	Pt:Air/ Pt:H_2 at 700 ºC	~690 mV	38 mW/cm^2	2006, N. Maffei [3]
0.05 mm $BaCe_{0.8}Gd_{0.2}O_{2.9}$	$La_{0.5}Sr_{0.5}CoO_3$:O_2/ Ni-BCGO: H_2 at 700 ºC	996 mV	371 mW/cm^2	2006, Q. Ma [4]
0.05 mm $BaCe_{0.9}Gd_{0.10}O_{2.95}$	Ag:O_2 / Pd:H_2 at 600 ºC	1150 mV	~12 mW/cm^2	1991, N. Bonanos [5]
0.5 mm $BaCe_{0.75}Y_{0.25}O_{2.88}$	$Ba_{0.5}Pr_{0.5}CoO_3$:Air/ Pd-FeO:H_2 at 600 ºC	~1150 mV	134 mW/cm^2	2002, T. Hibino [6]
0.5 mm $BaCe_{0.75}Y_{0.25}O_{2.88}$	Pt:Air/ Pt:H_2 at 600 ºC	~1150 mV	72 mW/cm^2	2002, T. Hibino [6]
1.0 mm $BaCe_{0.9}Y_{0.1}O_{2.95}$	Pt:Air / Pd:H_2 at 600 ºC	1100mV	~8 mW/cm^2	2003, S. Yamaguchi [7]
0.0007 mm $BaCe_{0.8}Y_{0.20}O_{2.90}$	perovskite:Air / Pd:H_2 at 600 ºC	1051 mV	1400 W/cm^2	2005, N. Ito [8]
0.05 mm $BaCe_{0.8}Gd_{0.2}O_{2.9}$	$La_{0.5}Sr_{0.5}CoO_3$:O_2/ Ni-BCGO:NH_3 at 600ºC	1102 mV	96 mW/cm^2	2006, Q. Ma [4]
0.05 mm $BaCe_{0.8}Sm_{0.2}O_{2.9}$ (BCSO)	$Ba_{0.5}Sr_{0.5}Co_{0.8}Fe_{0.2}$:$O_2$ / NiO-BCSO:H_2 at 600 ºC	1049 mV	132 mW/cm^2	2006, P. Ranran [9]

6.2 Ionic transference number of BYZ by EMF measurements

For the EMF measurement, a dense sample was affixed to the end of an alumina tube with a gas-tight ceramic paste seal (Aremco Ceramabond 552). Porous Pt electrodes were painted on both sides of the sample. Exposing one electrode surface to water saturated hydrogen and the other to water saturated compressed air (P_{H2O} = 0.03 atm) generated a voltage. The ionic transport number was estimated from the ratio of the measured potential to the calculated Nernstian (thermodynamic) value, $\langle t_{ion} \rangle = E_{meas}/E_N$, where E_N is calculated according to Eq. (6.1)

$$E_N = \frac{RT}{2F} \ln\left(\frac{P_{H_2}^{anode}}{P_{H_2}^{cathode}} \right), \tag{6.1}$$

where R is the universal gas constant, T is temperature, F is Faraday's constant and $P_{H_2}^{anode}, P_{H_2}^{cathode}$ are the partial pressures of hydrogen in the anode and cathode chambers.

The results of the EMF measurements are shown in Figure 6.1. The data reveal the ionic transport number of BYZ to be ~0.92 (or greater if one accounts for nonideal activity of the electrodes and imperfect seal) in the temperature range of interest, dropping slightly from 0.92 at 500 °C to 0.88 at 700 °C. The results are slightly higher compared to Schober and Bohn who reported an ionic transference number of approximately 0.8 at 700 °C under somewhat more oxidizing conditions [10]. The balance of the charge transport can be attributed to p-type electronic carriers (holes).

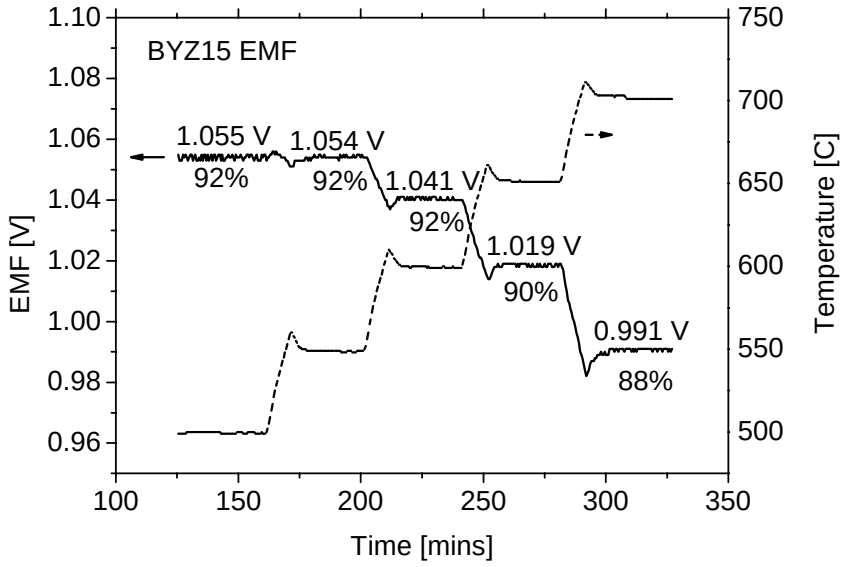

Figure 6.1. EMF results for BYZ under water saturated hydrogen and water saturated air gradient.

The electronic hole contribution of the electrolyte can be independently confirmed with impedance spectroscopy. Impedance measurements of a typical cell with Pt electrodes in varying oxygen partial pressure (water saturated) are shown in Figure 6.2. The performance of the electrolyte in H_2, Air and O_2 are 0.0024 S/cm, 0.0027 S/cm, and 0.0033 S/cm, respectively. The area specific resistance shifts to lower resistances with increasing oxygen partial pressure, which can be explained with the creation of (electron) holes as depicted in Eq. (6.2) below.

$$\frac{1}{2}O_2 + V_O^{\bullet\bullet} \rightarrow O_O^x + 2h^{\bullet} \tag{6.2}$$

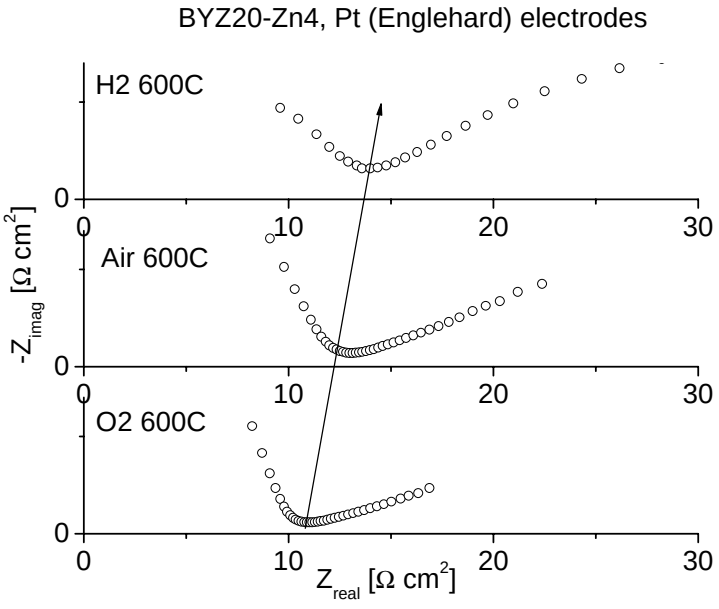

Figure 6.2. Impedance of BYZ electrolyte shifts to lower resistance with higher P_{O2}.

With increasing temperature, both the loss of protons from the structure and the higher mobility of holes lead to a slight decrease in the ionic transport number. While a pure ionic conductor is most desirable (t_{ion} = 1), the electronic resistivity of BYZ is sufficiently high for implementation of this material as a fuel cell electrolyte.

6.3 Evaluation of Electrode Materials for the BYZ Fuel Cell

6.3.1 Transition-metal Electrodes

Electrolyte supported symmetric cells (same electrode on both sides and under uniform atmosphere) were tested to evaluate the performance of metal electrodes. The electrode studies were conducted using the BYZ20-Zn4 electrolyte due to the ease in processing and fabrication as compared to the unmodified BYZ20 (discussed in Chapter 5). A summary of symmetric cell measurements (from the same batch of electrolyte material with similar thickness and surface area) under oxygen is presented in Figure 6.3, clearly showing an activity trend of Pt > Ag > Pd.

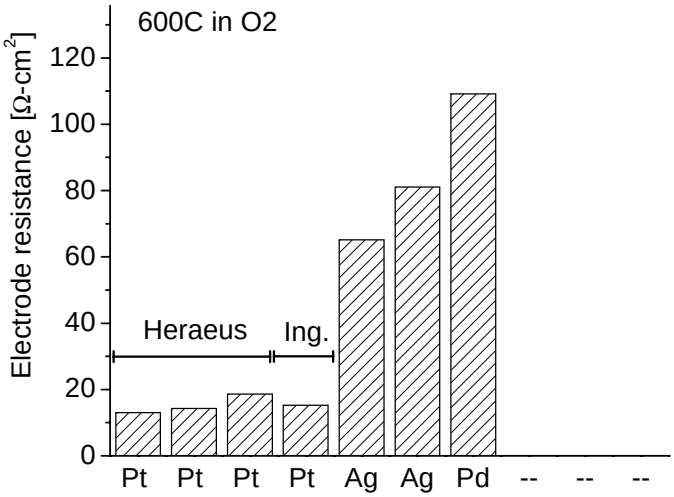

Figure 6.3. Summary of electrode resistances in humidified oxygen at 600 ºC (as measured by impedance spectroscopy under symmetric cell oxygen conditions).

It was suspected that microstructural differences may be responsible for some of the differences in catalytic activity of the electrode metals. The surface of the silver electrode, as imaged by scanning electron microscopy, Figure 6.4 a, is highly densified resulting in an undesirable structure with few triple phase boundaries and presumably high resistance to gas transport. The surface electron image of the platinum ink (Figure 6.4 b, 6.4 c), in contrast, shows more porosity and a thoroughly connected network.

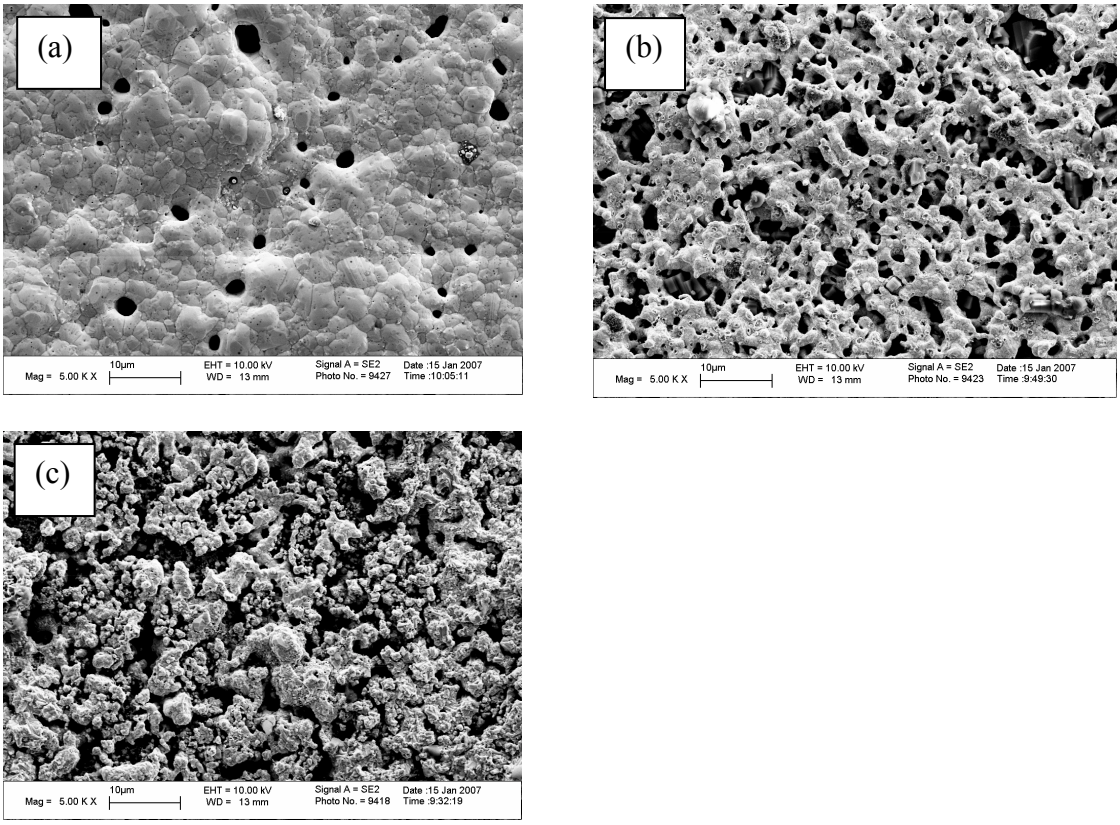

Figure 6.4. SEM images of electrode surfaces (a) Ag, (b) Pt-Heraeus, and (c) Pt- Engelhard.

The poor performance of the palladium metal catalyst is attributed to the oxidation of Pd in the cathode chamber. Formation of PdO is thermodynamically favored under pure oxygen at temperatures below ~ 680 ºC [11], Figure 6.5.

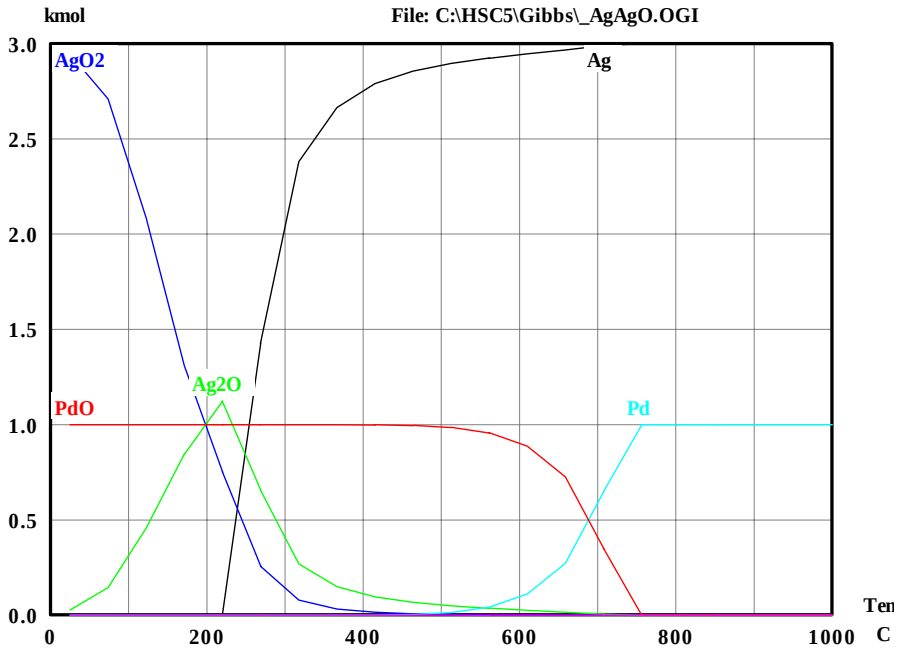

Figure 6.5. Thermodynamic calculation of oxidation stability of Ag and Pd metals.

6.3.2 Metal Electrode Performance under Varying Oxygen Partial Pressures

A remarkable characteristic of the Pt|BYZ20|Pt cells is the much lower electrode resistances under oxygen than under hydrogen atmospheres, Figure 6.6. With both platinum and silver electrodes on a BYZ-Zn4 electrolyte, the total resistance (electrolyte plus both electrodes) of the cell is 2–3 times larger under hydrogen as opposed to oxygen. The increased electronic conductivity under oxidizing conditions (enhanced p-type conductivity) in the BYZ electrolyte is believed to lead to enhancement in the oxygen electroreduction rates.

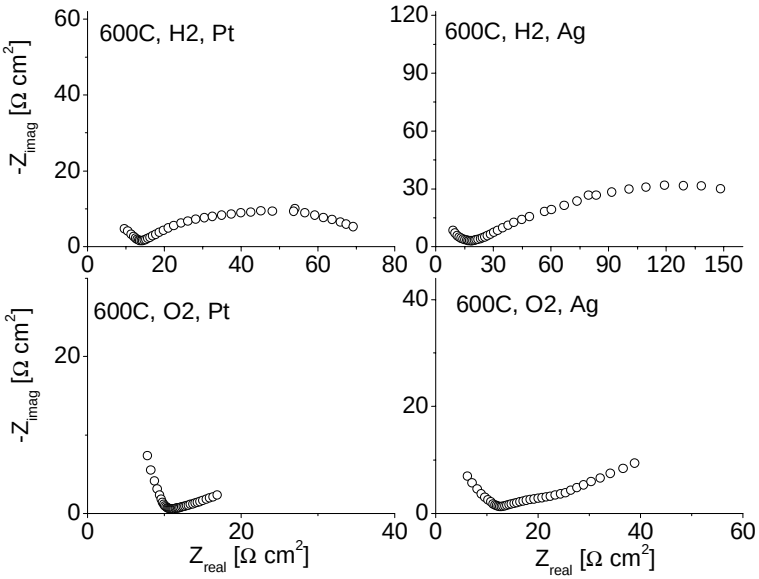

Figure 6.6. Comparison of electrode (Pt and Ag) performance under symmetric cell oxygen and hydrogen gases.

To further probe the hypothesis of electron-hole modulation of oxygen electroreduction, symmetric cell impedance measurements were carried out at lower temperatures at which hole concentrations become negligible. The results are summarized in Table 6.2. The independence of the electrolyte resistance to oxygen partial pressure at 500 and 400 ºC confirms that hole contributions to the conductivity are negligible at these temperatures. Furthermore, while the difference in electrode behavior in H_2 and in O_2 are not as stark as in some other samples, it is clear that the cathode kinetics slow down much more dramatically at low temperature than the kinetics at the anode, consistent with the hypothesis that electronic holes play a major role in oxygen electroreduction at high temperatures.

Table 6.2. Summary of electrode area specific resistances of BYZ20-Zn4 with Pt (Heraeus) electrodes in the temperature range of 400-600ºC for O_2 and H_2 atmospheres.

	O_2,		**H_2,**	
	electrodes, Ω-cm^2	electrolyte, Ω-cm^2	electrodes, Ω-cm^2	electrolyte, Ω-cm^2
600ºC	13	6	21	9
500ºC	92.5	17.5	53	18
400ºC	1922	50	285	50

To exclude possible reactions between Pt and BYZ under hydrogen atmosphere that would result in decreased catalytic activity, cell atmosphere was varied from $O_2 \rightarrow H_2 \rightarrow O_2$. Experiments illustrated the reversibility of the enhanced Pt activity under oxidizing conditions, Figure 6.7. Both the total electrolyte and total electrodes had superior performance under an oxygen atmosphere after cycling through 8 hrs of reducing conditions. Further, possible reaction products of the Pt and BYZ system were not observed under SEM.

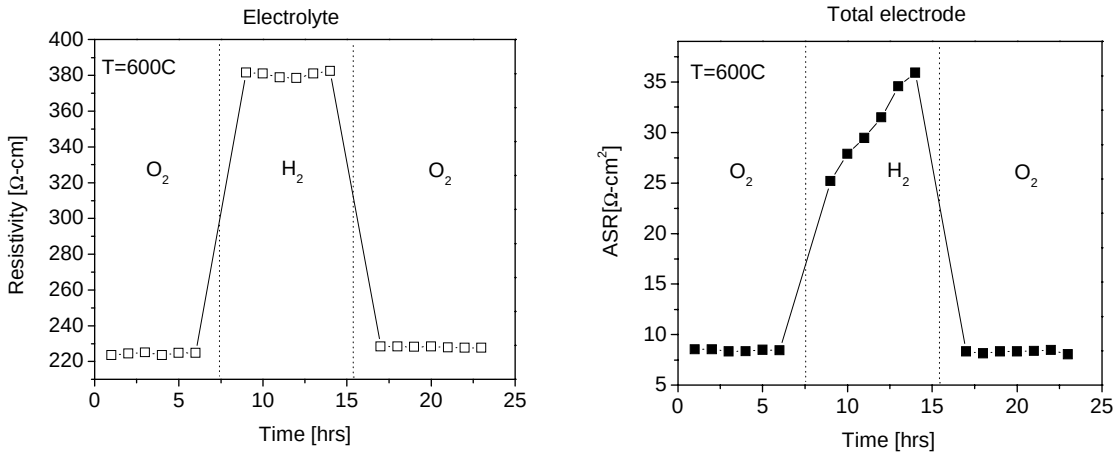

Figure 6.7. BYZ20 electrolyte (a) and Pt total electrode (b) resistances over 24 hrs with varying symmetric gas from oxygen to hydrogen and back to oxygen at 600 ºC.

6.3.3 Novel Perovskite Cathodes

Several potential cathode materials for the doped barium zirconate system were synthesized via the glycine nitrate combustion method. Based on initial screening, the following cathodes were synthesized: $BaZr_{0.40}Pr_{0.40}Gd_{0.20}O_3$, $BaZr_{0.70}Pr_{0.10}Gd_{0.20}O_3$, $BaZr_{0.80}Co_{0.20}O_3$, $BaZr_{0.60}Y_{0.20}Co_{0.20}O_3$ and $BaPr_{0.85}Y_{0.15}O_3$. All formed single phase perovskites as determined by X-ray power diffraction, Figure 6.8, except for Pr-rich compound, $BaPr_{0.85}Y_{0.15}O_3$, that proved to be unstable with time and was not considered further.

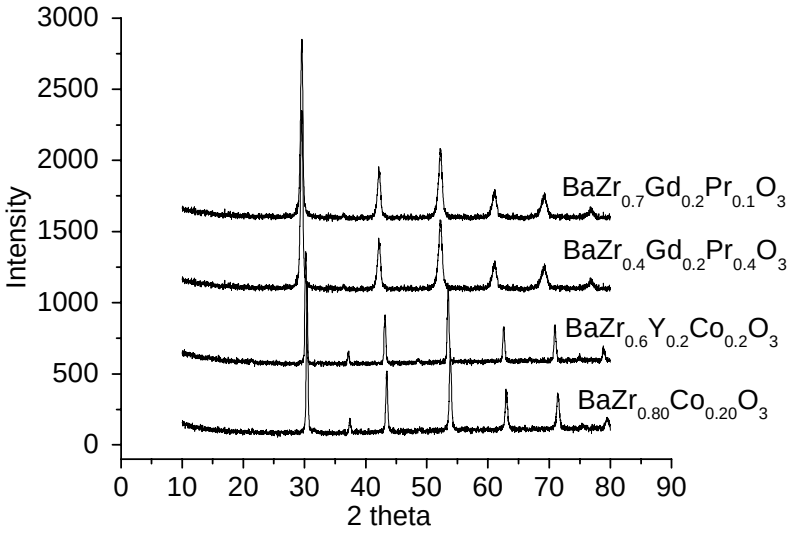

Figure 6.8 Powder x-ray of potential cathode materials

Potential cathodes were mixed with $BaZ_{r0.85}Y_{0.15}O_3$ (BYZ15) and calcined at 700 °C (maximum fuel cell operating temperature) for 24 hrs to observe the possibility of a reaction or inter-diffusion of species. Under these conditions, $BaZr_{0.70}Pr_{0.10}Gd_{0.20}O_3$ and $BaZr_{0.80}Co_{0.20}O_3$ reacted with BYZ to yield a single, solid-solution perovskite phase and were not considered further. In contrast, mixtures of $BaZr_{0.40}Pr_{0.40}Gd_{0.20}O_3$ with BYZ and of $BaZr_{0.60}Y_{0.20}Co_{0.20}O_3$ with BYZ retained two perovskite phases, Figure 6.9, although the possibility of slight interdiffusion cannot be entirely ruled out.

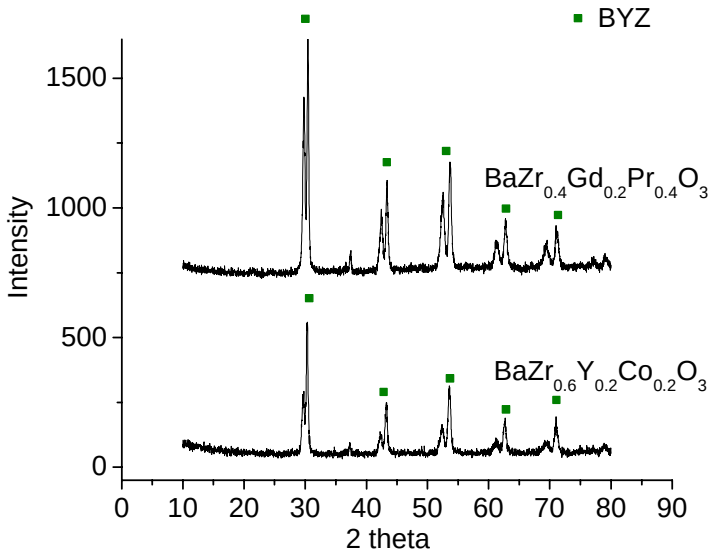

Figure 6.9. Diffraction patterns obtained from mixtures of (a) BYZ + $BaZr_{0.60}Y_{0.20}Co_{0.20}O_3$ and (b) BYZ + $BaZr_{0.40}Pr_{0.40}Gd_{0.20}O_3$, after exposure to 700 °C for 24 hrs showing that two separate perovskite phases are retained.

The bulk conductivities of $BaZr_{0.40}Pr_{0.40}Gd_{0.20}O_3$ and $BaZr_{0.60}Y_{0.20}Co_{0.20}O_3$ were measured by AC impedance methods in a wet air atmosphere, Figure 6.10. Both potential cathode materials have comparable conductivity values as BYZ in the temperature region of interest.

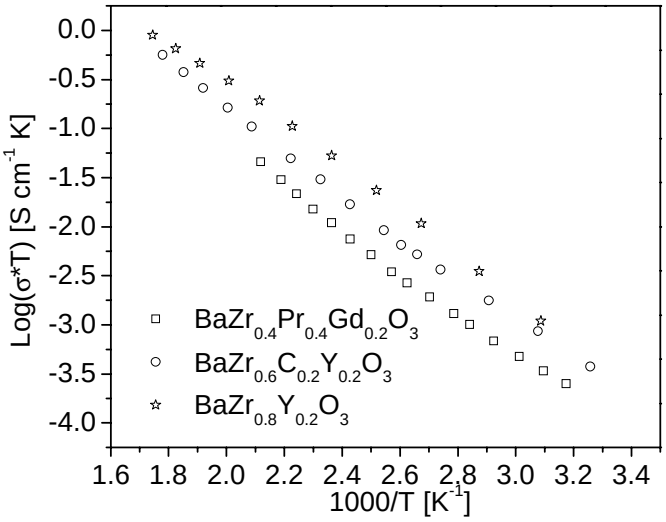

Figure 6.10. Bulk conductivity of two potential cathode materials as measured in wet-air atmosphere compared to BYZ20.

Surprisingly the activation energy of $BaZr_{0.40}Pr_{0.40}Gd_{0.20}O_3$ and $BaZr_{0.60}Y_{0.20}Co_{0.20}O_3$ was measured as 0.40eV and 0.42eV, respectively. These values are similar to the value of 0.47eV that Babilo et al. reported for BYZ20 bulk conductivity [12]. The additions of transition metals were expected to increase electronic conductivity of the samples resulting in significantly lower activation energies.

Of the five potential cathode materials examined $BaZr_{0.40}Pr_{0.40}Gd_{0.20}O_3$ and $BaZr_{0.60}Y_{0.20}Co_{0.20}O_3$ proved to be the most promising. However, the possibility that better materials exist has hardly been ruled and additional screening continues.

6.4 Yttrium-doped barium zirconate fuel cell demonstration

From the many Pt|BYZ20|Pt fuel cells tested, three electrolyte supported cells are evaluated and summarized in this section. The cell electrolyte thickness, stoichiometry, electrode material, open circuit voltage (OCV), and maximum power densities are summarized in Table 6.3. In all cases, inlet gases (O_2, air, H_2) were humidified to p_{H2O} = 0.03 atm.

Table 6.3 Summary of three Pt | BYZ20 | Pt fuel cells investigated

	stoichiometry	**Sintering conditions**	**electrodes**	**Thickness [cm]**	**OCV [mV]**	**Power density [mW/cm^2]**
Sample 1	BYZ20	1600ºC, 24 hrs	Pt (Heraeus)	0.024	960	25.3
Sample 2	BYZ20	1600ºC, 24 hrs	Pt (Heraeus)	0.032	1036	42.9
Sample 3	BYZ20	1600ºC, 8 hrs	Pt (Heraeus)	0.025	665	18.4

6.4.1 Sample 1- H_2 : Pt | BYZ20 (240 μm thick) | Pt : O_2

Polarization curves obtained from Pt | BYZ20 | Pt cell are presented in Figure 6.11. The maximum (or limiting) current and peak power density at 600 °C with oxygen supplied to the cathode and hydrogen to the anode were 92 mA/cm^2 and 25.3 mW/cm^2, respectively. The fuel cell polarization curves are extremely linear and thus it is possible to evaluate the slopes in order to assess the sources of polarization losses. At 600 °C, the polarization slope was calculated to be 10.1 Ω-cm^2.

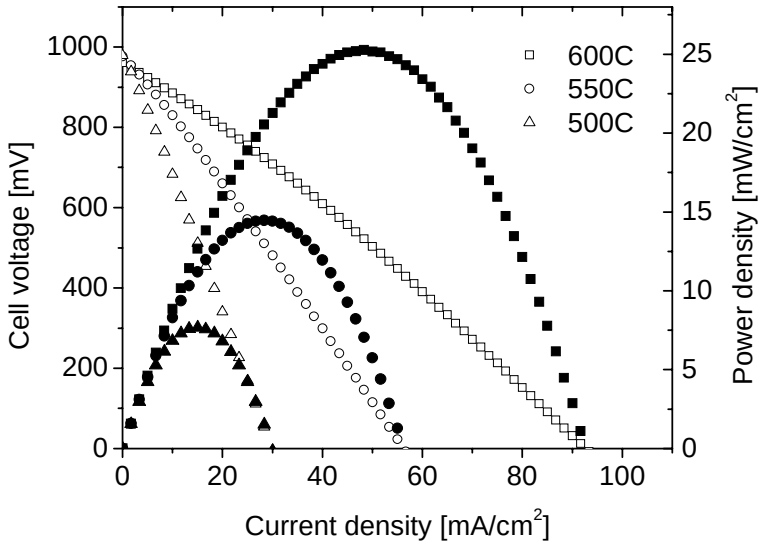

Figure 6.11. Polarization and power density curves at 600, 550 and 500ºC for H_2:Pt|BYZ20 (240 μm)|Pt:O_2.

The area specific resistances of the cell under a uniform gas atmosphere as well as under fuel cell conditions (H_2 partial pressure gradient), are measured by impedance spectroscopy for this particular cell, Figure 6.12, and are summarized in Table 6.4. In the case of impedance measurements under a H_2 partial pressure gradient, in conjunction with the impedance analyzer, a galvanostat was used to maintain zero current across the cell at OCV. The electrodes appear to contribute (2.8 + 10.8) / 2 = 6.8 Ω-cm^2 of resistance whereas the electrolyte appears to contribute ~ (4.1 + 7.2) / 2 = 5.65 Ω-cm^2 of resistance. The total, 12.45 Ω-cm^2 is slightly larger than the 10.1 Ω-cm^2 obtained from directly evaluating the slope of the polarization curve. Impedance evaluation under fuel cell condition results in an electrode contribution of 6.7 Ω-cm^2, which is comparable to 6.8 Ω-cm^2 averaged over O_2 and H_2 under symmetric cell conditions. Electrolyte contribution, under fuel cell, is 3.0 Ω-cm^2, 2.65 Ω-cm^2 smaller than the value obtained from symmetric cell measurements. This 2.65 Ω-cm^2 may account for the discrepancy between the

total resistance as calculated by symmetric cell measurement (6.8 + 5.65 = 12.45 Ω-cm^2) and the polarization slope (10.1 Ω-cm^2).

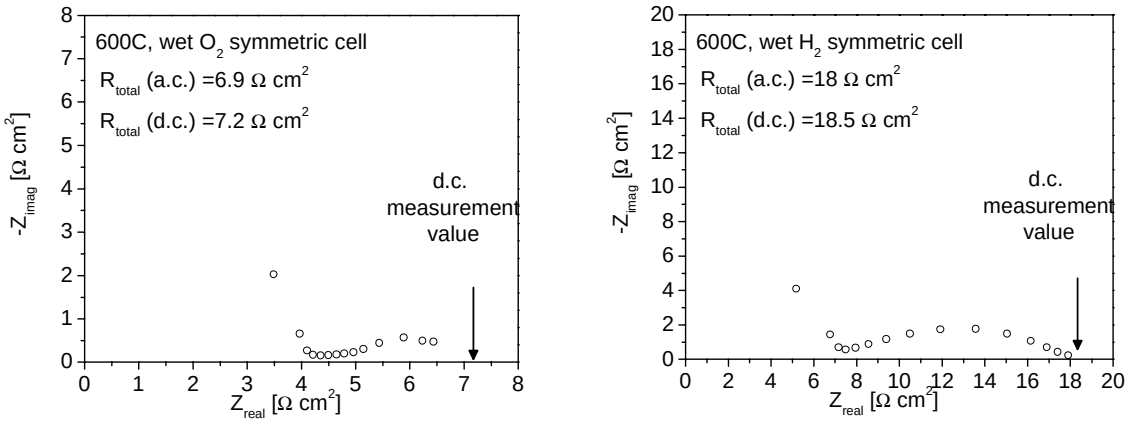

Figure 6.12. Symmetric cell measurements at 600 ºC under water saturated (a) oxygen and (b) hydrogen. D.C. measurements also shown for comparison (Pt electrodes).

The conductivities of the electrolyte under O_2, H_2 and fuel cell conditions are 0.00585, 0.0033, and 0.008 S/cm, respectively. These values are fairly reasonable compared to the values shown in Chapter 3. Total area specific resistance as determined by D.C. measurements under symmetric cell conditions, Figure 6.12, are analogous to the total determined with impedance studies. The advantage of the impedance measurement is the contributions of the electrolyte and electrode resistances to the total can be obtained as opposed to only the total resistance with D.C. measurements.

Table 6.4. Summary of impedance measurements under O_2, H_2 and fuel cell conditions.

	Impedance, O_2		**Impedance , H_2**		**Impedance, Fuel cell**	
	electrodes, Ω-cm^2	electrolyte, Ω-cm^2	electrodes, Ω-cm^2	electrolyte, Ω-cm^2	electrodes, Ω-cm^2	electrolyte, Ω-cm^2
Sample 1	2.8	4.1	10.8	7.2	6.7	3.0

6.4.2 Sample 2- H_2 : Pt | BYZ20 (320 μm thick) | Pt : (O_2 or Air)

The power output is higher when oxygen is supplied to the cathode than when air is the inlet cathode gas. A summary of the fuel cell characteristics under both atmospheres is provided in Table 6.5. In agreement with the EMF results, the measured OCV is just slightly below the Nernstian value (1036 mV compared to theoretical value of 1165 mV) and the ratio between the measured and theoretical values decreases with increasing temperature and also with increasing oxygen partial pressure at the cathode. This result again reflects the greater extent of p-type electronic conductivity under high temperatures and oxidizing atmospheres. The maximum (or limiting) current and peak power density at 600 °C with oxygen supplied to the cathode were 155 mA/cm^2 and 42.9 mW/cm^2, respectively. While these values are not competitive with state-of-art fuel cells, they are the highest reported in the open literature for fuel cells based on doped barium zirconate.

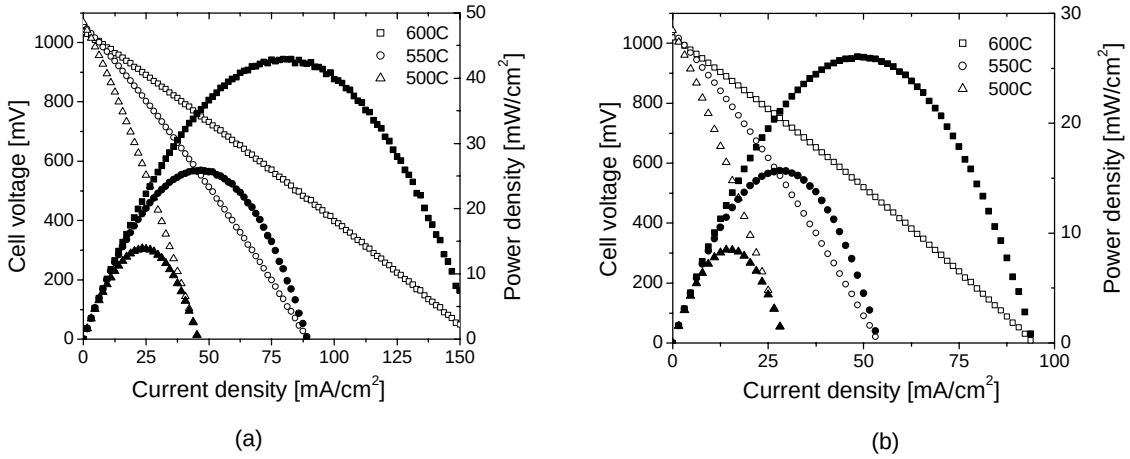

Figure 6.13. Polarization and power density curves when the cathode is supplied with (a) oxygen and (b) air for 320 μm BYZ20 cell with Pt electrodes.

A notable characteristic of the Pt | BYZ20 | Pt fuel cells is the much lower polarization slope under oxygen than under air. The increased electronic conductivity under oxidizing conditions is responsible for a small part of this (in the simplest case, the slope is the total of the electronic and ionic resistances summed in parallel), but cannot explain a decrease in the overall area specific polarization resistance by about 60% in switching from air to oxygen atmospheres. While a detailed investigation is required to fully understand the origins of this behavior, we hypothesize that the effect arises from differences in electrocatalysis rates at the cathode. As discussed in previous sections, the enhanced p-type conductivity in the BYZ electrolyte under oxidizing atmospheres leads to enhanced rates of oxygen electroreduction. Analogous behavior has been observed in acceptor doped ceria, with anode electrocatalysis rates exhibiting temperature and oxygen partial pressure dependences similar to those of the n-type conductivity in the mixed conducting electrolyte [13].

Table 6.5. Open circuit voltages (OCV) and polarization slopes for O_2-Pt|BYZ20|Pt-H_2 and Air-Pt|BYZ20|Pt-H_2 systems.

	OCV, O_2 [mV]	Theoretical voltage [mV]	Polarization slope, O_2	OCV, Air [mV]	Theoretical voltage [mV]	Polarization slope, Air
600ºC	1036	1165	6.7	1020	1136	10.8
550ºC	1060	1171	11.9	1039	1144	19.2
500ºC	1068	1178	23.4	1043	1152	35.8

6.4.3 Sample 3- H_2 : Pt | BYZ20 (250 μm thick) | Pt : O_2

Compared to previously shown voltage current (VI) curves, Figure 6.14 has a higher noise to signal ratio. Scatter in the polarization curve is indicative of gas leakage across the cell, which is confirmed by the low OCV of 665 mV. With a polarization slope of 6.3 Ω-cm^2, a peak power density of 18.4 mW/cm^2 is achieved.

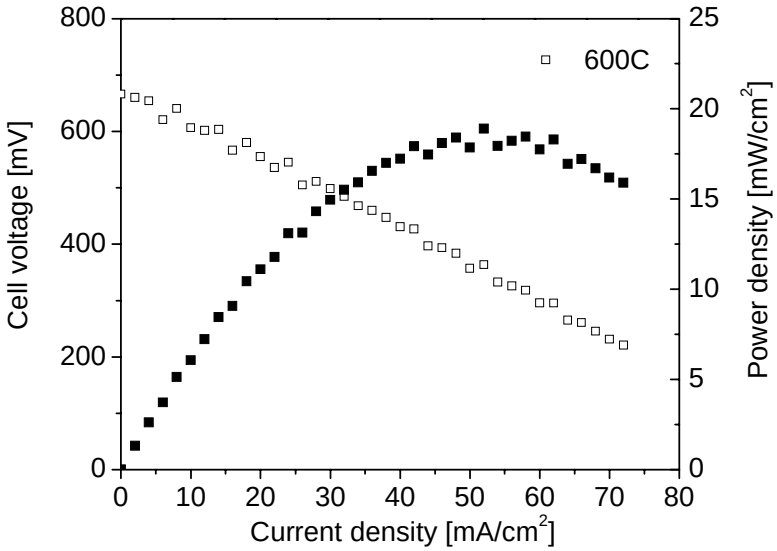

Figure 6.14. Polarization and power density of 250 μm thick BYZ20 cell with Pt electrodes at 600 ºC.

Impedance measurements under symmetric cell measurements indicate an electrode contribution of 3.8 Ω-cm^2, which is again comparable to the 3.1 Ω-cm^2 measured under fuel cell conditions. Total cell resistance under symmetric cell of 8.1 Ω-cm^2 is slightly larger than the slope of the polarization curve, 6.3 ohm-cm^2. The inconsistency arises from the fact that under fuel cell condition, the electrolyte contribution is lower than those measured under both oxygen and hydrogen symmetric cell conditions, Table 6.6. While the reasons for the 'apparent' higher electrolyte conductivity under fuel cell conditions remain to be elucidated, it is possible that such a phenomenon is the cause for disagreement between uniform atmosphere symmetric cell measurements and fuel cell condition measurements. Detailed investigation is required to fully understand the origins of this behavior.

Table 6.6. Impedance measurements under O_2, H_2, and fuel cell conditions.

	Impedance, O_2		**Impedance, H_2**		**Impedance, Fuel cell**	
	electrodes, Ω-cm^2	electrolyte, Ω-cm^2	electrodes, Ω-cm^2	electrolyte, Ω-cm^2	electrodes, Ω-cm^2	electrolyte, Ω-cm^2
Sample 3	1.7	3.5	5.9	5.1	3.1	2.5

To compare and validate the equivalency of A.C. impedance and D.C. measurements, under fuel cell conditions a D.C bias was applied while completing A.C. impedance measurements, Figure 6.15 a. A galvanostat was utilized in applying and maintaining the appropriate D.C. bias while impedance response analyzer swept through the proper frequency ranges with a given perturbation amplitude. As the current drawn increases, the mass transfer contribution (third arc in the impedance) increases, Figure 6.15 a. Integrating a polynomial function of the applied current and measured resistances, the polarization curve can be calculated, Figure 6.15 b.

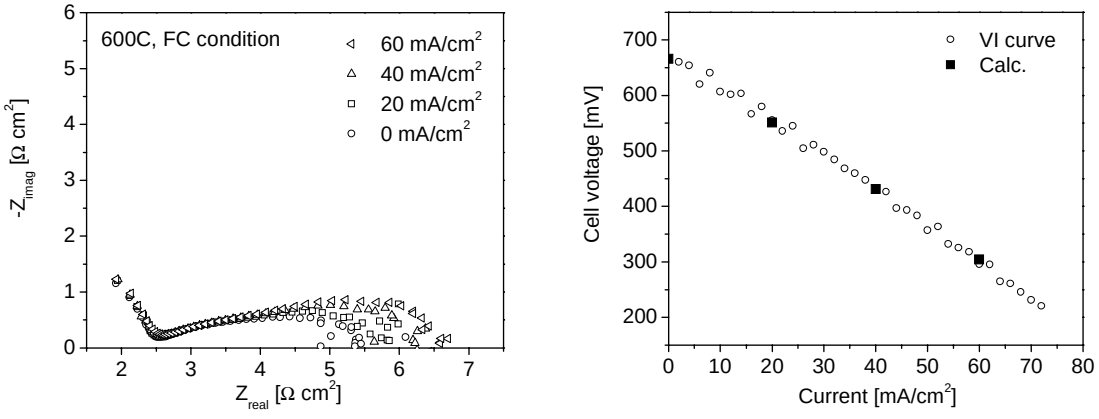

Figure 6.15. Impedance measurements under fuel cell condition with applied d.c. current (a) and calculated versus experimental polarization curve (b).

6.5 Conclusions

With an ionic transport number greater than 0.92 under fuel cell conditions in the temperature region of interest, barium zirconate is viable as an electrolyte in sensor and fuel cell applications.

Potential metal electrodes were tested and an activity trend of Pt > Ag > Pd was revealed. Pd electrodes proved to oxidize below 680 ºC under pure oxygen atmosphere inhibiting their use in the cathode chamber. Several potential mixed conducting (proton and electron) cathode materials were examined, concluding $BaZr_{0.40}Pr_{0.40}Gd_{0.20}O_3$ and $BaZr_{0.60}Y_{0.20}Co_{0.20}O_3$ to be the most promising in terms of both conductivity and stability.

Interesting result arose in the electrode behavior under varying oxygen partial pressure. The cathode activity of a proton conducting perovskite based fuel cells is higher than that of the anode. This unusual result is tentatively assigned to the electronic (hole) conductivity of BYZ under oxidizing conditions and suggests methods for further enhancing electrochemical activity.

Doped barium zirconate was shown a viable fuel cell electrolyte; a fuel cell based on this material and supplied with humidified hydrogen to the anode and humidified oxygen supplied to the cathode exhibited a short circuit current density of 155 mA/cm^2 and peak power density of 43 mW/cm^2 at 600 °C.

To compete with the 2 W/cm^2 of power output possible from conventional SOFCs, improvements in both the conductivity of BYZ and the electrocatalysis rates at its electrodes are required. Attaining these improvements by optimizing the doping concentration (as discussed in Chapter 4), enhancing grain growth (Chapter 4 & 5), and exploring alternative electrocatalysts will undoubtedly require substantial efforts.

6.6 References

1. S. M. Haile. Fuel Cell Materials and Components. *Acta Mater.* **51**, 5981 (2003).

2. N. Taniguchi, E. Yasumoto, and T. Gamo. Operating Properties of Solid Oxide Fuel Cells Using BaCe0.8Gd0.3O3 Electrolyte. *J. Electrochem. Soc.* **143**, 1886 (1996).

3. N. Maffei, L. Pelletier, J.P. Charland, and A. McFarlan. An ammonia fuel cell using mixed ionic and electronic conducting electrolyte. *J. Power Source* **162**, 165 (2006).

4. Q. Ma, R. Peng, Y. Lin, J. Gao, and G. Meng. A high-performance ammonia-fueled solid oxide fuel cell. *J. Power Source* **161**, 95 (2006).

5. N. Bonanos, B. Ellis, and M. N. Mahmood. Construction and operation of fuel cells based on the solid electrolyte $BaCeO_3$:Gd. *Solid State Ionics* **44**, 305 (1991).

6. T. Hibino, A. Hashimoto, M. Suzuki, and M. Sano. A solid oxide fuel cell using Y-doped BaCeO3 with Pf-Loaded FeO anode and $Ba_{0.5}Pr_{0.5}CoO_3$ cathode at low temperatures. *J. Electrochem. Soc.* **149**, A1503 (2002).

7. S. Yamaguchi, T. Shishdo, H. Yagami, S. Yamamoto, and S. Hara. Construction of fuel cells based on thin proton conducting oxide electrolyte and hydrogen-permeable metal membrane electrodes. *Solid State Ionics* **163-163**, 291 (2003).

8. N. Ito, M. Iijima, K. Kimura, and S. Iguchi. New intermediate temperature fuel cell with ultra-thin proton conductor electrolyte. *J. Power Sources* **152,** 200 (2005).

9. P. Ranran, W. Yan, Y. Lizhai, and M. Zongqiang. Electrochemical properties of intermediate-temperature SODCs based on proton conducting Sm-doped BaCeO3 electrolyte thin film. *Solid state Ionics* **177**, 389 (2006).

10. T. Schober and H. G. Bohn. Water vapor solubility and electrochemical characterization of the high temperature proton conductor $BaZr_{0.9}Y_{0.1}O_{2.95}$. *Solid State Ionics* **127,** 351 (2000).

11. Calculated using a Gibbs energy minimization method as implemented in the commercial software package HSC (Version 5.1, Outokumpo Research Oy, Finland).

12. P. Babilo, T. Uda, and S. M. Haile. Processing of yttrium doped barium zirconate for high proton conductivity. *J. Materials Research* (in press 2007).

13. W. Lai and S.M. Haile. Impedance spectroscopy as a tool for chemical and electrochemical analysis of mixed conductors: a case study of ceria. *J. American Ceramic Soc.* **88,** 2979 (2005).

Chapter 7: Conclusions and Plans for Future Investigations

7.1 Main conclusions and summary

The refractory nature of doped barium zirconate leads to significant challenges in its processing and characterization. The difficulty in readily processing a high density (>93%), high conductivity sample in conjunction with early misinterpretation of electrical data resulted in wide range of reported protonic conductivities in literature. The causes responsible for this poor reproducibility were explored. Using the proper processing methodology allows for consistently obtaining high density, high conductivity barium zirconate with transport properties comparable to the best values reported in the literature. Specifically, small initial particle size (50–100 nm), use of a organic binder, and high temperature sintering (1600 °C) in the presence of excess barium, so as to avoid barium loss, were essential. The total conductivity (contributions of both the bulk and grain boundary regions) of $BaZr_{0.8}Y_{0.2}O_{3-\delta}$ at 600 °C under humidified nitrogen (P_{H2O}= 0.031 atm) is 7.9×10^{-3} S/cm. In the absence of excess barium, the high temperature sintering conditions required to achieve good densification of barium zirconate induces measurable changes in stoichiometry and dramatic reduction in proton conductivity. Barium deficiency was shown to lower the conductivity by two orders of magnitude and it is believed that stoichiometry differences induced by severe processing conditions (sintering and milling) are the major contributors to the wide variation in literature data.

The ability to obtain high density, reproducible samples allowed for the further characterization and optimization of the grain boundaries. Total conductivity of doped barium zirconate can be improved through the control of its microstructure. Elongated sintering time resulted in grain growth, decreasing the grain boundary density. This was clearly shown to have beneficial effects on the total conductivity. In addition, the intrinsic properties of the grain boundary showed improvement with increased sintering times due to systematic decrease in both the grain boundary thickness and space charge potential with increasing sintering times.

Further, consistently producing reproducible doped barium zirconate permitted the investigation of dopant concentration's influence on the stability, proton solubility, and proton mobility. The lattice constant was shown to linearly increase with increasing dopant concentration, indicating the solubility of up to 40 mol % Y in the barium zirconate system. The highly doped (20–40 mol %) systems proved to be stable in aggressive environments. Samples prepared with 20, 30, and 40 mol % Y were fully protonated (up to the theoretical saturation limit) at room temperature. The hydration enthalpies and entropies were independent of dopant concentration due to the similar electron density of the oxygen ion (basicity) coordinated with the Y and Zr. Significant hydroxyl-dopant association were observed at higher dopant concentrations (40 mol %). As associations become more pronounced with increasing Y dopant, the bulk conductivity decreased (especially at lower temperatures) and total enthalpy (migration and association) increased.

To simplify the processing conditions needed to produce high density barium zirconate, transition metals as sintering aids were explored. A homogeneous distribution of 4 mol % ZnO in the intergranular regions of BYZ15 ($BaZr_{0.85}Y_{0.15}O_{3-\delta}$) led to enhanced sintering, which resulted in high sample densities greater than 93% (of theoretical) at a significantly reduced sintering temperatures of 1300 °C. Although the conductivity of ZnO modified BYZ was slightly lower than the unmodified counterpart, the high ionic transport number (>0.90 under fuel cell conditions), good chemical stability, and dramatic reduction in sintering temperature (from 1600 ^{o}C) render BYZ-Zn4 a good alternative for BYZ. Such advances in sintering temperature will enable the exploration of a wider variety of potential electrode materials, as well as development of advanced fabrication techniques for thin films.

Advances in processing (with and without sintering aids) allowed for fabrication of densified membranes, which are essential for electrochemical applications. With an ionic transport number greater than 0.92 under fuel cell conditions in the temperature region of interest,

barium zirconate is viable as an electrolyte in sensor and fuel cell applications. A fuel cell based on this material and supplied with humidified hydrogen to the anode and humidified oxygen supplied to the cathode exhibited a short circuit current density of 155 mA/cm^2 and peak power density of 43 mW/cm^2 at 600 °C. Investigations of electrode behavior under varying oxygen partial pressure found the polarization losses of the cathode was lowers than that of the anode. The enhanced electroreduction of the cathode is tentatively assigned to the electronic (hole) conductivity of BYZ under oxidizing conditions and suggests methods for further enhancing electrochemical activity.

7.2 Recommendation for future investigations

7.2.1 Electrode performance under varying oxygen partial pressure

Preliminary investigations, as discussed in Chapter 6, illustrate the enhanced electro-reduction catalysis on the cathode with increasing oxygen partial pressure. Investigation of the electrode conductivity will yield a power law dependence on oxygen partial pressure. This data combined with already established date for BYZ, will help postulate the electrochemical activity of BYZ for oxygen reduction.

7.2.2 Detailed investigation of mixed conducting perovskites for cathode materials

Further examination of the perovskite cathode is necessary to properly establish high performing cathode for proton conductors. Superior cathode electrodes require significant proton conductivity, electronic conductivity, and high electroreduction rates. In conjunction with a BYZ electrolyte, symmetric cell testing of the cathode materials in an oxidizing atmosphere should yield valuable information regarding catalytic activity for oxygen reduction and simultaneous proton transport.

7.2.3 Fabrication of thin film BYZ fuel cells

In the development of proton conducting doped barium zirconate thin film electrolyte for fuel cell applications, elaborate multi-structured systems are needed. The electrode supported single cell design enables to reduce the electrolyte thickness and hence decrease the cell internal resistance. Fabrication of these bi-layer BYZ structures with varying porosity will require substantial efforts to optimization starting powders with proper manufacturing processes. Figure 7.1 is a SEM micrographs of such system. The support is a porous BYZ layer (~700 μm) while the electrolyte is a fully densified layer (100 μm). Future plans include utilizing impregnation techniques to incorporate metal catalysts into the porous layer.

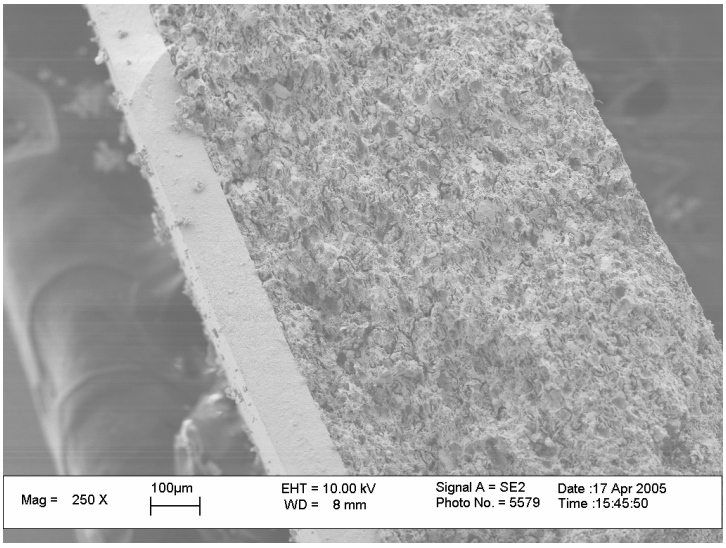

Figure 7.1. Cross-section of 100 µm electrolyte BYZ membrane on BYZ porous support.

7.2.4 Co-firing electrode supported thin film BYZ-Zn4 cells

Fabrication of cathode-supported cells (porous cathode with a dense thin electrolyte) is also under development. Such structures are beneficial and are implemented because the cathode overpotential is lower than that of the anode at 600 ºC. Our development of highly sinterable BYZ via the introduction of 4 mole % Zn (BYZ-Zn4) has made it possible to pursue cathode supported fuel cells. Fabrication methods to date have involved dual pressing, in which a thick cathode layer is uniaxially pressed and a thin electrolyte layer deposited atop this layer and the two layers pressed together (again, uniaxially), and sintered. Figure 7.2 shows a BYZ-Zn4 electrolyte on a $BaZr_{0.40}Pr_{0.40}Gd_{0.20}O_3$ cathode support. The electrolyte is approximately 40–50 µm thick; however, it is not yet fully densified. Further optimization of the co-sintering temperature is needed to develop a thin dense electrolyte on a cathode supported MEA (membrane-electrode assembly).

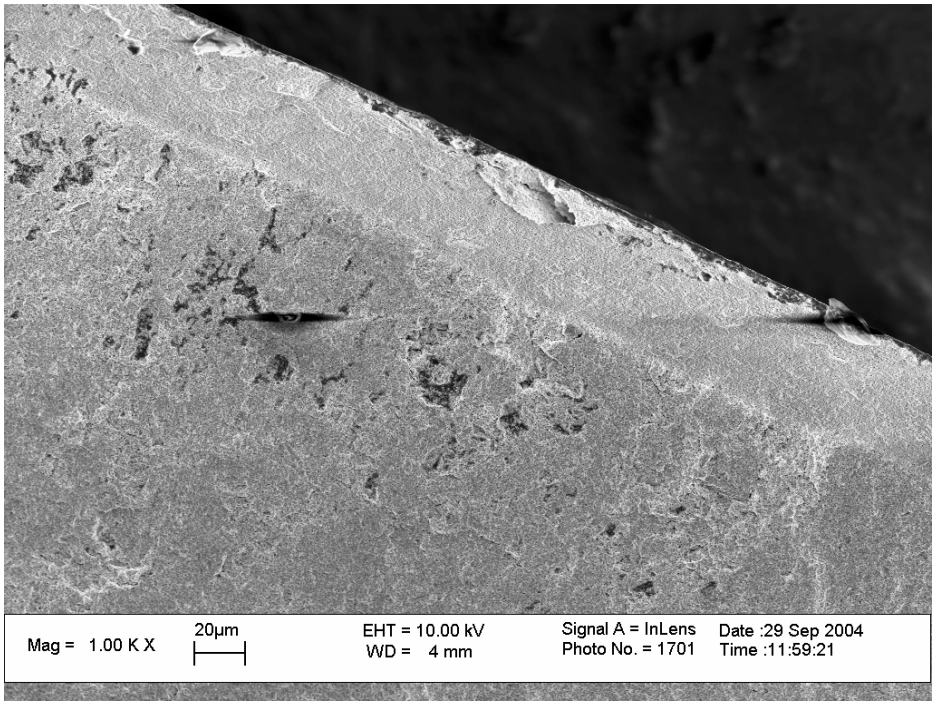

Figure 7. 2. Micrograph of a cathode-supported thin-film cell, 50 µm BYZ supported on $BaZr_{0.40}Pr_{0.40}Gd_{0.20}O_3$.

Appendix A: Anode Supported Ceria Fuel Cell Fabrication

A.1 Introduction

Solid oxide fuel cells (SOFCs) exhibit a number of attractive features for power generation, including efficiency, fuel flexibility, and relatively inexpensive electrode materials; however, the high operating temperatures required (800–1000 ^{o}C) introduce a number of challenges. In particular, thermal expansion mismatches between components can lead to failure of the seals that separate anode and cathode chambers. One strategy for addressing this challenge is to utilize a single chamber fuel cell in which the fuel and oxidant are allowed to mix, eliminating the need for seals. As a result, anode and cathode reactions take place within the same physical chamber.

In this section, preparations of SDC-based fuel cells using the colloidal deposition techniques are explored. This technique allows for the deposition of thin electrolyte film on the support, Figure A.1, reducing ohmic loses due to the electrolyte. The fuel cells were based on $Sm_{0.15}Ce_{0.85}O_2$ (SDC), provided by NexTech materials or synthesized in-house by solution chemical methods. A Ni+$Sm_{0.15}Ce_{0.85}O_2$ (NiO:SDC=50:50 wt.%) cermet was used as the anode, and a $Sm_{0.5}Sr_{0.5}CoO_{3-\delta}$ (SSC) cathode examined.

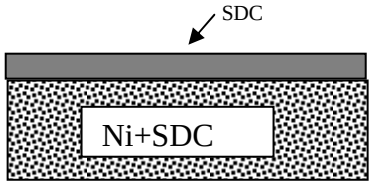

Figure A.1. Schematic of thin film SDC electrolyte on SDC-NiO cermet anode support.

A.2 Optimization of Colloidal Deposition for the Ceria Thin-film System

Fabrication of a thin-film samarium doped ceria (SDC) fuel cell using the colloidal deposition technique requires the optimization of a variety of parameters including: (1) uniaxial pressure of the support, (2) prefire temperature of the support, (3) particle size of the support and electrolyte, (4) colloidal solution, (5) deposition pressure and technique, and (6) deposition temperature.

The anode support consisted of 50:50 wt.% NiO (black powder with a mean particle size 0.60 μm) and commercial SDC powder (Nextech Materials). To this mixture 5 wt. % PVB was added to serve as a binder. SDC-NiO-PVB mixture was attritor milled for 2 hrs resulting in mean particle size in the range of 0.18–0.28 μm. Powders were dried and put through a 150 μm sieve (a blend of agglomerates, binder, and particles). If the mixture particles are too fine, the powders will stick during the pressing stage, and coarse particles will result in nonuniformity. The agglomerate will break once pressure is applied to the powders.

Pressures in the range of 50–300 MPa were examined for the anode support. Lower pressures resulted in a lower green density causing a higher linear shrinkage of the support during sintering. Higher shrinkage of the support results in a higher density of the thin film. To permit for maximum shrinkage of the support, a minimal pressure of 50 MPa was determined to be a good compromise between the shrinkage needed to densify the thin film and maintain the structural integrity and stability of the support. Pressures in the range of 200–300 MPa produced upward curvature in the pellet during the sintering process. The upward curvature was a result of the thin film shrinking more than the support. Downwards curvature results from the support shrinking greater than the film, Figure A.2.

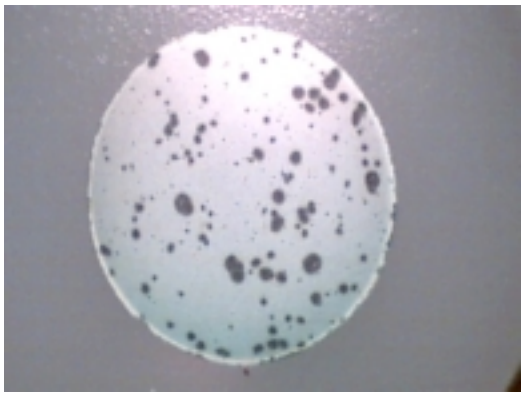

Figure A.2. Cell resulting from mismatch in thermal expansion coefficient; the shrinkage in the support was significantly larger than the film.

Prefiring of the support allows for the creation of pores by removing the organics and creating a rigid support to which film will be deposited. Eliminating the prefire step will result in cracking of the support due to the high pressures exerted during the deposition of the film. Pre-firing temperatures in the range of 800–900 °C were examined. The prefire temperature's main influence is in the final shrinkage of the support. Holding all other parameters constant, the difference between 800 °C and 900 °C is an additional 2% shrinkage of the support during final sintering. The pre-fire temperature adjusted simultaneously with the support pressure allows matching the shrink of the support with the deposited film resulting in a flat cell. A temperature of 825–850 °C was chosen as ideal for fabrication.

The anode surface area was limited by the starting particle size of NiO (Alfa-Aesar) and milling limit of a traditional ball mill. The anode surface area was measured to be 12–15 m^2/g. Electrolyte surface area of 13, 26, 35 m^2/g were studied. The surface area of the powder was controlled by calcination and milling. Electrolyte surface area of 13 m^2/g produced the best results due to a similar thermal expansion as the support. Electrolyte powders with higher surface area shrunk more, Figure A.3, than the support during sintering causing a cell with upward

curvature. Also, the powders with the highest surface area, 35 m^2/g, resulted in the film detaching from the support.

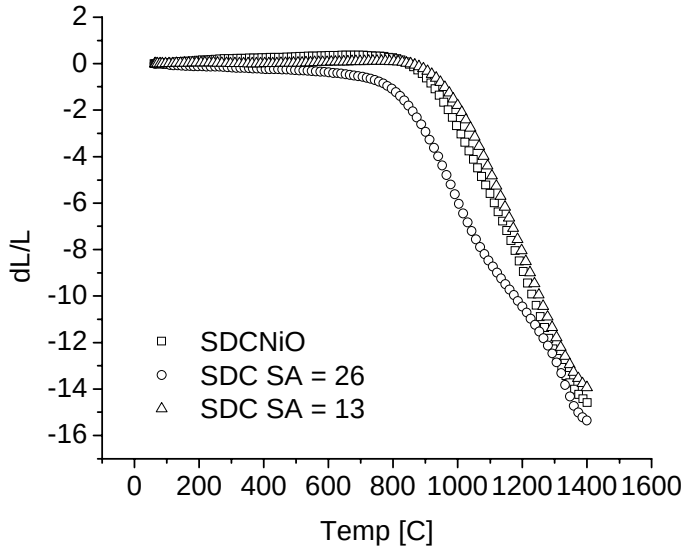

Figure A.3. Dilatometry curves of substrate and 13 m^2/g and 26 m^2/g electrolyte solution.

Sintering of the film and substrate should be at the minimum temperature required to achieve 18%–25% shrinkage. 20% shrinkage is ideal for the colloidal deposition method. In this case sintering time was established per Eq. (A.1). Sinter electrolyte for a longer periods of time results in grain growth which will destabilize the thin film.

3 ºC/min → 750 ºC for 30 min → 5 ºC/min → 1400 ºC for 4hr → 5 ºC/min (A.1)

For an ideal dense film, the substrate should shrink sooner in temperature and have overall more shrinkage than the film, Figure A.4. This allows for compression of the film during sintering avoiding cracks or flaws in the thin electrolyte layer.

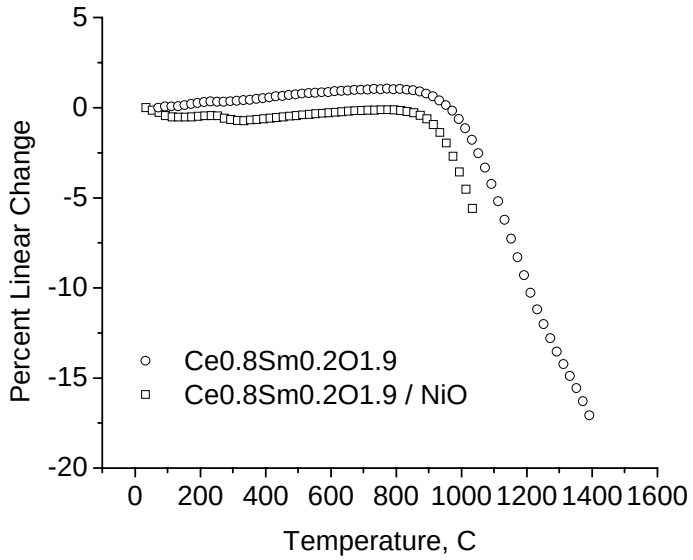

Figure A.4. Dilatometry results of both SDC electrolyte and SDC-NiO anode support

The colloidal solution concentration and their influence on the uniformity of the film were also investigated. To prepare the SDC commercial powder (Nextech Materials), powder was calcined at 1000 ºC for 1 hr to increase particle size. Powder was then attritor milled for 1 hr to break large agglomerate and achieve the particle target range of 0.2–0.3 μm (slightly larger than support particle size, 0.18–0.28 μm). Fish oil (2 wt.%) can be added during milling to aid in the dispersion of the powder in solution. A plasticizer, bibutyl-phthalate can also be added (2–3 drops) to help prevent cracking.

Solutions in the range of 0.002–0.02 g/mL were used for the deposition. It was found that the uniformity of the film highly depended on the number of layers deposited. A working concentration of 0.005 g/mL was determined appropriate to allow the deposition of multiple layers (20+). Higher concentrations (over 0.01 g/mL) lead to instability in the film resulting in local areas of high intensity of the electrolyte material, Figure A.5.

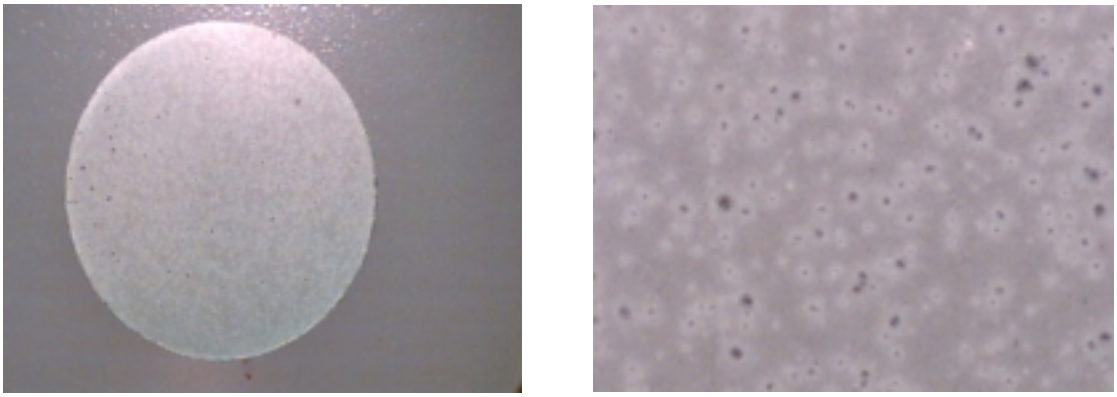

Figure A.5. Cell resulting from a high concentration of solution (a) 10x and (b) 60x.

Deposition pressure plays an important role in the creation of a uniform dense film. It should be noted that prior to deposition, it is critical for the surface of the substrate to be clean of dust particles and/or finger prints. Given the optimized anode support uniaxial pressure and pre-firing temperature, a pressure of 15 psi was determined to be ideal for the deposition of the ceria electrolyte. Higher pressures (~25 psi) resulted in fractures in the pellet during the deposition process, while deposition with lower pressures (~5 psi) results in a not densified film. To create a dense film given the maximum shrinkage (as determined by the pressing pressure and prefire temperature), a relatively high packing of the electrolyte is needed. This is achieved with a pressure of about 15 psi and with deposition 2–3 inches from the surface and perpendicular to the support. When depositing, the spray should hit the support surface wet. Depositing too far from the support or allowing the solution to dry before contacting with the support lead to inconsistency in the film. Upon completion, sample should be dried with compressed nitrogen.

Although not as significant as other parameters varied, the hot plate temperature will affect the uniformity of the film. Without the use of heat, deposition results in a nonuniform film due to the formation of puddles. For the best conditions, the hot plate is set to 90–95 °C (slightly above the boiling temperature of isopropanol, the solvent). This allows for the electrolyte particles to deposit wet while instantaneously evaporating the solvent. The film will become non-uniform,

Figure A.6 if the surface is too wet, developing puddles, and also if the particles are deposited dry (as described above). For a uniform, dense film (Figure A.7) the temperature of the hot plate should be set to approximately 95 °C to avoid the formation of puddles.

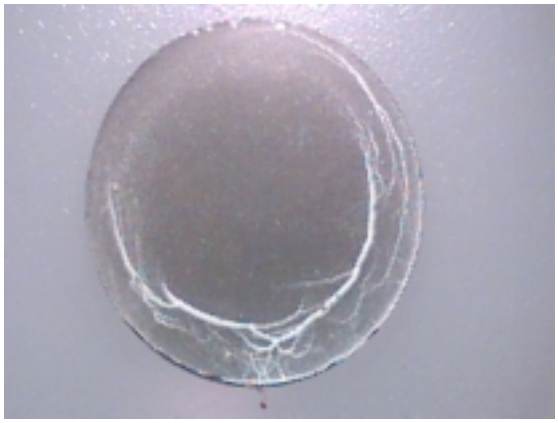

Figure A.6. Nonuniform film due to deposition at a low hot plate temperature allowing for the forming puddles.

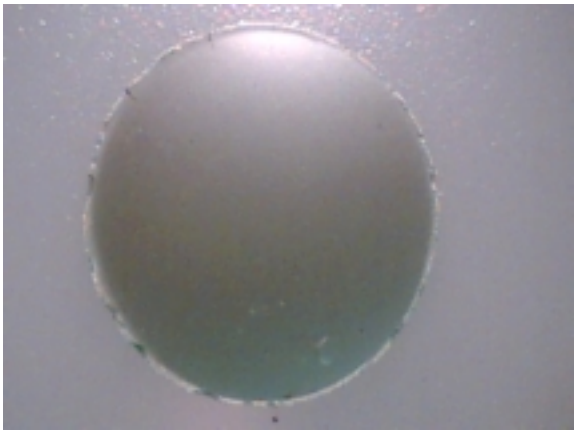

Figure A.7. Dense-uniform film deposited on an anode support.

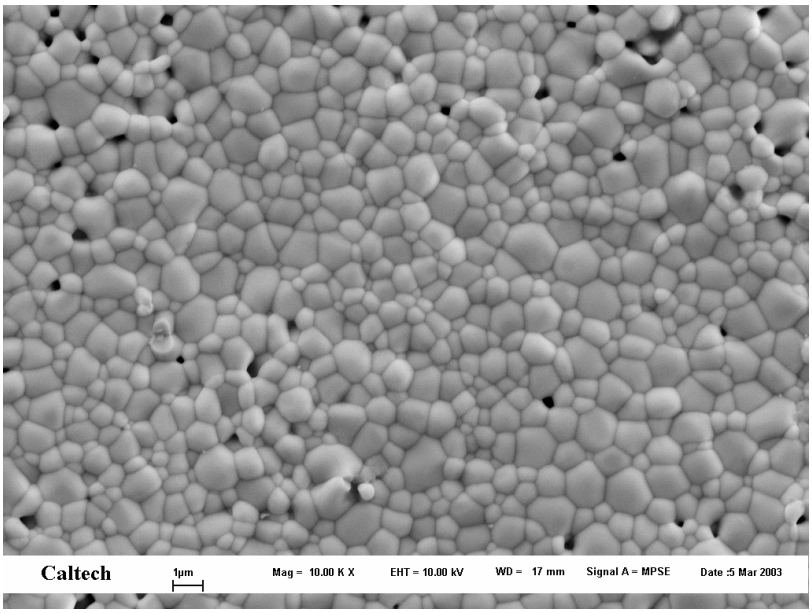

Figure A.8. SEM micrograph of the surface of deposited film.

A.3 Colloidal Deposition of Electrodes for the Ceria Electrolyte Supported System

Electrolyte supported $Ce_{0.80}Sm_{0.20}O_2$ (Samaria doped ceria) fuel cell with Ni-$Ce_{0.80}Sm_{0.20}O_2$ anode and $Sm_{0.50}Sr_{0.50}CoO_3$ (Strontium-doped samarium cobaltite) cathode was prepared using the colloidal deposition technique. Electrolyte was sintered at 1350 ºC for 4 hrs resulting in a dense support. The ceria electrolyte was masked, Figure A.9, with tape allowing for a consistent electrode area between cells. Both electrodes (anode and cathode) were deposited using similar colloidal solution and technique as described in appendix A.1. Deposition results and uniformity can be seen in Figure A.10. Platinum mesh was then adhered to the electrodes using Pt paint to serve as a current collector, Figure A.11.

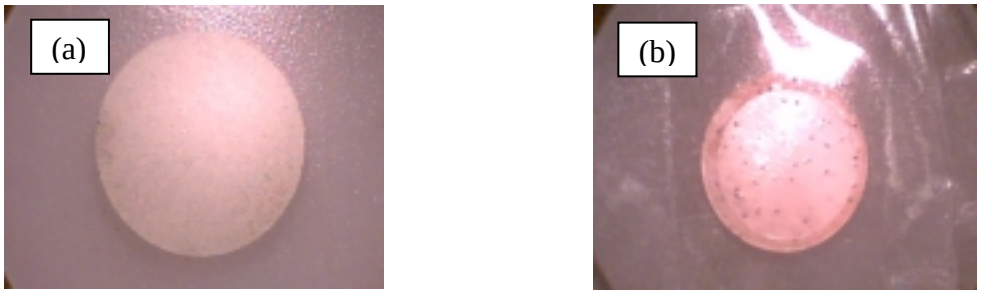

Figure A.9. Photograph of (a) $Ce_{0.80}Sm_{0.20}O_2$ 15 mm pellet, (b) pellet masked before electrode deposition.

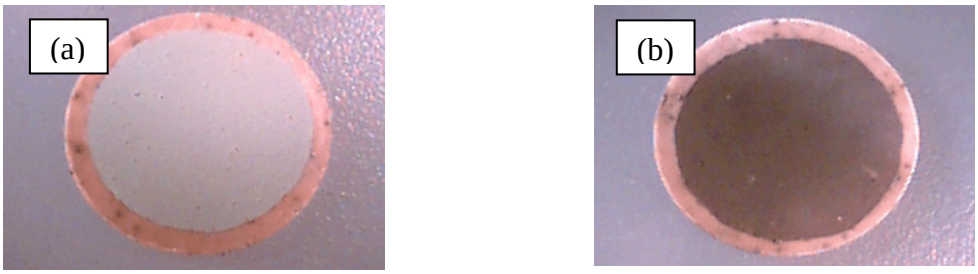

Figure A.10. Photograph of (a) SDC-NiO anode, (b) SSC cathode.

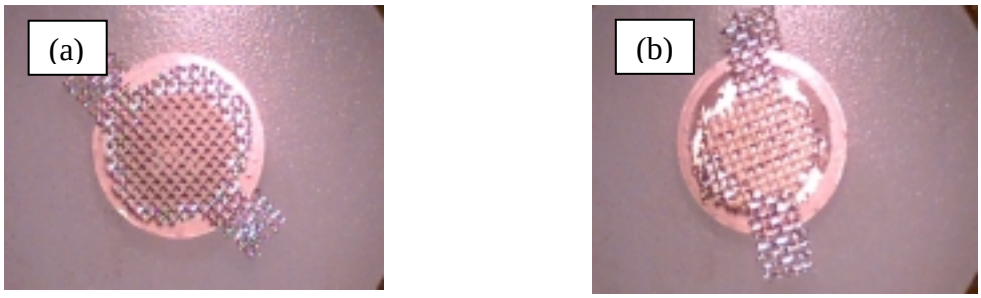

Figure A.11. Photograph of (a) anode side with current collector, (b) cathode side with current collector.

A.4 Conclusions

Optimized process for deposition of ceria electrolyte thin film on anode support included

1. SDC:NiO:PVB weight ratio of 47.5:47.5:5, respectively.
2. Anode cermet attritor milled for 2 hrs (0.18–0.28 μm particle size) and sieved with 150 μm sieve opening.
3. Pressure of 50 MPa for uniaxial pressing of support
4. Anode support prefire temperature of 825–850 °C was chosen as ideal (1% shrinkage).
5. Electrolyte surface area of 13 m^2/g (0.20–0.30 μm particle size) produced the best thermal expansion match as the support.
6. Sintering of the film and support were optimized as follows 3 ºC/min → 750 ºC for 30 min → 5 ºC/min → 1400 ºC for 4hr → 5 ºC/min.
7. Electrolyte concentration of 0.005 g/mL was determined appropriate to allow the deposition of multiple layers.
8. A pressure of about 15 psi when depositing with 2–3 inches from the surface and perpendicular to the support.
9. Hot plate should be set to approximately 95 °C to avoid the formation of puddles. Solution should deposit wet but instantaneously evaporate.

Appendix B: Analysis of TiO as a Sintering Aid for Doped Barium Zirconate

B.1 Introduction

In collaboration with Nextech Materials (Ohio, USA), TiO was studied as a sintering aid for the 15 Y mol % doped barium zirconate (BYZ15). All samples were prepared by Nextech Materials and characterized at Caltech.

B.2 Sintering and Conductivity Results

TiO as a sintering aid showed modest improvements in the densification of barium zirconate. The onset of sintering in BYZ with TiO, occurs at approximately 1100 °C, 100 °C before its onset in the BYZ system. Furthermore, at 1500 °C the total linear shrinkage for BYZ-TiO system, Figure B.1, is 7% as compared to only ~2% for BYZ.

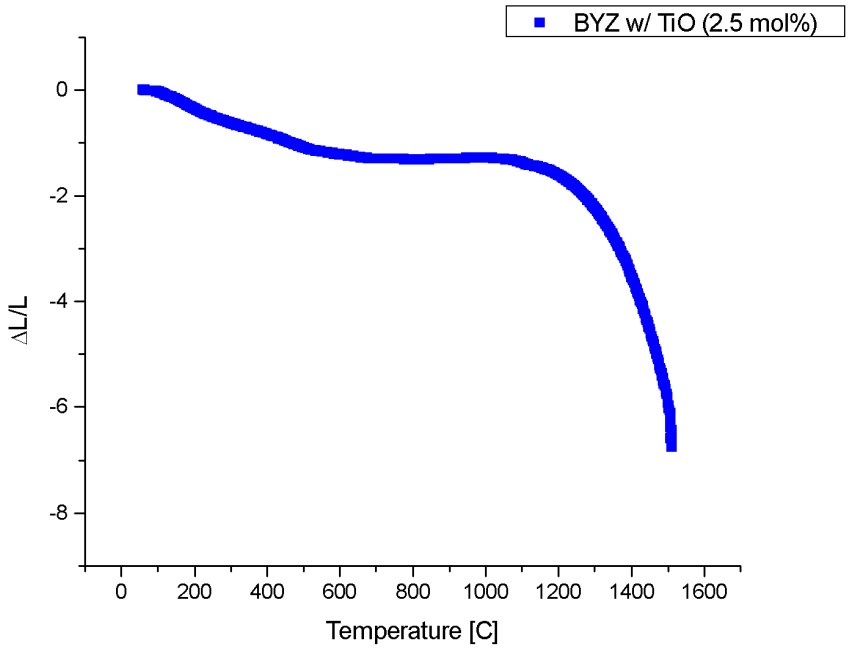

Figure B.1. Dilatometry results for BYZ15 with 2.5 mol% TiO.

Although improvements in densification can be achieved with TiO as a sintering aid, its affect on BYZ's electrical properties are detrimental. Bulk conductivities of sample 106-131 series, Figure B.2, are significantly lower than those of doped barium zirconate. Bohn and Schober [1] reported BYZ10 log(sigma*T) value of 0.42 for bulk conductivities at 600 ºC (1000/T value of 1.15). Our results indicate a log(sigma*T) value of -1.29 at 600 ºC. In terms of conductivities, Bohn reporting 10^{-3} S/cm at 600 ºC, while our data shows 10^{-5} S/cm, two orders of magnitude lower.

The 106-131 series consisted of BYZ15 with 10 mol % TiO. These samples were sintered at 1600 ºC for 2 hrs, resulting in an average density of 93% (compared to theoretical 6.12 g/ cm^3).

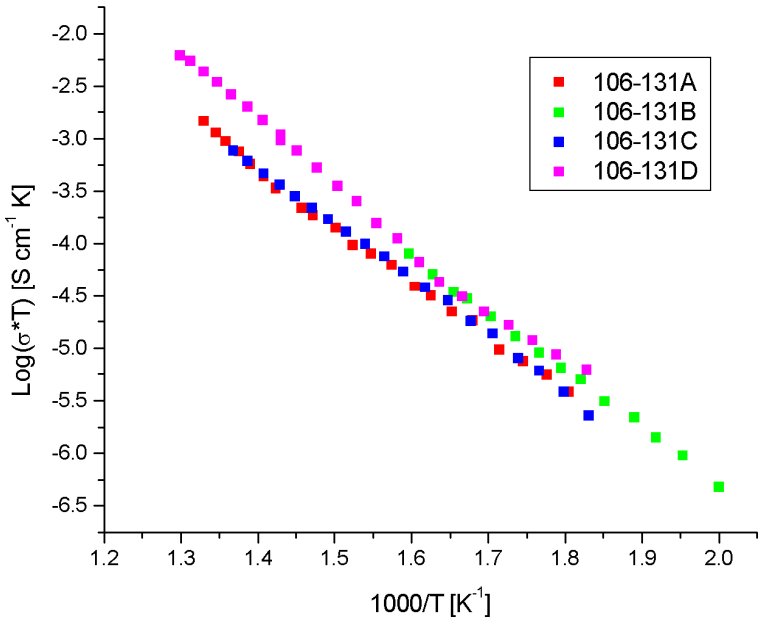

Figure B.2. Bulk conductivity in water saturated nitrogen atmosphere of BYZ with TiO modifier, sample 106 series.

Sample N106 series were prepared in hopes of optimization of the processing.

Samples consisted of N106-145A with BYZ+5 mol % Ti and a density of 90%, sample N106-145B consisted of BYZ+10 mol % Ti with density 95%, and sample N106-145C consisted of $Ba(Zr_{0.8}Y_{0.1}Ti_{0.1})O_3$ with density 94%.

Sample showed slightly higher conductivities, 10^{-4} S/cm and 600 ºC, Figure B.3. Significant differences were not observed between incorporating the Ti in the perovskite structure and synthesizing BYZ without accommodating for the Ti in the structure.

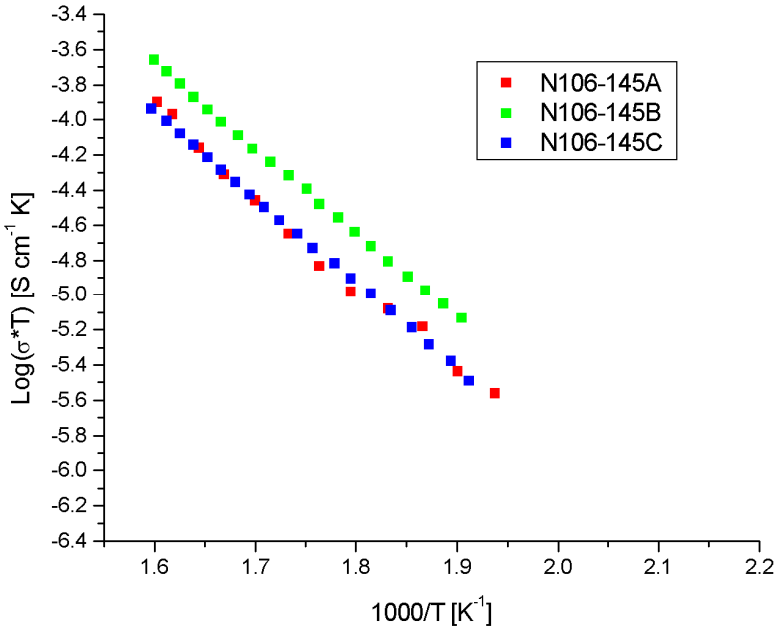

Figure B.3. Bulk conductivity in water saturated nitrogen atmosphere, sample N106 series.

Due to the high density of barium zirconate achieved with the TiO modifier, it was hypothesized that the low conductivity might be due to insufficient water saturation (or proton incorporation) of the sample. Sample N106 was pre-saturated for 15 hrs at 900 ºC before measurements were preformed. The presaturation step did not affect the bulk conductivity, Figure B.4. Data were surprisingly consistent suggesting that such extreme measures of presaturation were not necessary.

Although many more samples were provided by Nextech with varying TiO mole percentages and varying synthesis routes and methods, significant improvements in conductivities were not observed.

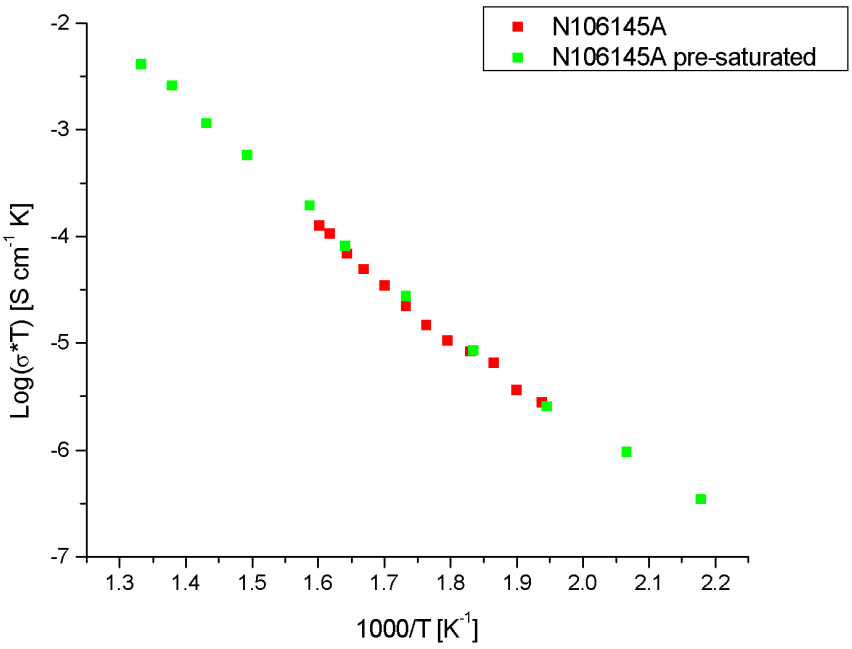

.

Figure B.4. Bulk conductivity in water saturated nitrogen atmosphere. "Presaturated" run was saturated for 15 hrs at 900 ºC before conductivity measurements.

B.3 Conclusions

Although improvements in density were observed with the use of TiO as a sintering aid, its affects on the bulk conductivity of BYZ was detrimental. As discussed in Chapter 3, it is believed processing temperature of 1600 ºC leads to considerable barium deficiencies in the sample. These samples did not have the benefits of the advanced processing methodology developed in Chapter 3. As it is well described in this thesis, such Ba deficiencies are destructive to the conductivities of doped barium zirconate.

B.4 References

1. H. G. Bohn and T. Schober. Electrical conductivity of the high-temperature proton conductor $BaZr_{0.9}Y_{0.1}O_{2.95}$. *J. Am. Ceram. Soc.* **83,** 768 (2000).